

AN EXPERIMENTAL INVESTIGATION OF DRAG
AND THE TURBULENT FLOW STRUCTURE
IN SIMULATED AND REAL AQUATIC VEGETATION

A Dissertation

Presented to the Faculty of the Graduate School
of Cornell University

in Partial Fulfillment of the Requirements for the Degree of
Doctor of Philosophy

by

Rafael Omar Tinoco Lopez

August 2011

© 2011 Rafael Omar Tinoco Lopez

AN EXPERIMENTAL INVESTIGATION OF DRAG AND THE TURBULENT FLOW STRUCTURE IN SIMULATED AND REAL AQUATIC VEGETATION

Rafael Omar Tinoco Lopez, Ph.D.

Cornell University 2011

The presence of aquatic vegetation in streams generates coherent structures at several length scales, that depend on the properties of both the vegetation and the flow. Stem- and leaf-scale wakes are generated as water moves within the canopy and the drag discontinuity at the top of the plants creates a free shear layer-like flow with coherent vortices that penetrate within the vegetation. Models to estimate velocity, turbulence, mixing rates, dispersion, and residence time within these complex, vegetated flows, require knowledge of the force exerted by the plants, often represented in terms of a drag coefficient, C_d , and yet its value is often left as a calibration parameter, to match numerical models against laboratory and field data.

We present a laboratory, non-intrusive, drag measuring device. The drag plate is tested on two well documented cases: uniform flow over a flat plate, and flow around a rigid cylinder. The successful performance of the device proves it suitable for direct measurements of drag on more complex, single or multiple, rigid or flexible elements, which makes it an ideal device for studies on vegetated flow, natural rough-bed boundary layers, and coastal structures. We use the drag plate, coupled with quantitative imaging techniques, to capture the velocity field and obstructed frontal areas associated with it, and we generate an extensive data set for flow through submerged and emergent arrays of rigid cylinders, as well as submersed and emergent canopies of live, flexible stems of Eurasian watermilfoil (*Myriophyllum spicatum*). Direct measurements of drag in flow through aquatic vegetation

are still rare, since most research groups often estimate its value using a simplified momentum equation, which does not necessarily hold for all scenarios. Our direct approach allows us to compare those estimates against actual measurements, and to identify sources of errors in the estimated values.

We use the measured values of drag in rigid cylinders, to obtain fitting parameters to predict C_d in canopies of live, flexible stems as a function of solid volume fraction, ϕ , and a diameter based Reynolds number, $Re_d = Ud/\nu$. For live stems, an effective diameter is proposed as the characteristic length scale, calculated from values of the volumetric frontal area, a (obstructed frontal area per unit volume, $[L^{-1}]$), and the canopy density n (number of stems per unit horizontal area $[L^{-2}]$), as $d_e = a/n$. The predicted values of C_d , and the newly introduced length scale, d_e , successfully perform at estimating the total drag, and balancing both momentum and turbulent kinetic energy budgets.

BIOGRAPHICAL SKETCH

The author was born in Mexico City, Mexico, in 1981. He graduated from the Universidad Nacional Autonoma de Mexico as a Civil Engineer in 2005. That same year he moved to Ithaca, NY, to pursue a Ph.D. degree at Cornell University, working with Prof. Todd Cowen studying the hydrodynamics of vegetated flow. In 2008, he received an M.S. degree from his studies on flow through emergent canopies of flexible, live vegetation, which established the foundation from which continue and expand his work on canopy flows.

DEDICATORY

To Agnieszka and Jakub

ACKNOWLEDGMENTS

Sincere thanks go to Todd Cowen, Lance Collins, and Nelson Hairston for their valuable advice and encouragement during my time at Cornell. Special thanks to Robert Johnson for sharing his vast experience on aquatic vegetation. Thanks to Evan Variano, P.J. Rusello, Allie King, and Yong Sung Park for sharing their expertise with the facilities and equipment at the DeFrees Lab. Thanks to Seth Schweitzer, Paul Richter, Jorge Escobar, and everyone in the EFMH group who contributed during the laboratory experiments. Thanks also to Paul Charles, Tim Brock, and Cameron Willkens for their help with designing, building, and fixing the experimental equipment.

Acknowledgment must also go to the CONACyT and the graduate school at Cornell University for funding the author's studies at Cornell University. Special thanks to the 'Alberto y Dolores Andrade' Foundation for their continuous support. This work was also supported by the National Science Foundation through award CBET-0626164. Any opinions and comments are those of the author and do not necessarily reflect the views of the sponsors.

TABLE OF CONTENTS

Biographical sketch	iii
Dedicatory	iv
Acknowledgments	v
Table of contents	vi
1 Introduction	1
1.1 Objectives	1
1.2 Relevant field and laboratory parameters	3
1.3 Physical processes involved	5
1.4 Thesis structure	12
2 Experimental facilities and techniques	14
2.1 Introduction	14
2.2 Recirculating open channel flumes	15
2.3 Arrays of rigid cylinders	16
2.4 Arrays of flexible, live stems	18
2.5 Flow rates	19
2.6 Velocities	20
2.7 Frontal areas	22
2.8 Free surface slopes	26
2.9 Drag	29
2.10 Conclusions	29
3 Direct and indirect measurements of boundary stress and drag on simple and complex arrays of elements	30

3.1	Introduction	30
3.2	Design and calibration	32
3.3	Validation experiments	36
3.3.1	Flat plate boundary layer verification test	37
3.3.2	Single rigid cylinder verification test	40
3.3.3	Arrays of rigid cylinders	43
3.4	Conclusions	46
4	Flow through and above arrays of rigid cylinders	49
4.1	Introduction	49
4.2	Experimental procedure	50
4.3	Results from arrays of emergent cylinders ($H = h$)	51
4.3.1	Analysis of drag and velocities	51
4.3.2	Analysis of momentum and tke budgets	65
4.4	Results from arrays of submerged cylinders ($H > h$)	69
4.4.1	Flow characterization	69
4.4.2	Analysis of drag and velocities	77
4.4.3	Analysis of momentum and tke budgets	89
4.5	Conclusions	95
5	Flow through and above canopies of flexible, live vegetation	97
5.1	Introduction	97
5.2	Experimental procedure	99
5.3	Results	102
5.3.1	Characterization of real vegetation	102
5.3.2	Flow characterization	106
5.3.3	Analysis of drag and velocities	109
5.3.4	Analysis of momentum and tke budget	122

5.4	Conclusions	131
6	Conclusions	132
	References	135

Chapter 1

Introduction

1.1 Objectives

The effect of physical obstructions in flows has always been an important subject in fluid mechanics. Whether the interest is on single or multiple, regular or irregular shaped obstructions, researchers have tried to characterize the physical processes generated by the flow-obstruction interactions.

A main concern has been the proper characterization of the drag force, D , acting on the immersed bodies. It is customary in fluid mechanics to represent D as a quadratic function of velocity, as stated in Eq. 1.1.

$$D = \frac{1}{2}\rho C_d A_f U^2 \quad (1.1)$$

In Eq. 1.1, ρ is the fluid density, A_f is a characteristic frontal area of the object, perpendicular to the mean flow, U is a characteristic velocity of the flow, and C_d is the drag coefficient, a value that depends on both the flow and obstruction characteristics.

Early experimental works, such as that from Wieselsberger (1922a), reported and analyzed by Schlichting (1979), characterized the drag coefficient for simple shapes, such as rigid cylinders and spheres, and found a relationship between C_d and a diameter-based Reynolds number, $Re_d = Ud/\nu$, where ν is the kinematic viscosity of the fluid and d is the diameter of the element. In most introductory fluid mechanics textbooks today, one can find the values of C_d as a function of Re_L , where L is some characteristic length scale of the obstruction, for several simple shapes. When dealing with more complex geometries, or with arrays of elements in the flow, such as flow through aquatic vegetation, a standard methodology to determine the values of C_d is still unknown.

Our primary goal is to characterize the drag exerted by vegetation. It is expected that high flow rates will generate larger drag forces, able to dislodge organisms living within the canopy and damage the plants themselves, or to destroy their assemblages. At the same time, high flow rates can increase mixing rates to improve the exchange of nutrients. On the other hand, while low flow rates will produce less drag and create a less turbulent environment, the lower mixing rates can become less favorable to some organisms (Nikora, 2009). Flexible plants will bend into a more streamlined configuration to reduce their exposed area and decrease drag, but that area reduction implies also a smaller surface for nutrient exchange, which along with self-shading and shading from adjacent stems can decrease light absorption. A better understanding of vegetated drag will help us clarify where the optimal range is for different plant species. We use a direct approach, measuring the actual drag exerted by the immersed bodies, by means of a drag plate, with a surface sufficiently large to average over several elements in the flow. Our novel device, introduced in Chapter 3, allows us to measure with precision bulk, mean values, and high frequency variation of the drag.

1.2 Relevant field and laboratory parameters

The interactions between flow and aquatic vegetation have been studied by research groups from a broad range of fields, mainly focused on either physical or biological processes.

From a physical processes perspective, it is known that aquatic vegetation a) impacts mean and turbulent flow structure in channels and coastal regions, b) generates drag, thus increasing flow resistance, c) controls the residence time within the water body (Rueda and Cowen, 2005; King, 2011), and d) modifies dispersion and diffusion within the canopy (Nepf et al., 1997b). From a biological oriented perspective, the presence of plants in streams a) promotes pollutant removal and degradation, b) provides shading to suppress algal growth, c) offers food and habitat to native wildlife, and d) the seasonal variations of populations varies the internal loading of phosphorus and nitrogen to the water column (Jadhav and Buchberger, 1995). With such a broad range of phenomena involved, we find research groups motivated by both a purely engineering approach, calculating the increased flow resistance due to vegetated beds on natural and man-made streams (Freeman et al., 2000; Jarvela, 2002; Baptist et al., 2007), and more ecologically-oriented research, such as the works on nutrient exchange between vegetation and the surrounding flow (Su et al., 1996; Ackerman, 1997).

Approaching the study of vegetated flow from a multidisciplinary perspective, one has to deal with different metrics, customary for each discipline, that must be “translated” between research groups, as often vegetation metrics from field macrophyte surveys, useful for biological studies, have to be interpreted and converted into useful parameters for fluid mechanics laboratory studies or modelling efforts.

Field surveys follow standard procedures to harvest macrophytes (e.g., see Johnson et al., 1998), and provide data such as:

W_d [M]: Dry weight, measured after 48 hours at $105^\circ C$.

B_m [ML^{-2}]: Biomass, the mass or weight of all living material on a unit area, A , at a given instant in time, usually $B_m = W_d/A$.

L_S [L]: Mean stem length, the total length of the extended stem, not necessarily the same as canopy height h .

SC [$\%$]: Species composition, the percentage of dry weight corresponding to each species in a specific area.

For laboratory experiments, however, we are interested in particular metrics, such as:

A_f [L^2]: Frontal area, a cross sectional area perpendicular to the mean flow.

a [L^2L^{-3}]: Volumetric frontal area, the total frontal area per unit volume of fluid.

ϕ [$\%$]: Solid volume fraction, the volume of plant material per unit volume.

η_p [$\%$]: Porosity, $\eta_p = 1 - \phi$.

In Chapter 2 we present the approaches used to convert field data into laboratory parameters, which are later applied in Chapter 5.

For our live plants studies, we chose Eurasian watermilfoil, *Myriophyllum spicatum*, an aquatic invasive species, commonly found throughout water bodies in North America (Madsen et al., 1991; Janauer and Dokulil, 2006). It has a thin $d \simeq 1 - 2mm$, flexible stem, with deeply-divided feather-like leaves. It is a fairly buoyant plant, with an approximate specific gravity of 0.8 (Koegel et al., 1973), adaptable to a wide range of conditions, which grows at depths of 0.5 to 9m until it reaches the water surface, forming a canopy that shades out smaller native plants, creating a watermilfoil monoculture as a result (Aiken et al., 1979; Johnson, 2008). Hereafter we use the term ‘canopy’ to indicate the vegetated layer formed by the branches and leaves of the vegetation, and ‘macrophytes’ to indicate aquatic plants large enough to be apparent to the naked eye. A distinction is also made between

submerged ($H/h > 1$) and emergent ($H/h \leq 1$) aquatic plants, where H [L] is the water depth and h [L] is the canopy height.

1.3 Physical processes involved

To study vegetated flow in a laboratory setting, research groups often use cylindrical shapes to recreate the plant canopies. Although flow around a cylinder has been thoroughly studied, its complexity increases as we add more elements into the flow, as the works of Williamson (1985), Sumner et al. (1999), and Lam et al. (2003), have shown for groups of 2, 3, and 4 cylinders, respectively. If the number increases to hundreds or thousands of elements, as is often the case to model aquatic vegetation, a bulk, averaging approach has to be used. Dunn et al. (1996) used wooden dowels and straws to recreate rigid and flexible plants in staggered arrays (submerged). Nepf et al. (1997a) used randomly arranged wooden cylinders, and added plastic stripes to model flexible branches (emergent). Nepf (1999) and Tanino and Nepf (2008a) investigated drag on arrays of rigid, wooden cylinders (emergent), the same materials used by Stone and Shen (2002) (emergent and submerged). Ghisalberti and Nepf (2002) built a scaled eelgrass model using polyethylene blades attached to a short cylindrical base (submerged).

All the authors mentioned above deal with drag using an indirect approach, estimating it from velocity and free surface slope measurements, as will be detailed shortly. Additionally, instrumentation, facilities, and methodology, can vary widely between authors, forcing us to take a more cautious approach to make comparisons between their results, since, as we discuss in Chapter 2, location, and number of measurements can yield large differences in the determined values. Research groups working on numerical models of vegetated flow, require experimental data to calibrate their models, but even with the increasing number of published

experimental works, finding consistent experimental data, that covers wide ranges of every relevant parameter, d , a , ϕ , H/h , is rare.

We generate a unique data set, by using the same facilities and techniques, as outlined in Chapter 2, to analyze four different aspects of vegetated flow, represented in Figure 1.1:

- A) flow through emergent rigid arrays of cylinders.
- B) flow through and above submerged arrays of rigid cylinders.
- C) flow through an emergent patch of flexible, live stems of Eurasian watermilfoil.
- D) flow through and above a submerged patch of flexible, live stems of Eurasian watermilfoil.

Each case shown in Figure 1.1 presents noticeable distinctive features, in response to the dominant physical processes involved. A simple sketch is presented in Figure 1.2 showing the increasing flow complexity, from the stem wakes on rigid cylinders (I), the added leaf-scale wakes as the plants start branching out (II), and the mixing layer-like structure formed between denser and more open regions of the canopy (III). Under submerged conditions, an additional shear layer is created at the top of the canopy. Let us discuss the physical processes and the governing equations applicable for each case represented in Figure 1.1.

For our experimental conditions, assuming a two-dimensional $x - z$ flow, where x , y , z are orthogonal coordinates, x is positive in the direction of the mean flow, y is the horizontal, span-wise direction, and z is vertical upwards, with their respective velocities u , v , and w , the temporally- and horizontally-averaged streamwise momentum equation, can be written as (Raupach and Thom, 1981; Finnigan, 2000):

$$\begin{aligned} \frac{\partial \langle \bar{u} \rangle}{\partial t} + \langle \bar{u} \rangle \frac{\partial \langle \bar{u} \rangle}{\partial x} + \langle \bar{w} \rangle \frac{\partial \langle \bar{u} \rangle}{\partial z} &= -\frac{1}{\rho} \frac{\partial \langle \bar{p} \rangle}{\partial x} - \left(\frac{\partial \langle \bar{u}'u' \rangle}{\partial x} + \frac{\partial \langle \bar{u}'w' \rangle}{\partial z} \right) + \nu \frac{\partial^2 \langle \bar{u} \rangle}{\partial z^2} \\ &\quad - \left(\frac{\partial \langle \bar{u}''\bar{u}'' \rangle}{\partial x} + \frac{\partial \langle \bar{u}''\bar{w}'' \rangle}{\partial z} \right) - f_1 \end{aligned} \quad (1.2)$$

Each term in Eq. 1.2 is horizontally-averaged over an area large enough to eliminate variations caused by single elements. Horizontal, fully developed flow is assumed, resulting in no horizontal gradients, and each term being only a function of the vertical, z -direction. In Eq. 1.2, u and w are the velocities in the x and z directions respectively, ρ is the fluid density, p is pressure, and ν is the kinematic viscosity of the fluid. Here we use the Reynolds decomposition, using overbars to indicate time average, and angle brackets for spatial (horizontal) average, while single and double primes represent the variations from temporal and spatial averaging, respectively (Eq. 1.3 and 1.4). Such temporal and spatial decomposition produces the well known Reynold stresses $\langle \bar{u}'_i \bar{u}'_j \rangle$, and dispersive stresses $\langle \bar{u}''_i \bar{u}''_j \rangle$.

$$\xi = \bar{\xi} + \xi' \quad (1.3)$$

$$\bar{\xi} = \langle \bar{\xi} \rangle + \xi'' \quad (1.4)$$

Eq. 1.2 can be further simplified. For steady flow $\partial/\partial t = 0$. A hydrostatic assumption for pressure yields $\langle \bar{p} \rangle = \rho g \langle \bar{H} \rangle$. For uniform flow horizontal velocity gradients are negligible. Poggi et al. (2004a) found the dispersive stresses to be negligible except for very sparse arrays ($ah < 0.1$). Rosman et al. (2010) found dispersive stresses of the same order as Reynold stresses for experiments on model kelp, but still neglected them due to large uncertainties in their calculation. Our previous studies using Eurasian watermilfoil also found the dispersive stresses to

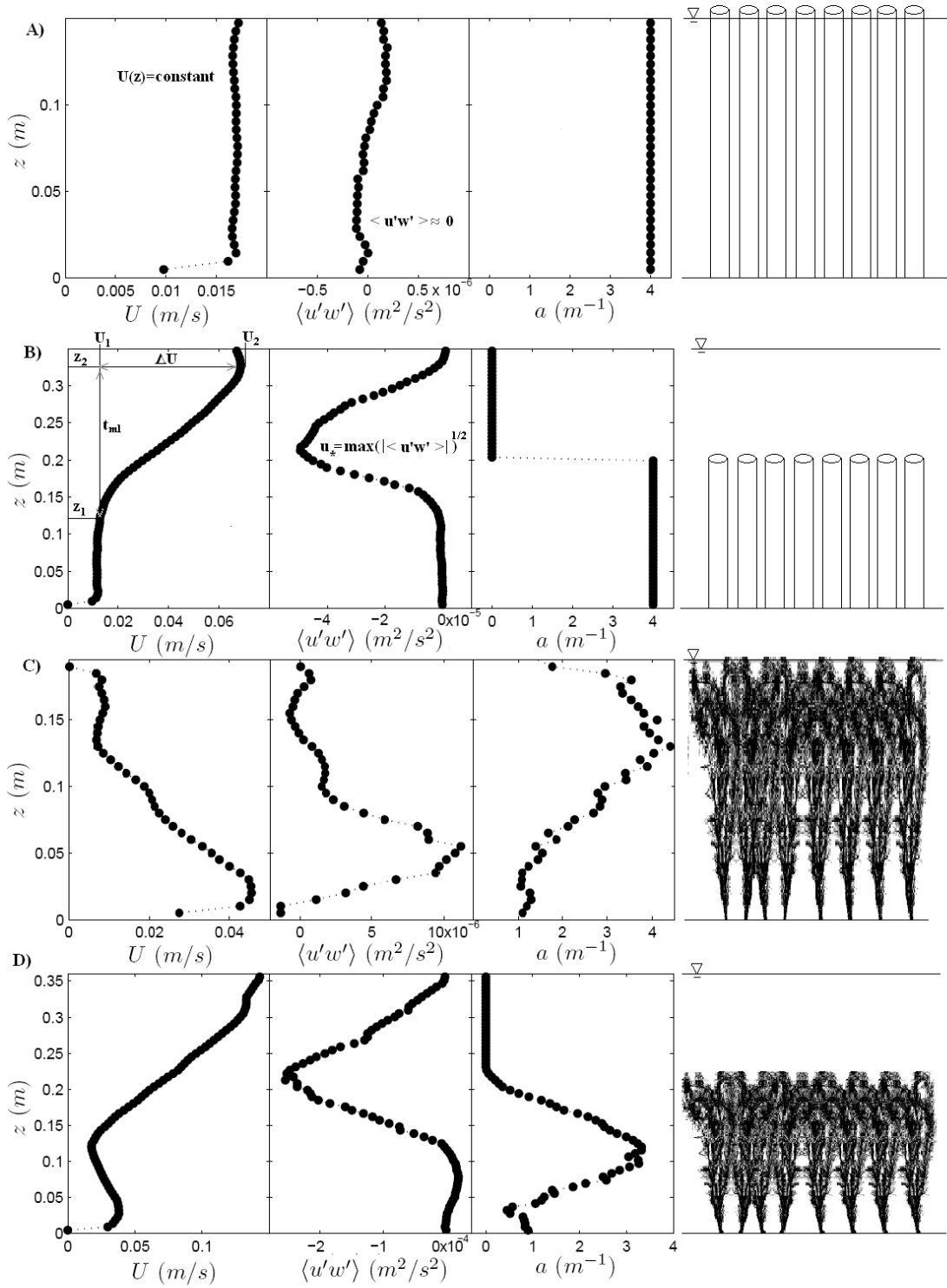


Figure 1.1: Typical measured vertical profiles of longitudinal mean velocity, U , Reynolds stress, $\langle u'w' \rangle$, and volumetric frontal area, a , for A) emergent, rigid cylinders, B) submerged, rigid cylinders, C) emergent, flexible vegetation, and D) submerged, flexible vegetation.

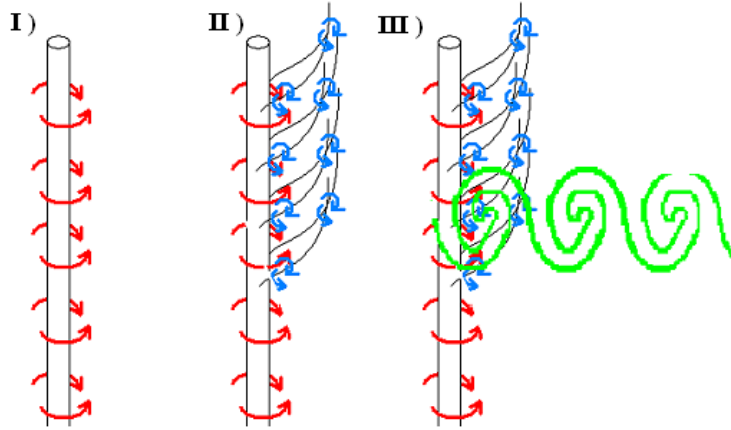


Figure 1.2: Expected flow patterns in vegetated flows: I) stem-scale wake turbulence, II) leaf-scale wake turbulence, III) canopy-scale mixing layer.

fall within the uncertainty range (Tinoco, 2008). A simplified horizontal momentum equation is then expressed as:

$$W \frac{\partial \langle \bar{u} \rangle}{\partial z} = -g \frac{\partial \langle \bar{H} \rangle}{\partial x} - \frac{\partial \langle \overline{u'w'} \rangle}{\partial z} + \nu \frac{\partial^2 \langle \bar{u} \rangle}{\partial z^2} - f_1 \quad (1.5)$$

For simplicity, U and W are herein used as short hand for $\langle \bar{u} \rangle$ and $\langle \bar{w} \rangle$, respectively. The free surface slope is defined as $S = \partial \langle \bar{H} \rangle / \partial x$. The drag term, f_1 , must account for form and viscous drag, and is here parameterized as:

$$f_1 = \frac{1}{2} C_d a U^2 \quad (1.6)$$

For each scenario (A, B, C, D) presented in Figure 1.1, the momentum equation can be further simplified as follows:

In (A) (Figure 1.1), the drag generated by the array of cylinders dominates over the vertical shear, suppressing all vertical gradients ($\partial/\partial z = 0$), yielding z -independent vertical profiles except very close to the bottom. For such condi-

tions, where the cylinder wakes and interactions among them control the flow, Eq. 1.1 can be expressed as:

$$0 = -gS - \frac{1}{2}C_d a U^2 \quad (1.7)$$

If all assumptions to get Eq. 1.7 are satisfied (steady state, uniform, fully developed flow, with a hydrostatic pressure distribution, and viscous and bottom stress negligibles), the force exerted by the array can be calculated from measurements of the free surface slope alone. The term gS is independent of z , meaning that the product $C_d(z)a(z)U(z)^2$ must also be independent of depth. In the simplest case, with rigid cylinders and a constant drag coefficient along the water column, this yields an expected uniform, constant velocity profile, as shown in Figure 1.1(A).

In (B), a shear layer is created by the discontinuity of drag between the canopy and the open water region. An inflection point in the velocity profile is noticed near the canopy top. Two regions are created: one where Kelvin-Helmholtz (K-H) vortices control the vertical transport and shear layer growth, and one with dominating stem-scale eddies, where shear scale energy is converted into wake scale kinetic energy. Adopting the same terminology as Ghisalberti and Nepf (2006), we define three characteristic zones in the vertical (see Figure 1.1B): the stem wake-zone, $0 < z < z_1$, the exchange zone, $z_1 < z < h$, and the upper shear layer, $h < z < z_2$. Since vertical stress gradients become important, Eq. 1.5 becomes:

$$0 = -gS - \frac{\partial \langle u'w' \rangle}{\partial z} - \frac{1}{2}C_d a U^2 \quad (1.8)$$

According to 1.8, estimates of drag require not only accurate measurements of the

free surface slope, but also detailed velocity statistics within the water column, which requires numerous measurements to find mean values representative of the region studied.

In (C), the non-uniformity of the frontal area profiles generates a more complex flow than its rigid counterpart (A). Large vertical gradients of a generate a local, within canopy, shear layer between the upper, more populated region, and the near bottom, sparser one. We keep all terms in Eq. 1.2 to investigate their relevance.

$$W \frac{\partial \langle \bar{u} \rangle}{\partial z} = -gS - \frac{\partial \langle u'w' \rangle}{\partial z} + \nu \frac{\partial^2 \langle \bar{u} \rangle}{\partial z^2} - \frac{1}{2} C_d a U^2 \quad (1.9)$$

Certain macrophyte species, with smaller variations in a along the water column, can resemble simpler, rigid structures. In those cases, Eq. 1.7 does a good job at predicting velocities within the canopy, as shown by Lightbody and Nepf (2006) in their work with *Spartina alterniflora*, but it fails for a non-uniform plant morphology such as Eurasian watermilfoil (Tinoco, 2008).

In (D), structures from the three previous cases appear, resulting in two mixing layers: a canopy scale shear layer at the canopy top, and a smaller scale shear layer within the array. To fully investigate the momentum contributions, we use the same Eq. as for case (C). Difficulties for (C) and (D) increase as plants begin to bend under larger flow rates, as well as sway periodically. When a boundary layer-like flow encounters a submersed vegetated patch, the flow is redirected towards the top of the water column, creating a mixing layer profile due to the higher velocities above the canopy, generating a Kelvin-Helmholtz instability, resulting in a stream of coherent vortices that cause a periodic oscillation of the plants. Such a phenomenon is known as *monami* in aquatic vegetation (Japanese: *mo* = aquatic plant, *nami* = wave), and *honami* (*ho* = cereal) in terrestrial canopies (Ackerman

and Okubo, 1993).

To study the turbulent kinetic energy (tke) budget, fully developed flow is assumed, so all horizontal gradients are neglected, and each term is only a function of z . The temporally- and horizontally-averaged tke equation for all four scenarios can be written as:

$$\frac{\partial k(z)}{\partial t} = T(z) + P_s(z) + P_w(z) - \epsilon(z) \quad (1.10)$$

$$\frac{\partial k(z)}{\partial t} = \frac{\partial}{\partial z} \left[\nu_t \frac{\partial k}{\partial z} \right] - \langle \overline{u'w'} \rangle \frac{\partial U}{\partial z} + \frac{1}{2} a C_d U^2 |U| - \epsilon(z) \quad (1.11)$$

In Eq. 1.10, T represents the transport of kinetic energy, P_s is the production of shear kinetic energy, P_w is the production of wake kinetic energy, and ϵ is the viscous dissipation. Details on the calculation of these values for each scenario studied, are presented and discussed in Chapters 4 and 5.

1.4 Thesis structure

In Chapter 2 we present the details of the laboratory facilities and experimental techniques used for all data acquisition, discussing how different methodologies can yield large variations in the experimental results. Chapter 3 details the design, calibration, and testing of a drag plate, built to get direct measurements of vegetated drag in a laboratory setting. In Chapter 4 we investigate the relationships between drag, characteristic velocities, and other representative parameters for arrays of emergent and submerged rigid cylinders, finding a family of curves to predict the drag coefficients as a function of solid volume fraction. The measured drag values are then used to analyze the momentum and turbulent kinetic energy budgets. In Chapter 5, we present the results and analysis of data from

experiments on flexible, live stems of Eurasian watermilfoil. We investigate the applicability of the predictions from rigid structures in the flexible case, and propose a methodology to estimate forces on patches of vegetation in the field. Chapter 6 summarizes our findings with final conclusions and states new directions for our research.

Chapter 2

Experimental facilities and techniques

2.1 Introduction

In order to fully characterize flow through aquatic vegetation, the most relevant variables involved are measured: flow rate, Q [L^3T^{-1}], mean and turbulent velocities, U_i , u'_i [LT^{-1}]; free surface elevation, η [L], and slope, S [$]$; frontal area obstructed by the rigid or flexible elements, A_f [L^2], as well as the drag exerted by such obstructions, D [MLT^{-2}]. In this chapter we discuss the facilities used for our series of experiments, the design of the arrays of obstructions, and each of the instruments and techniques used to analyze the flow. Unless stated otherwise, 95% confidence intervals (CI) for the random components of the uncertainty are calculated from the data records using a bootstrap method (Efron and Tibshirani, 1993). Bias errors are estimated using the root-sum-square (RSS) technique described by Kline and McClintock (1953).

2.2 Recirculating open channel flumes

The experiments were conducted at the DeFrees Hydraulics Laboratory (Hollister Hall, Cornell University), in two existing recirculating type open channel flumes with glass sidewalls and SAR acrylic beds, ideal for optical access from all sides. The initial experiments for testing and validation of the drag plate, presented in chapter 3, were conducted in a 4.50m long, 0.60m wide flume. Studies on arrays of rigid cylinders and live stems, reported in chapters 4 and 5, were conducted in an 8.00m long, 0.60m wide flume, which allowed us to study submergence ratios of $H/h = 1.00$, 1.25, and 1.80 (Figure 2.1). The notation H/h , as opposed to h/H , is adopted for consistency with recent works on canopy flow, as well as to make it clear that elevations at $z/h < 1$ are within the canopy, while elevations at $z/h > 1$ are above the canopy.

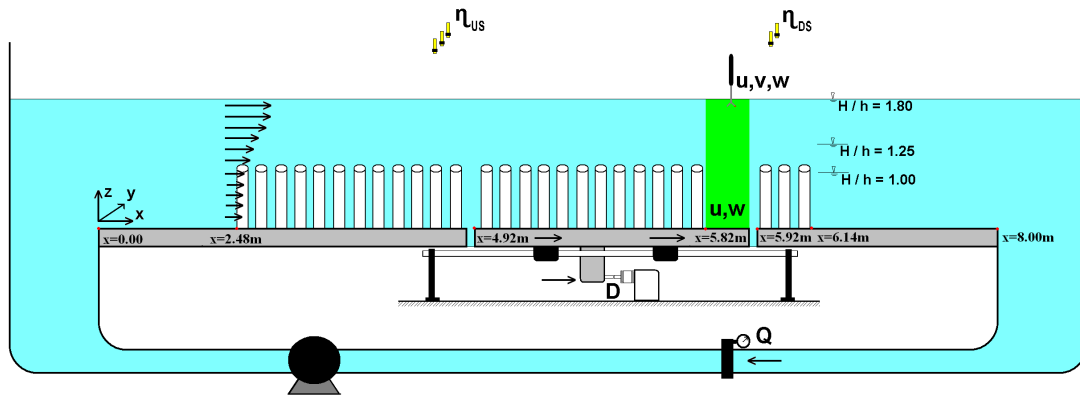


Figure 2.1: Sketch of the 8m long, recirculating, open channel flume used to carry out the experiments reported in chapters 4 and 5.

Both facilities are supported by tilting steel frames, allowing bed slopes of -0.25% to $+2\%$. For our experiments, the bed slope is set to 0% . The flow is driven by centrifugal pumps controlled by variable frequency inverters. For simplicity in the notation, each experiment is initially identified by the frequency at which it was conducted (e.g., Q_{02} is the flow rate measured with the pump running at

a frequency of $2Hz$, and so on). Both flumes were designed with a $1.00m$ by $0.30m$ removable section of the floor, where the drag plate is installed as detailed in Chapter 3.

2.3 Arrays of rigid cylinders

Three PVC plates, $6.3mm$ thick, $1.22m$ long, and $0.60m$ wide, fitted with a random array of vertical rigid cylinders, were placed on the bottom of the flume creating a $3.66m$ long patch for each cylinder diameter. Random arrays of $h = 0.20m$ tall, rigid, acrylic cylinders (US Plastics Corporation, OH, USA) were created assigning only the number of elements per unit area and the minimal spacing allowed between cylinders centers, $s_{min} = 2d$, as follows:

1. Create a rectangular grid, with $\Delta x = \Delta y = 0.1d$ of the size of the PVC plate ($1.22m$ by $0.60m$).
2. Choose the locations for the total number of cylinders in each plate, N_p , using a uniform random distribution.
3. Each time a location is selected, it must satisfy: a) a distance of at least $d + 0.32$ (cm) from the edges, and b) at least $2d$ from the closest occupied grid point (i.e. $2d$ from center to center of the cylinders).

By having the same pattern on each PVC plate we impose a periodic array, repeating itself every $1.22m$.

Four commercial cylinder diameters were chosen, $d = \{1/8", 1/4", 1/2", 1"\}$ ($0.32, 0.64, 1.27, \text{ and } 2.54\text{cm}$, respectively, Figure 2.2). Since some variation was observed in the diameter of the elements, sets of 100 elements of each diameter were measured to determine the exact dimensions. The measured values, shown in Table 2.1 with their respective 95% confidence interval (CI), are slightly smaller ($\approx 0.1mm$) than their nominal values. Given the requirements of the computer

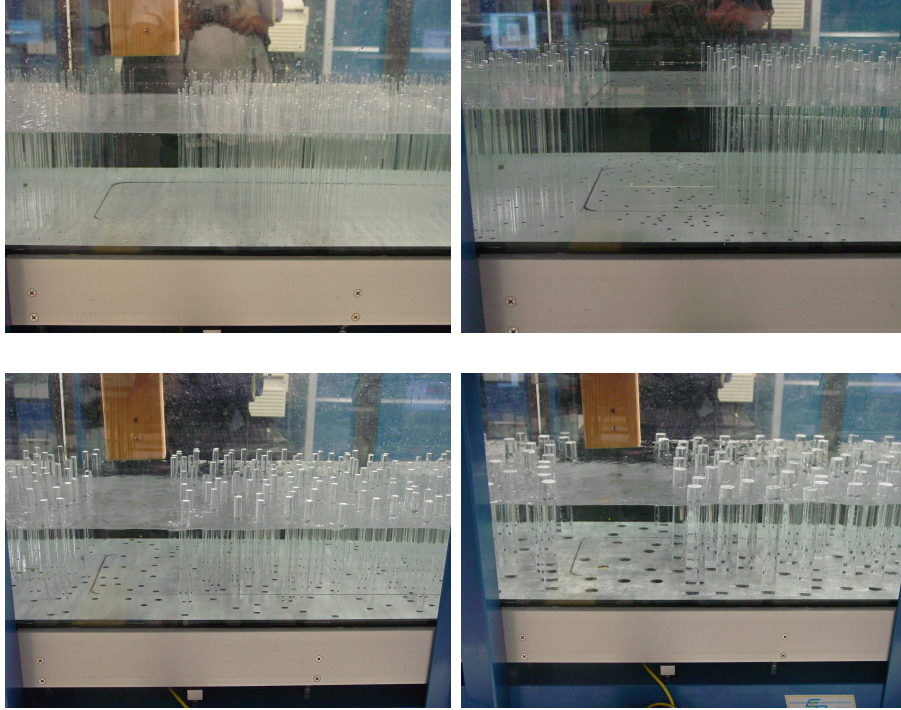


Figure 2.2: Side view of the acrylic cylinder arrays. Measured diameters $d = \{0.31, 0.62, 1.27, 2.53\}cm$ (from top-left to bottom-right).

numerical control (CNC) machine, perforations on the PVC plates were made at 122, 246, 500, and 990 thousandths of an inch (0.310, 0.625, 1.270, and 2.515cm, respectively). Number of elements per PVC plate, N_p , volumetric frontal area, a (m^{-1}), porosity, η_p , solid volume fraction, ϕ , and the resulting space averaged mean separation (center to center distance) between adjacent cylinders, s_n , are shown in Table 2.1.

Table 2.1: Representative parameters for the cylinder arrays.

diameter (mm)	N_p	a ($1/m$)	η_p	ϕ	s_n/d_i
$d_1 = 3.07 \pm 0.15$	921	4.0	0.99	0.01	4.83
$d_2 = 6.15 \pm 0.09$	460	4.0	0.98	0.02	3.67
$d_3 = 12.66 \pm 0.20$	230	4.0	0.96	0.04	2.89
$d_4 = 25.31 \pm 0.25$	115	4.0	0.92	0.08	2.39

2.4 Arrays of flexible, live stems

Stems of Eurasian watermilfoil (*Myriophyllum spicatum*) were harvested from the marsh at the Cornell University Experimental Ponds Facility, Site II (Neimi Road), with the help of Robert L. Johnson, Manager of Cornell Experimental Ponds. The stems were harvested with the roots still attached, and later washed, hand selected, and cut to the specific height ($\sim 25\text{cm}$) as shown in Figure 2.3.



Figure 2.3: Harvesting Eurasian watermilfoil stems. Stems were washed, hand selected, and cut to the required length for the experiments.

Three plant population densities were investigated, $n = \{100, 300, 500\} \text{stems}/\text{m}^2$. Common field conditions fall within $100\text{--}300 \text{stems}/\text{m}^2$ (Robert L. Johnson (2008), personal communication). We originally planned to begin at $n = 500$ and reduce the number of stems until $n = 50$ to cover a full order of magnitude, but the density at $n = 50$ would have been too sparse to get data comparable with the other densities.

The arrays were created following a similar process as for rigid cylinders. Instead of placing plants as individual stems, in order to better represent natural conditions, they were arranged in clumps from 3 to 7 stems, following a normal distribution ($\mu = 5, \sigma = 2$). To generate the random array, we assumed the diameter of each clump to be 2.5cm , and assigned a minimal separation of $2d$, using the same spacing algorithm as with rigid cylinders. For consistency with the rigid cylinder experiments, the same length of the flume was covered, creating a 1.22m

long patch, and repeating it two more times to create the 3.66m long patch. Part of the set up process as well as a top and side view of the placed stems are shown in Figure 2.4. Table 2.2 shows the number of stems, N_p , and number of clumps, N_{cp} , per 1.22m long patch. Values of frontal area, porosity, and solid volume fraction require a different approach, as detailed in section 2.7.

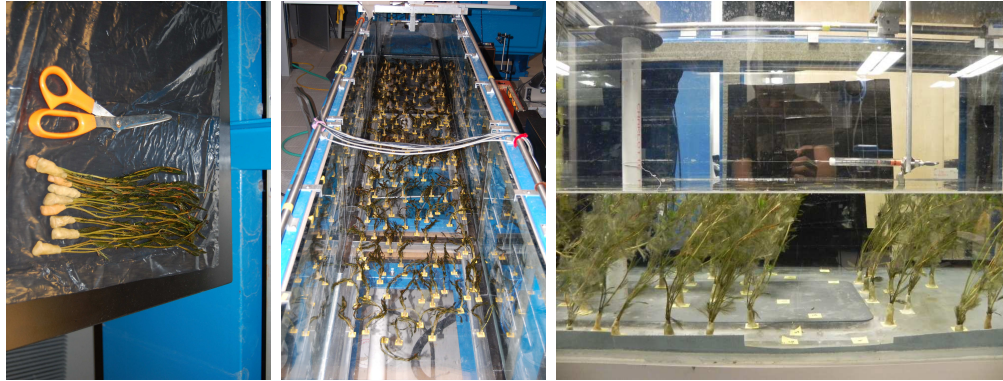


Figure 2.4: Stems being arranged in 3-7 elements per clump (left), and randomly placed with a minimal separation of 5cm (center). Side view of the $n = 500stems/m^2$ configuration at $H/h = 1$ (right).

Table 2.2: Representative parameters for the flexible arrays. Number of stems and clumps per 4ft long patch (N_p and N_{cp} respectively), and actual number of stems on the drag plate (N_{sdp}).

n ($stems/m^2$)	N_p	N_{cp}	N_{sdp}
500	366	74	122
300	220	44	75
100	74	16	29

2.5 Flow rates

Each flume is equipped with an in-line Venturi flow meter (Lo-Loss PMT-IP series, Badger Meter Inc.), constructed of a fiberglass reinforced polyester resin body, and a precision machined PVC throat section, with differential pressure sensors to

monitor the water flow rate in the channel in real time. The difference between a high and low pressure port is reported in units of inches of water column, Δh , and updated every three seconds. Each value is manually recorded to get 3 or 4 minute long records (60 or 80 samples) for each test. The flow equation and the discharge coefficient given from the manufacturer are:

$$Q = K \frac{\pi d_v^2}{4} \sqrt{2g \frac{\Delta h}{12}} \quad (2.1)$$

$$K = \frac{C}{\sqrt{1 - (d_v/D_v)^4}} \quad (2.2)$$

$$C = 0.8221 \quad (2.3)$$

where g is the gravity acceleration, and $D_v = 0.3048m$, and $d_v = 0.1770m$, are the entrance diameter, and the throat diameter of the Venturi meter, respectively. The worst case accuracy specified by the manufacturer is expected to be $\pm 0.75\%$ of the reported Δh .

2.6 Velocities

Particle image velocimetry (PIV) measurements of the 2-D velocity field in the $x-z$ vertical plane were taken over the entire flow depth in the field of view (FOV) shown in Figure 2.1 at 3 transverse sections for the rigid cylinders $y = \{0.14, 0.30, 0.56\}m$, and at 7 sections for the flexible plants, $y = \{0.09, 0.16, 0.23, 0.30, 0.37, 0.44, 0.51\}m$. Two PIV systems were used.

For the shorter (4.5m long) flume, the image plane was illuminated by a frequency doubled twin-head Nd:YAG laser (Spectra Physics PIV200-10) and a cylindrical lens expanding the beams on the $x-z$ plane. The laser operated at 10Hz on each head with the time between pulses ranging from 8ms to 36ms according to

the flow speed. Images were acquired with an SMD-Dalsa 1M60-20 digital camera (1024×1024 pixel array, 12 bit/pixel), fitted with a Nikon 60mm f/2.8D AF Micro-Nikkor lens. Image acquisition was performed by Vision Now software (Boulder Imaging Inc., CO). For the emergent and submerged experiments, the 1024×1024 pixel images gave us resolutions between $0.18\text{mm}/\text{pixel}$ and $0.36\text{mm}/\text{pixel}$.

For the longer (8.0m long) flume experiments, an Argon-Ion laser (Innova 90 Series Ion Laser, Coherent Inc.), in multi-line mode was used. The laser was operated in light regulation mode at an output power of 4.5W. The light sheet was created by a scanning mirror (Model 6860, Moving magnet capacitive position detector optical scanner, Cambridge Technology). A computer controlled shutter (Model LS200, nmLase Products, Inc.) was located immediately after the laser and operated to insure that only a single scan by the scanning mirror was allowed to illuminate the image plane per camera frame exposure. The camera and image acquisition system were the same as for the shorter flume studies.

Images are post-processed for instantaneous velocity, using a central-difference form (Wereley and Meinhart, 2001) of the dynamic sub-window PIV technique outlined in Cowen and Monismith (1997). Final PIV processing is carried out on a 32×32 pixel subwindow with a 75% overlap. Stray vectors are removed using an adaptive Gaussian filter and a local median filter (Cowen and Monismith, 1997). Temporally- and horizontally-averaged vertical profiles of velocity statistics (e.g., $U(z)$, $\langle u'w'(z) \rangle$, $\langle k(z) \rangle$) are obtained by averaging over the x -direction (along horizontal rows of subwindows from the $\sim 10\text{cm}$ field of view), and then averaging over the 3 to 7 transverse, y -sections.

Additional measurements were taken with a Nortek Vectrino acoustic Doppler velocimeter (ADV), equipped with + (“plus”) firmware option, at a 50Hz frequency for the drag plate experiments reported in chapter 3, and 200Hz for the experiments in chapters 4 and 5. The location of the ADV measurements varied through

the experiments, from only a few transverse points at a given x and z location to check for lateral variability, to a full $y-z$ grid to study the flow three-dimensionality and generation of secondary currents.

2.7 Frontal areas

Frontal areas are straight forward to calculate for the rigid cylinders array based on the known diameter, submerged length, and number of cylinders. A different approach is required for real plants. Quantitative imaging is used to measure the area obstructed by the live plants as a function of elevation, and fluid velocity, $a = f(z, U)$.

Two approaches were taken:

1. Stems of length $L \simeq 0.25m$ were placed in a fish tank with the same water depth as the emergent case experiments ($H = 20cm$). Pictures of individual stems (10 in total), as well as clumps of 3 to 7 stems (5 of each) were taken and analyzed to obtain mean profiles of frontal area (Figure 2.5). A vegetated threshold (VT) to separate vegetated pixels from the background was manually obtained for each set of images. Using a white background, the threshold was sharp enough to capture even the thinnest structures of the stems. Each stem was later measured to obtain wet and dry weights (oven-dried for 48 hours at $60^\circ C$), the former to estimate the volume of the plants, and thus solid volume fraction ϕ , and the latter for biomass calculations (Figure 2.6). The volume of each stem and group of stems is calculated from their wet weight and the specific gravity of Eurasian watermilfoil ($SG_{Ew} = 0.8$, Koegel et al., 1973), as $V = W_w / (SG_{EW}\rho_0)$, where ρ_0 is water density.

As shown in Figure 2.7(A), a linear relationship is found between the total frontal area (i.e., from the whole stem) of each stem and clump measured and

their dry weight, $W_d(mg) = 2.5 \times 10^6 a(cm^{-1})$. This relationship allows us to use field biomass data to estimate a total value of a , and subsequently use our mean vertical profile per stem $a_s(z)$ (Figure 2.7(B), obtained from averaging the vertical profiles of all the individual stems and clumps photographed) to estimate the actual vertical profile, $a(z)$, correspondent to the reported field conditions (e.g., for a reported biomass $B_m(g/m^2)$, we calculate the total a from Figure 2.7(A), and use the mean vertical profile per stem $a_s(z)$ (Figure 2.7(B)), to calculate the actual vertical profile, $a(z) = X \cdot a_s(z)$, such that $\int_0^h X \cdot a_s(z) dz = a$). It is expected that similar relationships can be found for other plant taxa, which will help create a field-lab model with empirical biomass-frontal area curves for different species, to facilitate communication between field, laboratory, and numerical researchers.

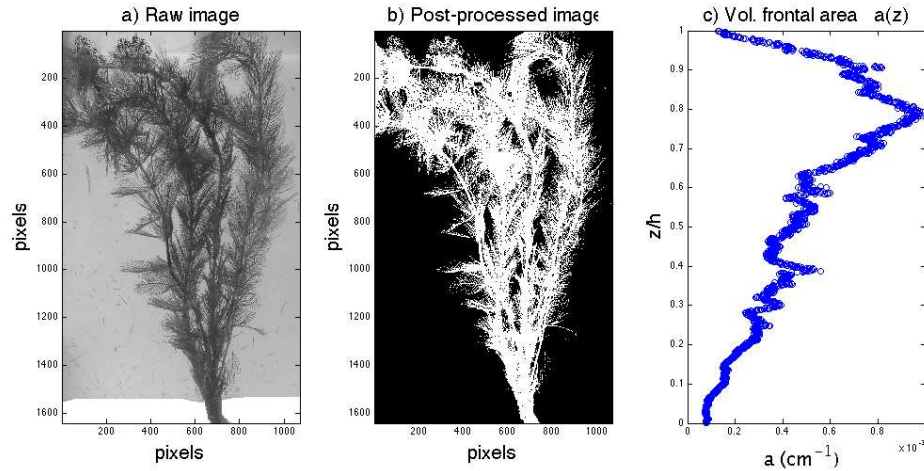


Figure 2.5: Determination of frontal area. a) Raw images of submerged plants, b) post processed binary images, c) calculated vertical profile of a .

2. A second approach includes the effects of velocity on the bending of the plants and subsequent effect on frontal area. As seen in Figure 2.8 for the $n = 500 stems/m^2$ emergent case, the stems bend as the flow rate increases, acquiring a more streamlined position to offer less resistance to the flow. To account for such variations, a mirror was placed downstream of the plant canopy, at a 45 degrees

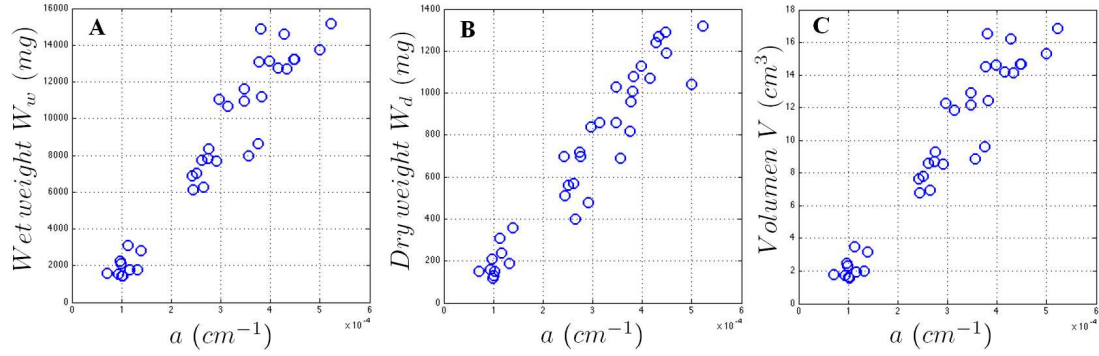


Figure 2.6: A) Wet weight, B) dry weight, and C) volume, as a function of volumetric frontal area, a . Data taken from images of 10 single stems and of 5 clumps each of 3 to 7 stems.

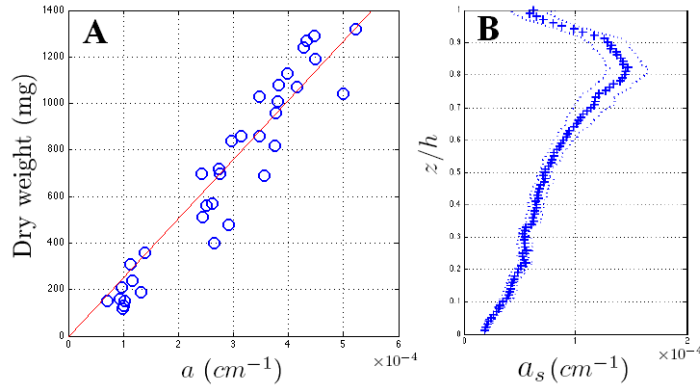


Figure 2.7: A) Relationship between biomass (measured dry weight) and total volumetric frontal area (per m^2). B) Vertical profile of the mean value of $a(z)$ for a single stem (per m^2)

angle allowing a camera to take pictures from the side (Figure 2.9), thus capturing a frontal view of the stems. To ensure that only the last rows of stems affected the measurement, the pictures were taken with the lights off, while two slide projectors, situated at opposing sides of the flume, illuminated the stems on the final 20cm of the canopy .

Pictures were taken at each flow rate, capturing 4 images per second for 2 minutes. The VT is chosen iteratively by eye, until we find the value that reproduces the original images the closest. In the first approach, the plants in the fish tank with a white background had a sharp VT. In the second approach, with the plants



Figure 2.8: Side view of the downstream edge of the $n = 500 \text{ stems}/m^2$ plant array with increasing flow from left to right.

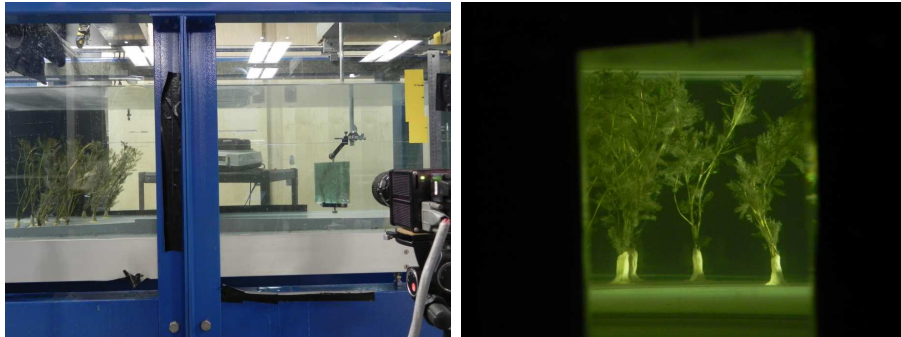


Figure 2.9: Camera focused on a mirror placed at 45° downstream of the plant canopy (left). View from the camera location with lights off and slide projectors on each side of the flume (right).

experiencing the flow, VT is not as sharp, and part of the fine structure of the leaves is lost, especially at higher flow rates when the stems bend, preventing a uniform illumination on all the leaves. However, even for the worst cases, we still capture a good mean value, as shown in Figure 2.10 (for $n = 500 \text{ stems}/m^2$, Q_{16} , fully submerged, see Section 5 for details). To investigate the sensitivity of our algorithm to the choice of VT, we present the vertical profiles of a obtained by varying the VT by ± 2 , and ± 5 , as shown in Figure 2.10. It is noticed that in the more populated region, the worst case variations will be of the order of 10 and 20% respectively. However, location and magnitudes of the vertical gradients, as well as the canopy height, do not present significant variations.

Analysis of the images provides not only mean vertical profiles as a function of velocity (Figure 2.11), but also time variations (Figure 2.12) which evince periodic

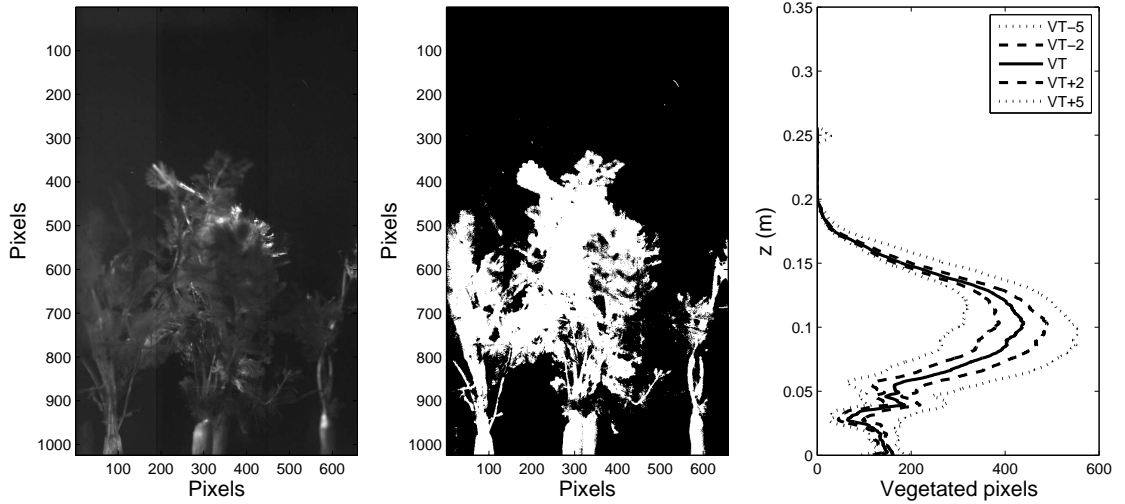


Figure 2.10: Raw and processed images of frontal area (flow directed out of the page), and uncertainty from the choice of the vegetated intensity threshold (VT), by varying the chosen VT by ± 2 and ± 5 intensity units.

waving of the stems (*monami*). As the plants bend and h decreases, their biomass is concentrated over a smaller region, with more vegetated material obstructing the flow near $z = h$. However, since the leaves on the branches are also bending in the direction of the flow, the observed frontal area is actually reduced as the flow rate increases. Further analysis of the results and their effects on the flow, as well as representative velocities for each case are presented and discussed in Chapter 5 (Tables 5.1 and 5.2).

2.8 Free surface slopes

Measurement of the free surface slopes deserves special attention, as it is the most common method of determining the available energy to the flow. The free surface slope is often used to estimate drag in emergent vegetation (See Eq. 1.7 in Section 1.3). It is often measured by either resistance type surface displacement gages (Nepf, 1999; Tanino and Nepf, 2008a; Augustin et al., 2009), or ultrasonic, acoustic wave gages (Barnes et al., 2009). However, the location of the measurements differs

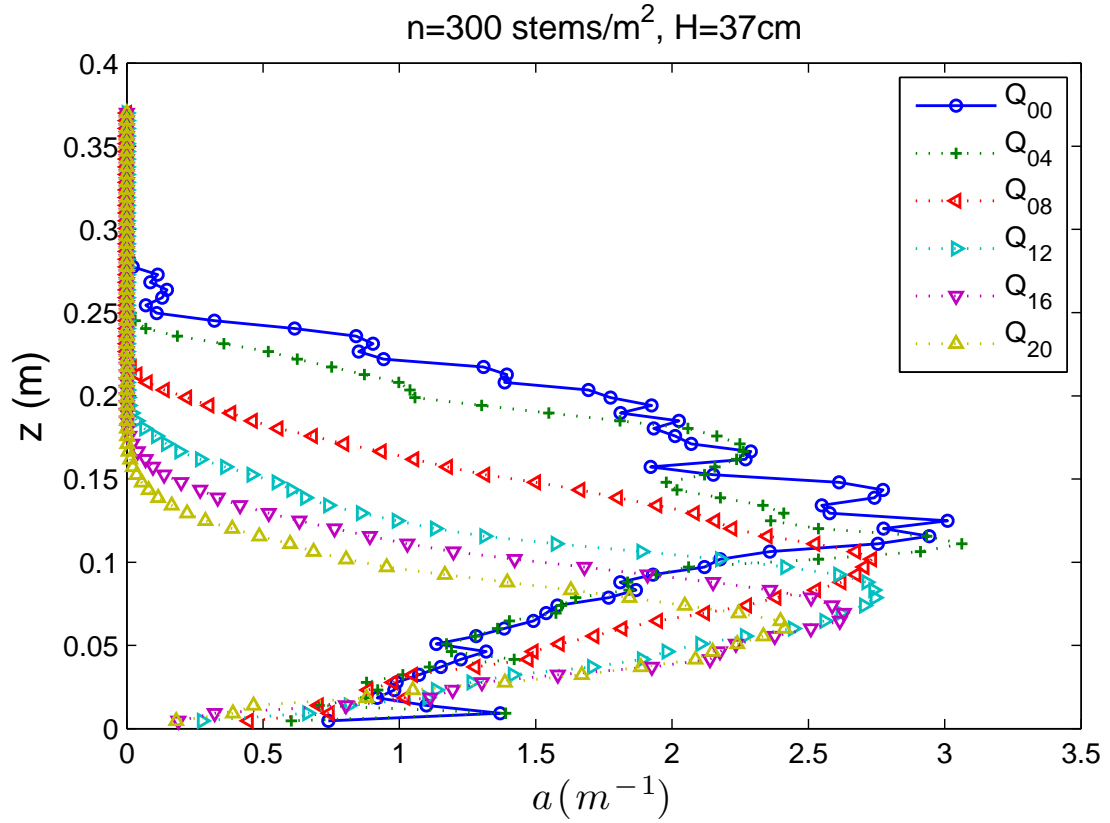


Figure 2.11: Variations in frontal area with increasing flow rates, from $Q_{00} = 0m^{3/s}$ to $Q_{20} = 0.035m^{3/s}$. Uncertainty bars, with a worst case of $\pm 10\%$ (Figure 2.10) are omitted for clarity.

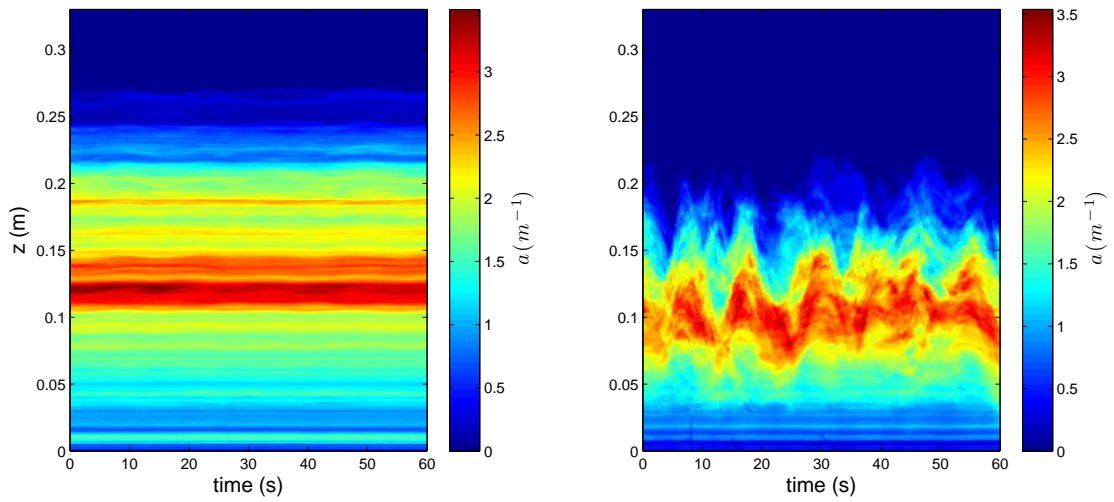


Figure 2.12: Time records of $a \text{ (m}^{-1}\text{)}$ for increasing flow rates ($Q_{02} = 0.0031m^{3/s}$ and $Q_{08} = 0.0140m^{3/s}$), for the $n = 300\text{stems/m}^2$ case, $H = 0.37\text{m}$.

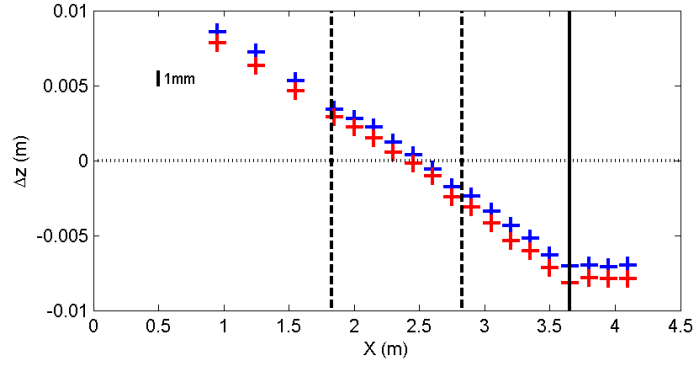


Figure 2.13: Measured surface displacements with an array of 7 ultrasonic wave gages spanning the width of the flume at 19 x -locations, for the $d=0.64\text{cm}$ cylinders array with $U_Q=14.37\text{cm/s}$. Dashed line marks the edges of the drag plate. Solid line marks the end of the cylinders array. For simplicity only maximum and minimum values at each x -location are presented

from study to study, from only two centerline points, up- and downstream of the array (Dunn et al., 1996; Nepf, 1999), to sets of 2 or 3 lateral measurements at two points within the length of the array (Tanino and Nepf, 2008a). To identify the expected variations due to the number and location of the gages, and optimize our own measurements, we used an array of 7 ultrasonic wave gages (S18U Series, Banner Engineering Corp.), and take 5 minutes long, 50Hz records at 19 locations along the length of the array, as shown in Figure 2.13. What we observed is a relatively high variation of $\sim 1\text{mm}$ between the lowest and highest point on each y -transect, as well as a dramatic change in the slope at the downstream edge of the array, demonstrating that a) a single centerline measurement is not sufficient, and b) measurements have to be taken within the length of the array only, to avoid violations in the assumption of one-dimensional flow.

Based on the results from Figure 2.13, measurements of the water depth for the rigid and flexible arrays were conducted with arrays of 3 and 2 wave gages, at the up- and downstream edges of the drag plate respectively, unless stated otherwise for specific cases.

2.9 Drag

A main goal of our research is to directly measure the drag on arrays of rigid and flexible elements. The details of the drag plate, built specifically for such a purpose, are presented in chapter 3.

2.10 Conclusions

Careful considerations must be made in the selection and implementation of each measurement technique. This has to be considered when comparing data from different studies, since changes in even the location of the instrumentation relative to the arrays in the case of velocities and free surface slopes, or the use of different methodologies for determination of obstructed area, or different mechanisms to estimate or measure drag, create differences in the results that might lead to inaccurate interpretations. One of our goals is to produce an extensive data set, with rigid and flexible vegetation, for both submerged and emergent conditions, acquired in a consistent way, expected to be used as a benchmark for current and future modeling efforts.

Chapter 3

Direct and indirect measurements of boundary stress and drag on simple and complex arrays of elements

3.1 Introduction

The measurement of boundary stress and form (pressure) drag are critical components of investigations of fluid-structure interactions. Forces acting on aquatic vegetation can induce breaking and uprooting of stems, scour the bottom, and control mixing rates of nutrients and pollutants that will directly affect both the plants and the organisms to which they provide habitat. While a variety of methods have been used to measure each of boundary stress and form drag, both directly and indirectly, their measurement remains challenging due to the potential for strong local gradients, the effects of unsteadiness (e.g., wave induced flows), the motion or deformation of the object of interest (e.g., bending of plants), the need to make measurements exceedingly close to boundaries, and the complex interactions of wakes when multiple objects are sufficiently close (e.g., flow through plant

canopies). As discussed by Ackerman and Hoover (2001), methods to estimate the boundary stress include calculation from the mean velocity profile, momentum balance, or pressure differences at the boundary layer (i.e., Preston-tube). Other near-wall methods require more specialized equipment, such as oil-film interferometry, a surface fence, a wall hot wire, or a wall pulsed wire (see Fernholz et al., 1996, for details).

When dealing with the fluid drag exerted on objects, similar indirect approaches are often taken, using velocity and pressure data to calculate the drag, but the problem is potentially more complex due to the strong local gradients, both in pressure and viscous drag (e.g., at the separation points on bluff bodies). The use of embedded sensors within objects is primarily restricted to large-scale experiments (Wienke and Oumeraci, 2005) but with the increasing availability of arrays of MEMS sensors it may soon be possible to instrument relatively small scale objects. However, such procedures are spatially intensive, as the gradients in pressure and wall stress must be resolved in all directions of variation, which results in a rapid increase in cost, complexity, and time required to test different elements and configurations. If multiple objects are involved the costs will likely be prohibitive for the foreseeable future.

Researchers have addressed the direct measurement of drag in different ways, depending on whether the focus of the study was to produce a device capable of measuring drag in the field (e.g., Callaghan et al., 2007), or to design a laboratory device able to measure the drag in physically modeled conditions close to the natural conditions (e.g., Sand-Jensen, 2003; Fathi-Maghadam and Kouwen, 1997). The present work focuses on the latter, to measure the drag while reproducing natural conditions in a well controlled experimental set up, able to accommodate a wide range of velocities, geometries, and configurations.

Our goal is to design a non-intrusive, easy to use device, simple to calibrate,

that requires minimal maintenance, and allows for the straight-forward mounting of different multi-object, potentially highly complex configurations. The developed device, dubbed a drag plate, allows the direct measurement of wall stress (drag force over the area of the plate), the drag on individual objects, as well as the drag that arises from complex arrays of objects. Among the important factors considered in the drag plate design were that calibration should be insensitive to significant variations in vertical loading and intrusive support structures were to be avoided (Khalak and Williamson, 1996; Sand-Jensen, 2003).

The drag plate is large enough to spatially average the drag over several elements, providing more representative mean values of drag, as opposed to measuring forces on a single element (Fathi-Maghadam and Kouwen, 1997; Freeman et al., 2000; Callaghan et al., 2007). Barnes et al. (2009) demonstrated that a large shear plate can yield accurate direct measurements of shear stress. We extend this concept to an open channel by mounting a drag plate on an air-bearing-rail system external to the facility test section. The plate is isolated from the facility test section by a thin gap made water tight with a thin membrane. The force experienced by the drag plate is monitored by a load cell mounted to the test section frame. We present a more robust, simple, and yet powerful system for measuring drag in complicated flows, such as vegetated flows, natural rough boundary layers, coastal structures, and urban canopies.

3.2 Design and calibration

The specified drag plate has dimensions $L = 0.995m$ long and $B = 0.296m$ wide, just smaller than the specified opening in the facility bed, which is $1.000m \times 0.300m$. This specific size was chosen due to the intention of measuring the drag on aquatic plant canopies and the need to average over multiple plants at various plant stem

densities. The drag plate consists of three layers: 1) an upper smooth flat PVC plate maintained at the same elevation as the test facility bottom, in contact with the fluid, to which can be attached single or multiple elements, 2) a bottom stainless steel metal plate to provide rigidity, and 3) a thin, flexible, elastic, abrasion resistant, 0.15mm (0.006in) thick, latex rubber membrane sandwiched between the PVC and stainless steel plates, that seals the gap between the flume and the drag plate (Fig 3.1). The latex rubber membrane performed satisfactorily for each of the experiments presented in this chapter, but was easily punctured by debris, and required to be replaced in more than one occasion. For later experiments in the longer flume, it was replaced with a 0.25mm (0.010in), liquid silicone rubber (BISCO Silicones, Rogers Corp.), which was found to be less prone to tearing and punctures.

The drag plate rests on four mounting blocks that each terminate in an air bearing (NewWay air bearings, PA, USA). The air bearings ride on a pair of 25.4mm (1in) diameter precision stainless steel shafts mounted to the facility frame, parallel to the longitudinal direction of the facility, allowing essentially frictionless displacement in the direction of motion, as shown schematically in Fig. 3.2.

The drag plate system was mounted within the bed of an existing 4.50m long, 0.600m wide recirculating type open channel flume with glass sidewalls and an SAR acrylic bed in the DeFrees Hydraulics Laboratory in the School of Civil and Environmental Engineering at Cornell University. The center of the drag plate is located 2.30m from the facility inlet and laterally on facility centerline. The flume is supported by a steel frame and the structure of the drag plate device that holds the stainless steel shafts is mounted securely to this steel frame, allowing fine vertical adjustment to ensure that the drag plate surface is flush with the flume bed surface.

A rigid stainless steel rectangular cantilevered beam is mounted to the bottom

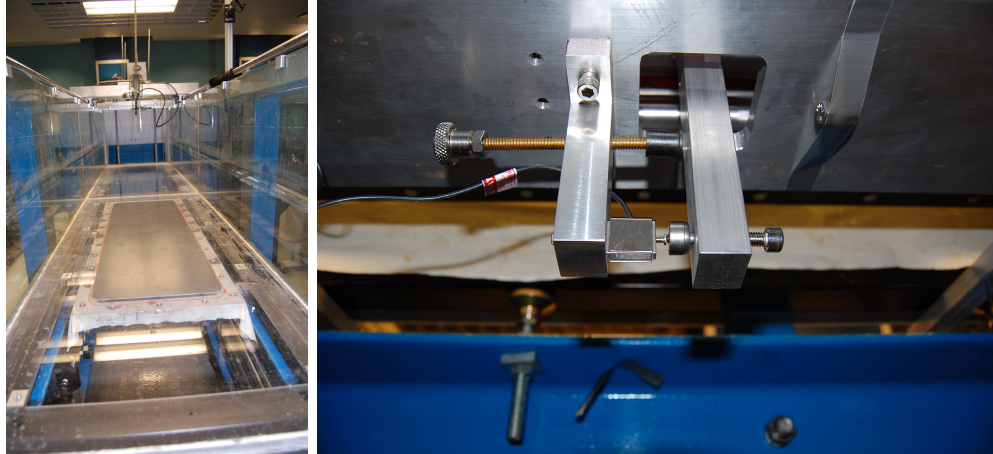


Figure 3.1: Left: View of the drag plate installed in the 4.5m open channel flume from above and upstream. The top PVC plate, sandwiched latex membrane, and an O-ring and mounting screws (coming through the membrane from below) are visible. Right: View from below and to the side of the drag plate. As the flow displaces the plate (flow is from right to left), the beam connected to the drag plate (rightmost beam) is forced against the load cell mounted to the leftmost beam which is attached to the fixed frame.

of the drag plate and set to be just in contact with a 100g, S-beam load cell (Cooper Instruments and Systems, VA, USA) mounted to the fixed frame, as shown in Fig. 3.1 (right). The load cell is connected to a National Instruments data acquisition system to sample the output voltage.

Calibration of the drag plate is performed by applying a known force in the direction of motion on a vertical rod mounted to the topside of the drag plate. A series of increasing known forces are applied using a spring scale with a 95% confidence interval of $\pm 0.005N$. The process is performed both with an empty flume, $h = 0m$, and at the working water depth, $h = 0.18m$, to investigate the repeatability of the results under the same horizontal loading conditions, and their dependence on vertical loading of the plate. The load cell is sampled for 30 seconds at $50Hz$ starting 30 seconds after the known force is applied. The results for all calibrations are consistent and yield the same linear calibration curve, independent of h , as shown in Fig. 3.3. Values of the recorded voltage output from the load

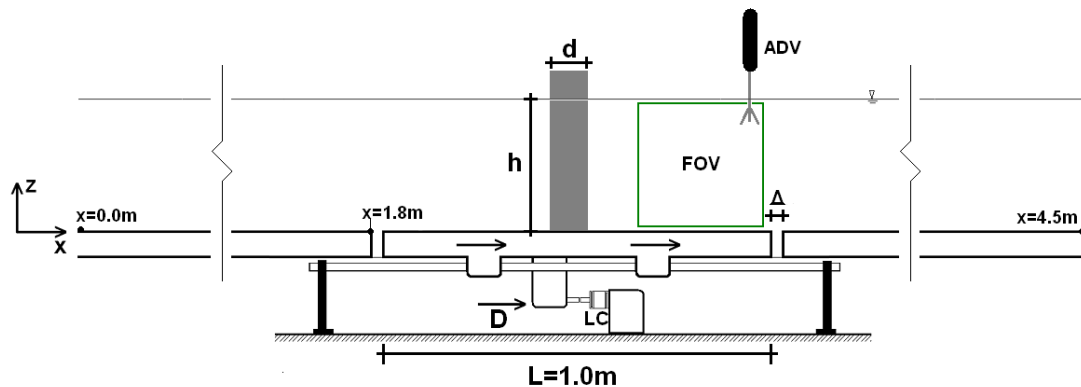


Figure 3.2: Schematic elevation of the drag plate. The location of the test cylinder of diameter d , and the field-of-view (FOV) of the PIV measurements are shown. An ADV is located at the downstream edge of the drag plate. Flow is from left to right, the gap Δ allows the plate to displace freely, thus applying the drag force D onto the load cell LC.

cell to an applied force of $F = 0.50N$ for each of the five test cases shown in Fig. 3.3 are given in Table 3.1, along with the bootstrap determined 95% confidence interval (Efron and Tibshirani, 1993).

Figure 3.3 also shows the results of calibrations taken just before each of the experiments described in the following sections. It is noted that the exact slopes, $m = -2.00mV/N$ (Fig. 3.3 left) and $m = -1.54mV/N$ (Fig. 3.3 right), differ substantially, due to a required replacement of a punctured latex membrane. However, the new calibration shows the expected linearity and repeatability.

Table 3.1: Drag plate calibration. Recorded values for an applied force of $F = 0.50N$.

	Mean value (mV)	95%CI (mV)
cal.1, $h = 0.00m$	-0.9895	± 0.0027
cal.2, $h = 0.00m$	-1.0056	± 0.0026
cal.3, $h = 0.18m$	-0.9696	± 0.0037
cal.4, $h = 0.18m$	-0.9854	± 0.0040
cal.5, $h = 0.18m$	-0.9777	± 0.0040

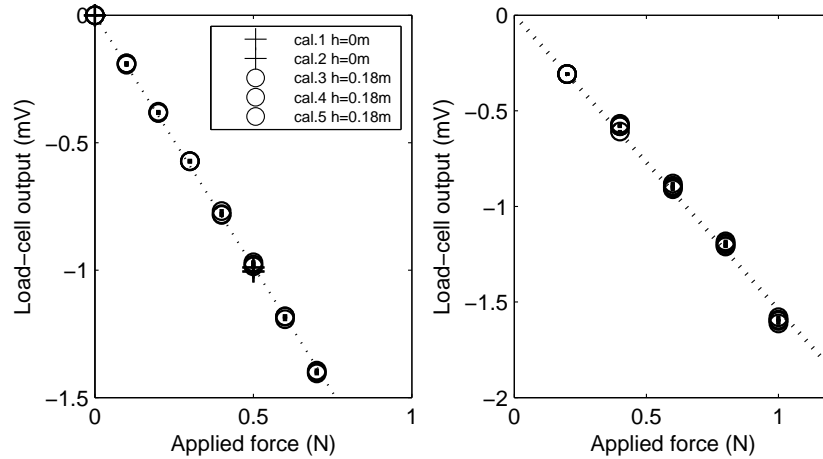


Figure 3.3: Left: calibration curve for the drag plate. Study for linearity, repeatability, and water depth dependence. Right: Calibration curve for the drag plate for the studies on drag induced by a flat plate boundary layer and flow past a rigid cylinder. Vertical bars represent the 95% confidence interval.

3.3 Validation experiments

Two series of validation experiments were performed in the 4.5m open channel flume on well studied and documented cases: drag induced by a turbulent flat plate boundary layer and drag induced by flow around a rigid cylinder. A third series of experiments, measuring the drag on arrays of randomly placed rigid cylinders, is presented to show the power and applicability of the drag plate on more complex flows. For each series of experiments the facility was filled to a flow depth of $h = 0.180m$ and multiple flow rates, driven by three variable frequency controlled centrifugal pumps, were tested. For each measurement, the load cell on the drag plate was sampled at $50Hz$. A developing flat plate boundary layer was established at five increasing flow rates. Simultaneous particle image velocimetry (PIV) measurements of the 2-D velocity field in the $x - z$ vertical plane were taken over the entire flow depth (see Fig. 3.2). The FOV was illuminated by a frequency doubled twin-head Nd:YAG laser (Spectra Physics PIV-200-10) operating at 10 Hz on each head with the time between pulses (Δt) ranging from 16.00ms down

to $4.00ms$ with increasing flow speed. The laser beams were expanded within the $x - z$ plane using a cylindrical lens. Images were acquired by an SMD-Dalsa 1M60-20 digital camera (1024×1024 pixel array, 12-bit/pixel) fitted with a Nikon 60mm f/2.8D AF Micro-Nikkor lens. Image acquisition at $20Hz$ was performed by VisionNow software (Boulder Imaging Inc., CO) producing $10Hz$ velocity fields, which were collected in 200s records at each flow rate. Images were post-processed for instantaneous velocity, using a central-difference form Wereley and Meinhart (2001) of the dynamic sub-window PIV technique outlined in Cowen and Monismith (1997). Final PIV processing was carried out on a 32×32 pixel subwindow with a 75% overlap yielding a 124×116 ($x \times z$) array of velocity vectors.

3.3.1 Flat plate boundary layer verification test

The PIV velocity fields were averaged in time and horizontally in space to produce vertical profiles of the various metrics of the velocity. Turbulence quantities were calculated based on Reynolds decomposition, i.e., $\xi'_i = \langle \xi_i \rangle - \xi_i$ where ξ is the instantaneous quantity of interest, $\langle \ \rangle$ indicates the linear process of temporal and horizontal averaging, and ξ' is the instantaneous turbulent fluctuation about the mean quantity $\langle \xi \rangle$.

Vertical profiles of the non-dimensional longitudinal velocity $u^+ = \langle u(z) \rangle / u_*$ are shown in Fig. 3.5 for all five runs, which are characterized by their momentum thickness Reynolds numbers, $Re_\theta = U_0\theta/\nu$, where U_0 is the free stream velocity taken as the maximum in $\langle u(z) \rangle$ and θ is the momentum thickness, defined as (Kundu and Cohen, 2004)

$$\theta = \int_0^\infty \frac{\langle u(z) \rangle}{U_0} \left(1 - \frac{\langle u(z) \rangle}{U_0} \right) dz. \quad (3.1)$$

The friction velocity, u_* , is calculated by extrapolation of a linear fit to the

Reynolds stress profile, $\langle u'w'(z) \rangle$, in the range $0.1 < z/h < 0.25$ to the bottom of the flume to estimate the wall stress, τ_w (Fig. 3.4). The friction velocity is then calculated as $u_* = \sqrt{\tau_w/\rho}$, where ρ is the density of water. The wall-scaled longitudinal mean velocity profiles closely follow the log-law

$$u^+ = \frac{1}{\kappa} \ln z^+ + B \quad (3.2)$$

where $z^+ = u_* z/\nu$ and ν is the kinematic viscosity of water, with the von Kármán constant $\kappa = 0.41$, and $B = 5.5$ (Cowen and Monismith, 1997; Pope, 2000) as well as the direct numerical simulation (DNS) data of Spalart (1986) which were carried out at $Re_\theta = 1410$.

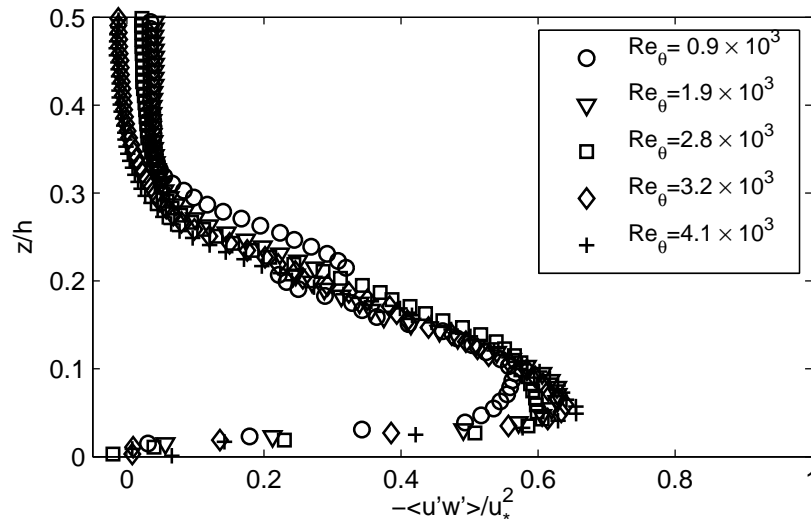


Figure 3.4: Normalized Reynolds stress profiles $\langle u'w' \rangle$ for all Re_θ .

The output from the load-cell was sampled at $50Hz$ for $5min$ for each test. The sample records are time averaged and the final calibration (Fig. 3.3) is applied to convert the mean voltages to mean forces. The time averaged drag force, D , is shown in Fig. 3.6 as a function of the mean velocity. Figure 3.6 also shows the drag force estimated from τ_w determined from the PIV measured velocity

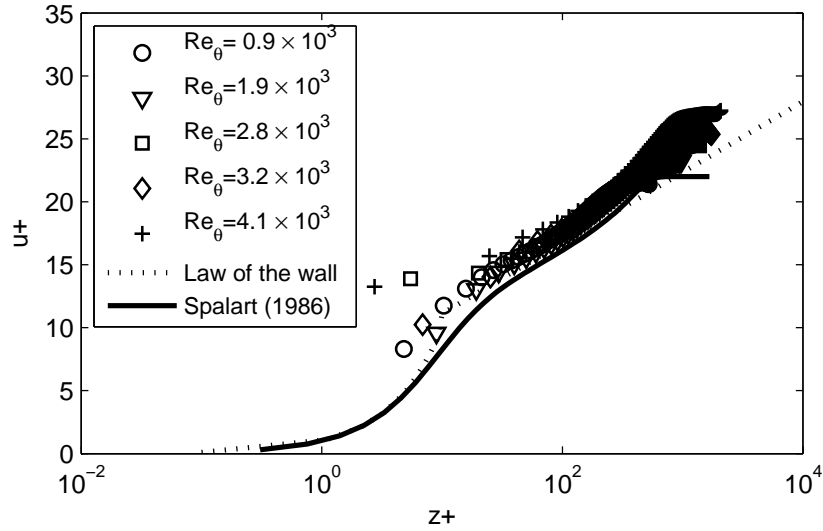


Figure 3.5: a) Normalized longitudinal mean velocity profiles $u^+ = \langle u \rangle / u_*$: PIV experimental data (open symbols); Spalart (1986) data (solid line), and the law of the wall, $u_+ = \frac{1}{0.41} \log(z_+) + 5.5$ (dotted line).

profiles, assuming a uniform wall stress over the surface of the drag plate, $A = 0.995m \times 0.296m$, such that the drag force on the plate is determined as $D = \tau_w \cdot A$. Assuming a uniform wall stress, equal to the measured stress at the downstream edge of the drag plate, results in an underestimation of drag, since as the boundary layer thickens as it advances along the drag plate, the associated velocity gradients near the bottom decrease, generating a reduction on the wall stress as x increases from the edge of the plate. Using the Schultz-Grunow formula (Pope, 2000) we can calculate an x -dependent skin-friction coefficient, $c_f(x) = 0.370(\log_{10} Re_x)^{-2.584}$, with $Re_x = Ux/\nu$, and a mean c_f over the drag plate $c_f = \frac{1}{L} \int_0^L c_f(x) dx$, to estimate the total drag force on the plate as $D_{S-G} = A \cdot \tau_{S-G}$, where $\tau_{S-G} = \frac{1}{2} \rho U^2 c_f$. The results are presented for comparison in Figure 3.6.

Both the direct drag measurements and the estimated values based on τ_w are seen to follow the expected quadratic velocity drag force relationship, using the depth integrated velocity, $U = \frac{1}{h} \int_0^h u(z) dz$, as the characteristic velocity (Equation 3.3).

$$C_d = \frac{2D}{\rho U^2 A} \quad (3.3)$$

The actual drag coefficients from the shear plate, C_{dsp} , can be calculated from Eq. 3.3, and a comparable skin friction coefficient, C_{dws} (Eq. 3.4), can be calculated from the determined wall stress for comparison.

$$C_{dws} = \frac{\tau_w}{\frac{1}{2}\rho U^2}. \quad (3.4)$$

When plotted against Re_θ both measured and estimated coefficients fall within the same range and show a decreasing trend as Re_θ increases (Figure 3.6). As seen in Table 3.2, the drag force measurement for the lowest velocity considered ($Re_\theta = 948$) is of the same order as the measurement uncertainty, which propagates into the calculation of C_d , as seen in Figure 3.6. For the described drag plate configuration, this represents the drag force where the signal-to-noise ratio is approximately 1.

Table 3.2: Directly measured drag force induced by flat plate boundary layer, its uncertainty, and relative error.

	D (N)	δD (N, from 95%CI)	$\delta D/D$
U_1	0.0020	± 0.0017	0.82
U_2	0.0153	± 0.0028	0.19
U_3	0.0336	± 0.0021	0.06
U_4	0.0543	± 0.0023	0.04
U_5	0.0881	± 0.0020	0.02

3.3.2 Single rigid cylinder verification test

A rigid cylinder was fixed at the center of the drag plate, as shown in Fig. 3.2. A series of tests were conducted at the same flow rates as were used in the flat plate trials across four cylinder diameters: $d = \{12.7, 25.4, 42.1, 76.5\}mm$.

The measured drag forces are shown in Fig. 3.7. The results follow closely the

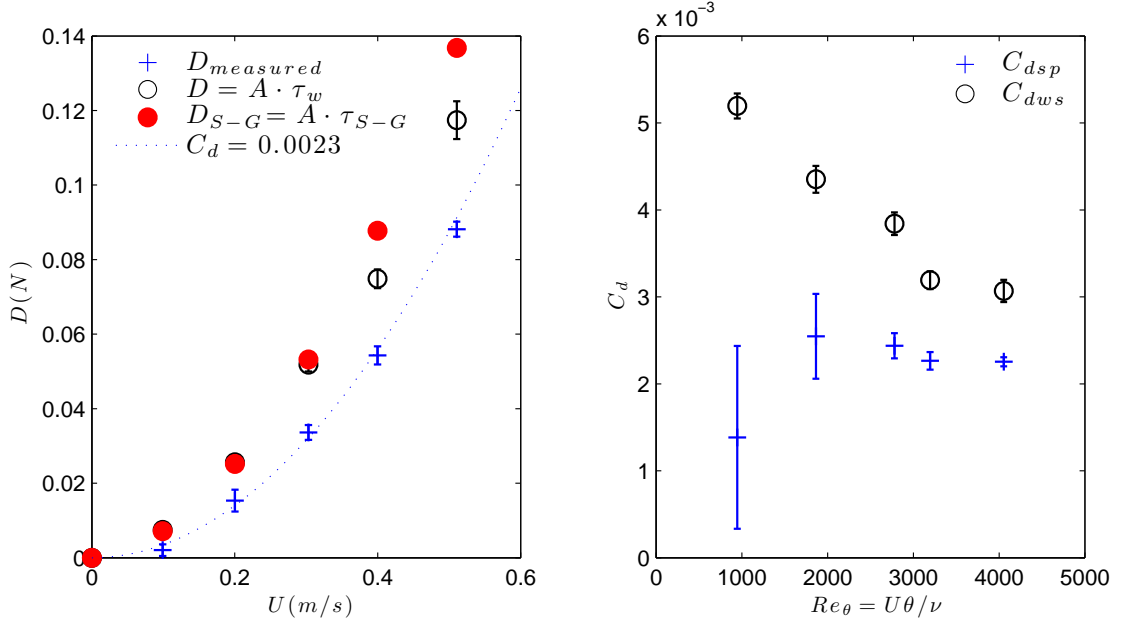


Figure 3.6: Left: drag force on the drag plate: direct drag measurements (+), and drag estimates from τ_w (open symbols) and τ_{S-G} (solid symbols). Right: flat plate boundary layer drag coefficients calculated from a) direct measurements on the drag plate (+), and b) the determined τ_w (o) Vertical bars represent 95% CI.

expected quadratic power law (Equation 3.5) when using a constant value of the drag coefficient, $C_d = 1.2$ (note the diameter based Reynolds number, $Re_d = \frac{Ud}{\nu}$, range is approximately $10^3 - 5 \times 10^4$, as seen in Fig. 3.7, where C_d is expected to be constant).

$$D = \frac{1}{2}C_d\rho dhU^2 \quad (3.5)$$

The depth averaged velocity, after a continuity-based correction for the obstructed area of the cylinder is:

$$U = U_m \left(\frac{W_f}{W_f - d} \right), \quad (3.6)$$

with $W_f = 0.60m$ being the width of the flume, and U_m the measured depth averaged velocity.

A noticeable deviation arises for the $d = 76.5mm$ cylinder at $U = 0.34m/s$

case, during which lateral standing waves formed, due to a resonance between the Kármán vortex shedding frequency and low-mode lateral standing waves, and contributed to changes in the induced drag force.

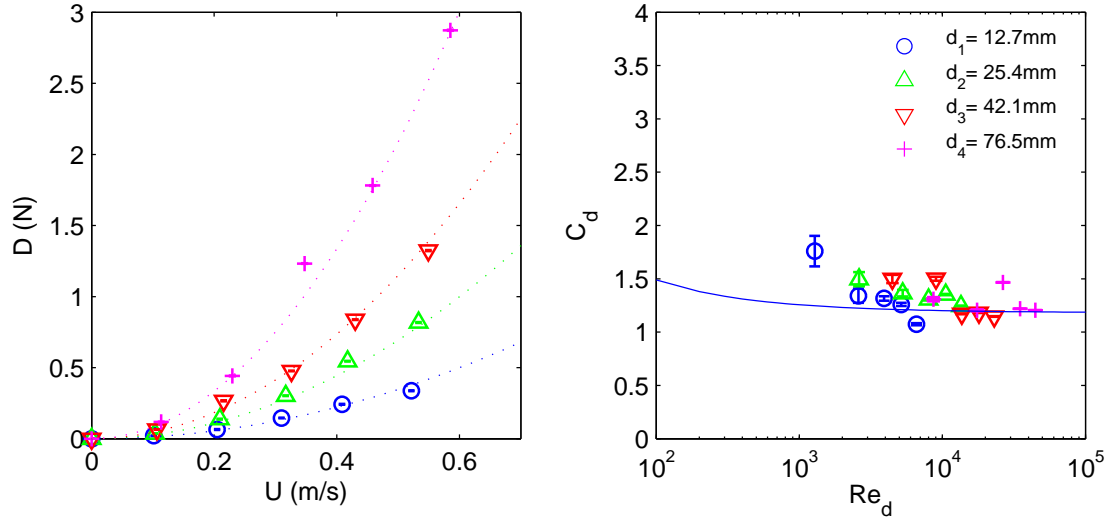


Figure 3.7: Left: drag force on a rigid cylinder. Symbols represent measured drag force for different cylinder diameters. Dashed lines calculated based on Eqn. 3.3 with $C_d = 1.2$. Right: measured drag coefficients for rigid cylinders at various Re_d . Solid line calculated from Sucker and Brauer (1975) curve fit to Schlichting (1979) data. Vertical bars, smaller than the symbols for most D and C_d values reported, represent 95% CI, .

The individual drag coefficients, as a function of Re_d , are calculated using the measured drag force and correspondent depth averaged velocities from Eqn. 3.5, and the results are presented in Fig. 3.7. The values collapse into a single curve, with values close to those expected from the classic studies of Schlichting (1979), represented in Figure 3.7 by the approximation of Sucker and Brauer (1975).

The continuity adjusted (Eqn. 3.6) depth integrated PIV estimates of U , were verified against the characteristic Strouhal velocity determined from the frequency of the periodic vortices formed in the Kármán vortex street in the wake of the cylinders. Given the Re_d range of $10^3 - 5 \times 10^4$, the Strouhal number $St = fd/U$, where f is the shedding frequency, is expected to be constant with a value $St = 0.21$

(Schlichting and Gersten, 2000). The shedding frequency, f , was measured from the peak of the lateral velocity spectra calculated from a Nortek Vectrino acoustic Doppler velocimeter (ADV - shown in Fig. 3.2). The ADV was sampled at 50Hz for 327.68s and the characteristic velocity determined as $U_{St} = fd/0.21$ from the ensemble averaged spectra (each record was split into 8 non-overlapping records for ensemble averaging). U_{St} was found to be equivalent to U to within 3% on average; their mean ratio across the twenty experiments is $U_{St}/U = 0.969$ with a 95% confidence interval of ± 0.024 .

3.3.3 Arrays of rigid cylinders

Work on arrays of rigid cylinders will be discussed in detail in chapter 4. Here we analyze the response of the drag plate to temporal variations generated by the cylinders, proving its ability to resolve not only mean unidirectional forces, but also high frequency and periodic variations.

A distinct and interesting feature of the flow through arrays of rigid elements was captured, which allowed us to test the temporal response of the drag plate. Lateral standing waves, as shown schematically in Figure 3.8 for the first two wave modes, were observed at specific velocity ranges at three of the four cylinder diameters studied.

Wave generation by vortex shedding is reported and studied by Zima and Ackerman (2002) and Ghomeshi et al. (2007). Their work is focused on estimating the wave amplitude, based on the dimensions and number of cylinders in regular and staggered arrays within the flow. We show the occurrence of the phenomenon in random arrays, and focus on the ability of the drag plate to resolve it. However, further research will allow us to expand on existing work, to predict the generation and effects of such lateral waves in random arrays, at different submergence ratios,

as functions of d and a .

The natural frequencies of the flume of width B , for a specific water depth H , are calculated using the gravity wave dispersion relationship to solve for the wave radian frequency ω (Eq. 3.7), using the expected wavelength $\lambda = 2B/n$, for each wave mode n , as well as the wave number $k = 2\pi/\lambda$, wave period $T = 2\pi/\omega$, and frequency $f = 1/T$. The expected frequencies are thus calculated using Eq. 3.8.

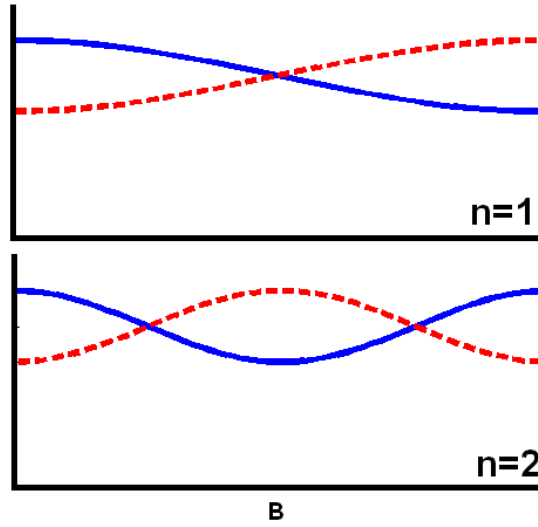


Figure 3.8: Sketch of the modes 1 and 2 of the lateral standing waves observed in the flume.

$$\omega^2 = kg \tanh(kH) \quad (3.7)$$

$$f = \frac{1}{2\pi} \left(\frac{\pi n}{B} g \tanh\left(\frac{\pi n B}{H}\right) \right)^{1/2} \quad (3.8)$$

The onset of the waves occurs when the shedding frequency of the cylinders nears a natural frequency of the flume. The flow speeds at which the standing waves are expected to appear are easily estimated from the frequencies obtained above. As mentioned in section 3.2, the flows analyzed in the present study fall in the range where the Strouhal number (Eq. 3.9) has a constant value $St \simeq 0.21$. Since the frequencies in Eqs. 3.8 and 3.9 must be the same for the waves to occur,

we combine both equations to get a simple method to estimate the wave-generating mean velocities as a function of wave mode n , cylinder diameter d , flume width B and water depth h , as shown in Eq. 3.10.

$$St = f_s d / U \quad (3.9)$$

$$U = \frac{d}{0.42\pi} \left(\frac{\pi n}{B} g \tanh\left(\frac{\pi n H}{B}\right) \right)^{1/2} \quad (3.10)$$

The consistency of the frequencies is apparent by analyzing the frequency spectra of the transverse velocity, S_v , measured drag, S_D , and surface elevation, S_η . The coincidence in the peak values for the three calculated spectra in two of the studied cases are shown in Figure 3.9. The expected frequencies for modes $n = 1$ and $n = 2$ according to Eq. 3.8 are 0.96 and 1.57, respectively, which is just 4% larger than the measured values of 0.92 and 1.52 in Fig. 3.9.

The drag plate accurately captures the high frequency variations due to the waves, providing valuable insight as to how the different wave modes affect the drag on the submerged cylinders. The mean value of the free surface at the two most central wave gage locations $y = \{0.265, 0.350\}m$, can be used to calculate a time dependent drag as a function of the time dependent water depth, as shown in Eq. 3.11.

$$C_d(t) = \frac{D(t)}{\frac{1}{2}\rho N_{dp} d \cdot h(t) \cdot U(t)^2} \quad (3.11)$$

$$h(t) = \bar{h} + \eta(t) \quad (3.12)$$

$$U(t) = \frac{Q}{Bh(t)(1 - \phi)} \quad (3.13)$$

It is clearly apparent that the drag plate responds to the variations in the water level. As the water depth increases over the drag plate the drag increases and vice versa. Calculating $C_d(t)$ yields a time series with the same periodic oscillations

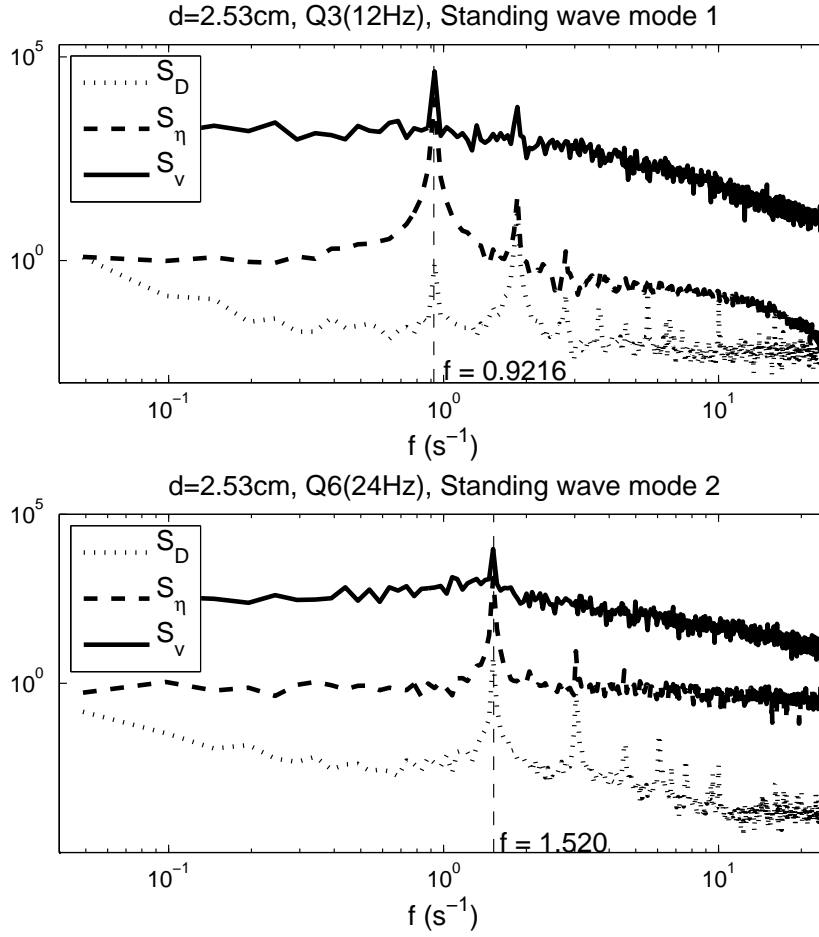


Figure 3.9: Drag spectra, S_D , elevation spectra, S_η , and velocity spectra, S_v , for the wave modes $n = 1$ (top) and $n = 2$ (bottom).

as the drag records, which can be averaged over the entire record ($t > 5min$) to obtain more accurate mean values.

3.4 Conclusions

The drag plate yields accurate measurements for values of the drag force greater than $0.01N$ (see Table 3.2). Such small drags are only typical of pure flat plate boundary layer induced wall stress at low speeds (0.1 m/s in the present case) and when interested in the drag force on submerged objects (such as the single rigid

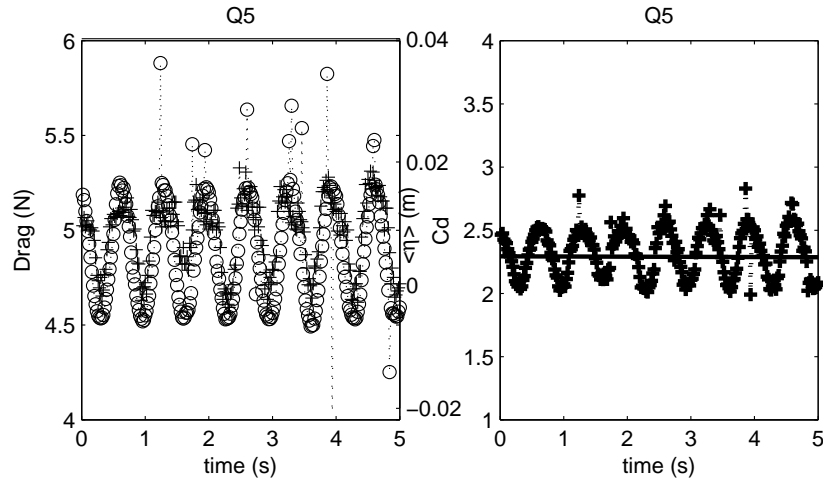


Figure 3.10: Time variations of the drag D (+) and free surface elevation η (o) (Left), and calculated C_d (Right) for one of the flow rates considered for $d_4 = 0.0253m$. Solid line indicates the mean C_d over the whole time series (5 minutes long sample records).

cylinder in the present study) the minimum drag expected is at least an order of magnitude greater (see Figure 3.7). If one were interested in smaller drag forces they could likely be accommodated by either a larger area for a wall stress to act over or if point forces are the concern, then a smaller membrane and hence less internal energy to overcome to apply a force on the load cell. The drag plate also proved its ability to capture high frequency variations, as shown by its ability to resolve the standing waves occurring under resonant conditions in the cylinder array experiments, providing valuable insight as to how the different wave modes affect the drag on the emergent elements. The device has been demonstrated to be capable of accurately measuring drag forces in the phenomena that motivated its design: vegetated flow, natural rough boundary layers, and coastal structures.

The flexibility of the drag plate design allows it to be installed to test different configurations of multiple elements with varying geometries and physical properties, as needed. The dimensions of the drag plate were chosen to fit without modification all of the open channel and wave tank facilities in the DeFrees Hy-

draulics Laboratory, which greatly expands the research areas in which the device will be used. Further modifications will allow the device to measure bi-directional drag forces in oscillating flows, an area of study with significant need of drag force measurement, both on man-made structures and the natural environment, such as sea grass canopy patches.

While the primary purpose of the drag plate is to contribute to state of the art research, it is also a powerful teaching tool and is currently being used in laboratory experiments in a large undergraduate introductory fluid mechanics course.

The drag plate concept has been demonstrated to be well suited for the required tasks. Its usefulness has been proven for the low signal-to-noise ratio application of pure wall stress measurements, and at higher signal-to-noise ratio conditions such as flow past a circular cylinder. The experiments detailed in this Chapter clearly demonstrate the drag plate facility has the desired characteristics of: accuracy, repeatability, lack of intrusion on the flow, and simplicity of use for different geometries and configurations, as shown for randomly generated, cylinder arrays in the present study; such characteristics make it a powerful tool in the study of the physical processes on natural streams, coasts and wetlands, in which vegetated drag, rough boundary layers due to living organisms, and the design of coastal structures are a wide and evolving field of research.

Chapter 4

Flow through and above arrays of rigid cylinders

4.1 Introduction

The use of rigid cylinders has become common practice for laboratory experiments on model vegetated flow. The work from Dunn et al. (1996) has been used as a benchmark for numerical models, such as those of Lopez and Garcia (1997, 1998, 2001). Former and current researchers from Dr. Heidi Nepf's group at MIT have conducted extensive research on arrays of submerged and emergent cylinders from 1997 to date (e.g., Nepf, 1999; Lightbody and Nepf, 2006; Ghisalberti and Nepf, 2006; Tanino and Nepf, 2008a). Other authors, such as Stone and Shen (2002), and Poggi et al. (2004c), have used a similar approach to study vegetated flows.

Predictions of drag and drag coefficients for arrays of rigid cylinders are often conducted by calculating a bulk or height dependent C_d from the simplified momentum equations (Eq. 1.7 and 1.8) or assuming a constant drag coefficient of order one. The latter approach over-simplifies the problem by neglecting all interactions between cylinder wakes and shear-scale eddies, using the same C_d as

for a single element, while the former approach requires accurate, high resolution data in both time and space to get mean, representative parameters of the flow.

We bypass the assumptions required to calculate C_d from velocity statistics, and directly measure the drag, using the device already tested and verified in Chapter 3). Coupling the drag measurements with a detailed analysis of the velocity field, using both quantitative imaging for 2-dimensional velocity data, and ADV measurements to investigate the three-dimensionality of the flow, we generate an extensive data set that allows us to investigate how the measured values match the estimated values from common approaches.

Analysis of the generated data set for different diameters and solid volume fractions allows us to develop our own predictions of C_d as a function of ϕ and Re_d .

4.2 Experimental procedure

A $3.66m$ long section of an $8m$ long open channel flume is covered by an array of rigid, $0.20m$ long acrylic cylinders, as detailed in Section 2.3. Four different arrays are studied, with the same initial $a = 4.0m^{-1}$, with $d_i = \{0.31, 0.62, 1.27, 2.53\}cm$. To study the effects of the variation in a , several cylinders are removed from the $d_2 = 0.62cm$ array to obtain values of $a = \{1.0, 2.0, \text{ and } 3.0\}m^{-1}$. Relevant parameters for each array: number of elements per plate, N_p , volumetric frontal area, a , porosity, η_p , solid volume fraction, ϕ , and the space averaged mean separation (center to center) between adjacent cylinders, s_n , are presented in Table 4.1.

Measurements of the 2-D velocity field in the $x - z$ vertical plane were taken using particle image velocimetry (PIV) over the entire flow depth at the downstream edge of the drag plate, using the PIV set-up as detailed in Section 2.6. To gain access to the full field of view (FOV), several array elements had to be

Table 4.1: Representative parameters for the cylinder arrays

d (cm)	N_p	$a(m^{-1})$	η	ϕ	s_n/d_i
$d_1 = 0.31$	921	4.0	0.990	0.010	4.83
$d_2 = 0.62$	460	4.0	0.980	0.020	3.67
$d_3 = 1.27$	230	4.0	0.960	0.040	2.89
$d_4 = 2.53$	115	4.0	0.920	0.080	2.39
$d_2 = 0.62$	116	1.0	0.995	0.005	6.72
$d_2 = 0.62$	231	2.0	0.990	0.010	4.89
$d_2 = 0.62$	346	3.0	0.985	0.015	4.1

removed (Fig. 4.1). To test the effect of the removal of cylinders, we analyzed the 2-dimensional velocity field in the gap, and found no significant changes in the mean longitudinal velocity over its length, consistent with the findings of Ikeda and Kanazawa (1996), indicating that the removal of cylinders had little effect on the measured velocity field. For the emergent case, a single, centerline ($y = 0.30m$) vertical plane is investigated, recording 8200 images at $20Hz$ to get $10Hz$ velocity fields, with time between images, Δt , ranging from $8.00ms$ to $36.00ms$. For the submerged case, three lateral sections are studied, $y = \{0.14, 0.30, 0.46\}m$, and sets of 1030 images are captured at $2Hz$ for the 2 off-centerline locations and sets of 8200 images at $20Hz$ are taken for the centerline location, with a Δt ranging from $8ms$ to $33ms$, yielding $1Hz$ and $10Hz$ velocity fields, respectively. Images are post-processed as detailed in Section 2.6.

4.3 Results from arrays of emergent cylinders ($H = h$)

4.3.1 Analysis of drag and velocities

Eight flow rates were initially studied for each diameter, as shown in Table 4.2, spanning a range of $Re_d = \{50 - 5000\}$. Flow rate, Q , free surface slope, S , and



Figure 4.1: Side view of the cylinder array. Several cylinders had to be removed for optical access. Flow from right to left.

drag, D , were measured for each test. PIV was originally conducted at 6 flow rates for each diameter, but disturbances in the free surface distorted the light sheet directed from above and prevented us from acquiring good quality images at the highest flow rates on the largest diameter cylinders.

Table 4.2: Flow rates Q (m^3/s) as set by the pump frequency f_p (Hz). Characteristic velocity U_Q (m/s), and Re_d are reported.

d_i (cm)	f_p (Hz)	4	8	12	16	20	24	28	32
0.31	Q (m^3/s) $\times 10^{-3}$	2.52	5.50	8.27	11.14	14.05	16.97	19.87	22.50
	U_Q (m/s) $\times 10^{-2}$	2.50	5.45	8.19	11.03	13.92	16.81	19.68	22.28
	Re_d	59	130	194	262	330	399	467	529
0.62	Q (m^3/s) $\times 10^{-3}$	2.18	5.35	8.13	10.99	13.94	16.88	19.63	22.18
	U_Q (m/s) $\times 10^{-2}$	2.19	5.35	8.13	11.00	13.94	16.88	19.63	22.18
	Re_d	104	254	386	522	661	801	931	1050
1.27	Q (m^3/s) $\times 10^{-3}$	2.52	5.35	8.18	11.04	13.91	16.76	19.65	22.46
	U_Q (m/s) $\times 10^{-2}$	2.58	5.47	8.35	11.27	14.20	17.11	20.06	22.93
	Re_d	250	530	809	1090	1380	1660	1940	2220
2.53	Q (m^3/s) $\times 10^{-3}$	2.52	5.20	7.78	10.67	13.47	16.35	18.54	22.07
	U_Q (m/s) $\times 10^{-2}$	2.69	5.54	8.29	11.36	14.35	17.42	19.75	23.51
	Re_d	520	1070	1600	2200	2780	3370	3820	4550

To study the lateral (y) variability of the velocity, point measurements of the 3 components of the velocity (u, v, w) were acquired with an ADV (32,768 samples

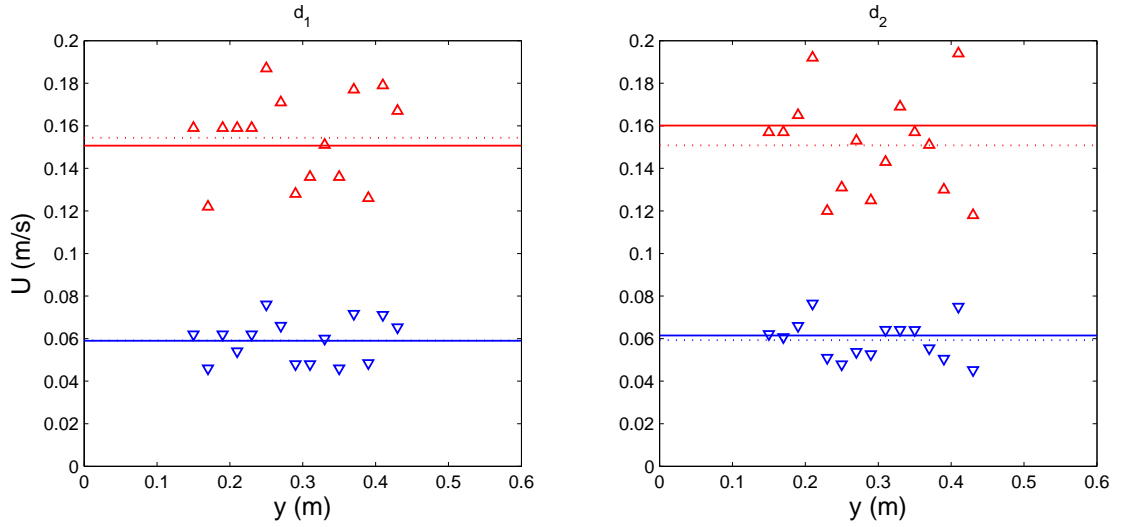


Figure 4.2: ADV measurements of longitudinal velocity, U (m/s), at 15 points along a y -transect, at $z = 0.12m$, for diameters $d_1 = 0.31cm$ and $d_2 = 0.62cm$, at two flow rates. Dotted lines indicate the means of the 15 measurements for each flow rate. Solid lines show the value of their respective measured mean porous velocities U_Q (m/s).

at $200Hz$) at 15 transverse locations at $z = 0.12m$. As shown in Figure 4.2, the longitudinal velocity varies almost 30% with respect to the laterally averaged value, which shows the need for measuring at several locations in order to get a more representative mean value. For rigid, emergent cylinders, it is expected that cylinder drag will suppress vertical gradients (Nepf et al., 1997b; Nepf and Koch, 1999), resulting in almost uniform velocity profiles. Figure 4.3 shows the results from PIV data taken at a single, centerline location, for all diameters, adjusted by a factor $(1 - \phi)^{-1}$ to account for continuity.

To account for the overall spatial variability, given the essentially uniform velocity profiles, a mean porous velocity, U_Q , is defined as:

$$U_Q = \frac{Q}{BH(1 - \phi)} \quad (4.1)$$

Q is measured via a modified Venturi flow meter (see Section 2.5), and H is taken

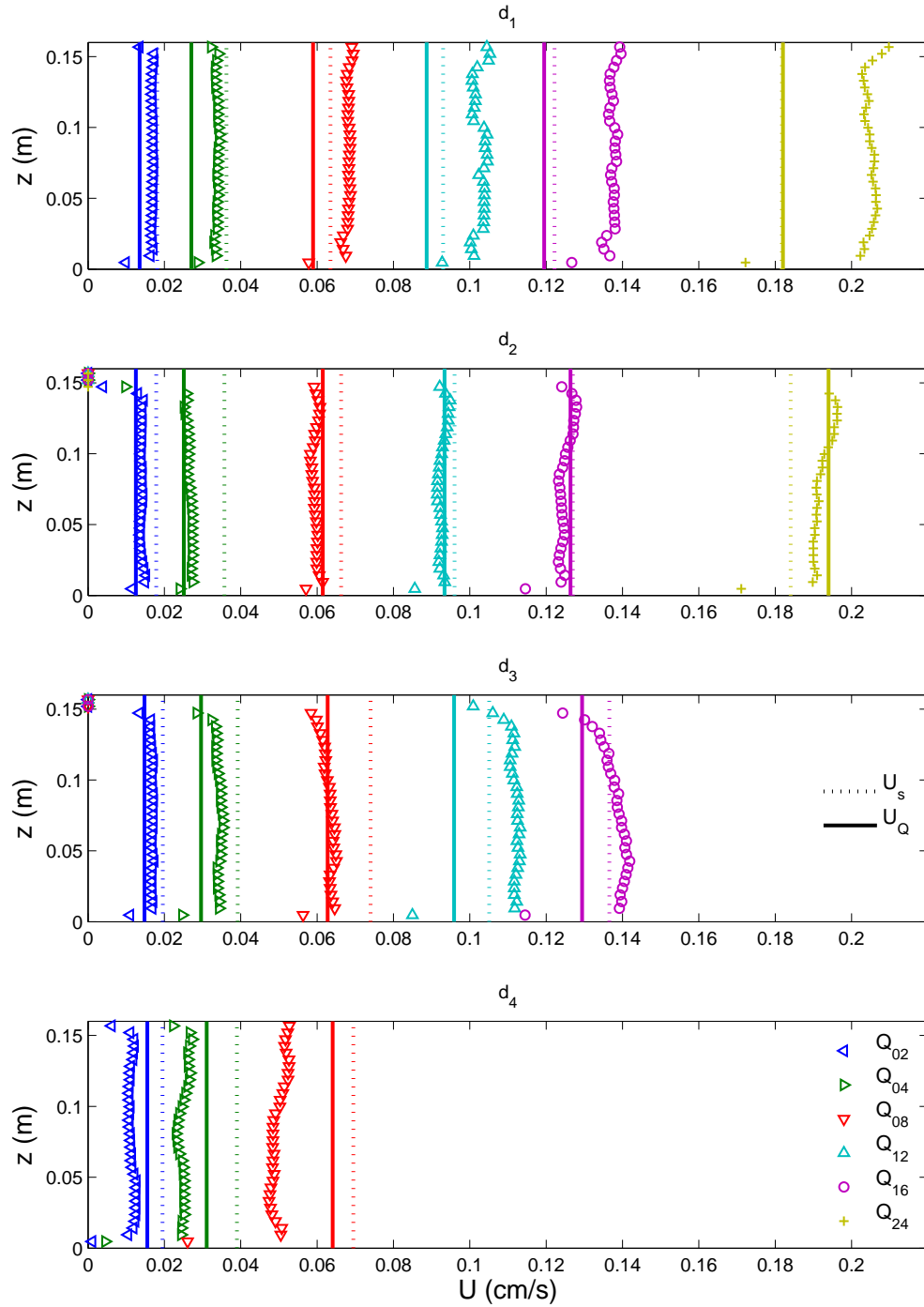


Figure 4.3: Vertical profiles of longitudinal velocity, U (m/s), for emergent, rigid cylinders at all the flow rates studied (open symbols). Dotted lines indicate the estimated velocities from the momentum equation, U_s , and solid lines show the mean porous velocities, U_Q for each flow rate.

as the average water depth over the drag plate. U_Q values plotted in Figure 4.2 show a difference between a laterally averaged velocity and U_Q of up to 6%.

To validate the use of U_Q , since only one lateral section was studied using PIV and hence no lateral averaging can be performed, we compare it against estimated values. Based on Equation 1.7, a mean velocity can be estimated from the measured free surface slope $S = \partial\eta/\partial x$ (Eq. 4.2)

$$U_s = \sqrt{\frac{-2gS(1-\phi)}{C_d a}} \quad (4.2)$$

For a first order estimate, a constant value, $C_d = 1.13$, is used (Dunn et al., 1996), yielding the results in Figure 4.3. The mean porous velocities, U_Q , estimated values, U_s , and depth averaged values of the vertical profiles, U_h , are compared in Figure 4.4. It is now clearly noticed how the ratio U_s/U_Q gets closer to unity as the flow rate increases, attributed to larger uncertainties in the slope measurements at the lowest flow rates. The choice of a constant $C_d = 1.13$ is also a source of uncertainty, a reminder of our main goal to find more accurate ways to estimate drag coefficients. Differences larger than 20% are noticed on the U_h/U_Q ratios, which is expected since only one location was studied. For analysis hereafter, U_Q values are used as representative bulk velocities.

For each test, the load cell output was recorded for 5min at 50Hz. The obtained drag values, D , show a quadratic relationship with the velocity (Figure 4.5). Following a similar approach as with a single cylinder, a drag coefficient can be calculated from Eq. 4.3, where N_{dp} is the actual number of cylinders on the drag plate:

$$C_d = \frac{D}{\frac{1}{2}\rho d h N_{dp} U_h^2} \quad (4.3)$$

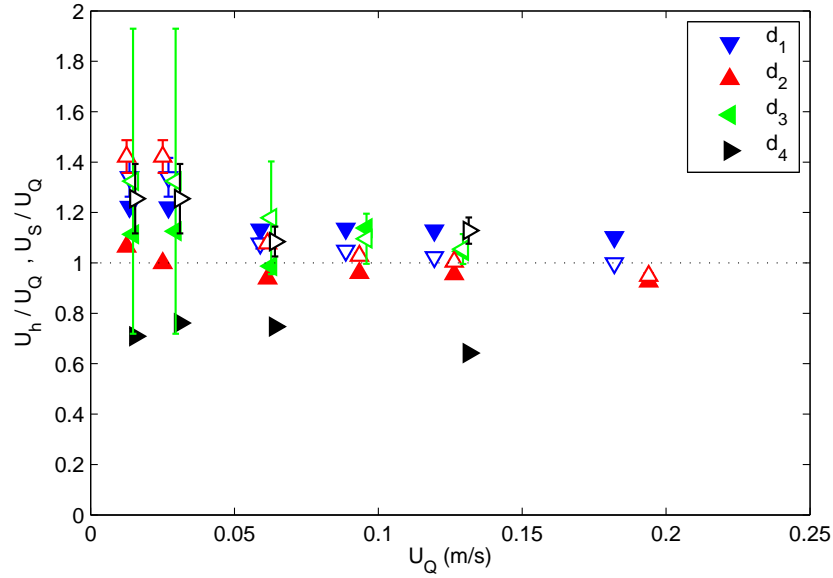


Figure 4.4: Ratios of depth averaged, U_h (solid symbols), and estimated, U_S (open symbols), velocities over the mean porous velocity, U_Q . Error bars represent uncertainty over the measured slopes used to calculate U_S .

For emergent rigid cylinders, given the observed generation of waves at some of the flow rates studied (see Section 3.3.3), C_d is calculated as a time average from the time dependent equations (Eq. 3.11, 3.12, 3.13). The calculated coefficients are shown in Figure 4.6 as a function of Re_d .

Using the measured C_d values, we investigate how the velocity estimates using the free surface slope perform with the actual, measured drag coefficients as opposed to assuming a constant C_d . Figure 4.7 presents both approaches. Since the actual C_d values are larger than the estimated $C_d = 1.13$ the new estimates appear to underestimate the mean, porous velocity, U_Q , by as much as 20%.

The simple, yet powerful drag plate approach allows us to find drag coefficients without requiring further assumptions or simplifications. An alternative common approach to estimating the drag on fully emergent, rigid elements, leverages the assumption of steady state, fully developed flow, neglecting bed and free surface stresses (Tanino and Nepf, 2008a,b). For a flow satisfying all of the above condi-

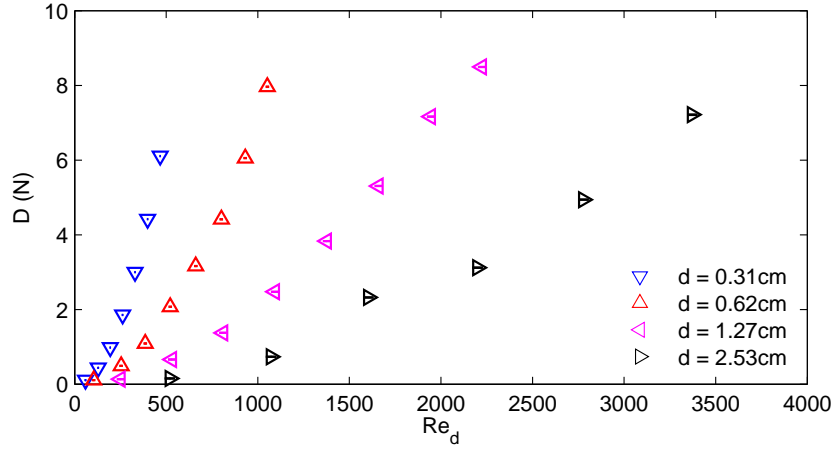


Figure 4.5: Measured drag as a function of Re_d for each diameter tested. Vertical bars show the 95% CI.

tions, a drag coefficient can be found by solving the simplified governing equation, Eq. 4.4, where n is the number of elements per square meter, ϕ is the solid volume fraction of the array, and $\partial h/\partial x$ is the free surface slope:

$$\frac{C_d U_h^2}{2} n d = -(1 - \phi) g \frac{\partial h}{\partial x} \quad (4.4)$$

To compare the estimated values from Eq. 4.4 against the measured C_d values, ultrasonic wave gages (S18U Series, Banner Engineering Corp.) were placed along the flume, sampling at $50Hz$ for $5min$, to measure the free surface slope to account for lateral variations. An array of seven wave gages was used to measure the surface height at seven transverse locations (y -axis), at several longitudinal locations (x -axis). Based on the results (Figure 4.8), two conclusions can be made: 1) relatively large variations are found laterally due to the presence or absence of cylinder wakes, and 2) the x -location of the wave gages can also introduce errors in the calculations, since placing the sensors up or downstream, or even too close to the array edges will lead to an underestimate of the slopes, since the assumptions of one-dimensional flow are violated. Considering the lateral variations, the ratios of the measured

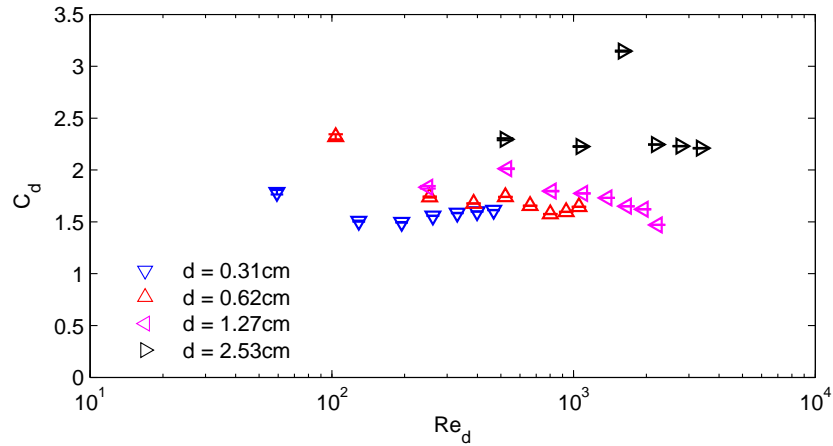


Figure 4.6: Drag coefficient as calculated from the drag plate measurements (Equation 4.3). Vertical bars show the 95% CI.

and estimated drag coefficients are calculated and presented in Figure 4.9. It is noticed a clear trend for all diameters, where C_d values estimated from the free surface slope over-predict the actual, measured drag at lower Re_d , but as Re_d increases, they underestimate C_d for as much as 20%. The large uncertainties in the slopes due to lateral variability confirm the need for a device capable of measuring the drag without further assumptions of the flow conditions, and the successful performance of the drag plate assures the ability to study increasingly complex flows.

We intend to use the data from arrays of emergent, rigid cylinders to predict values of C_d in more complex flows (submerged arrays, and flexible elements). Values of C_d for all experiments from Table 4.1 are presented in Figure 4.10. To investigate the relevance of three characteristic length scales of the flow, C_d is plotted against three different Reynolds numbers, using d , a^{-1} , and s_n as length scales, but no clear trend is seen (Figure 4.10). To account for array properties other than the cylinder diameter, we propose the use of a different non-dimensional parameter, $C_d a d$. By using this term, we notice a seemingly asymptotic tendency for larger values of Re_d as a consistent, increasing function of ϕ (Figure 4.11). The

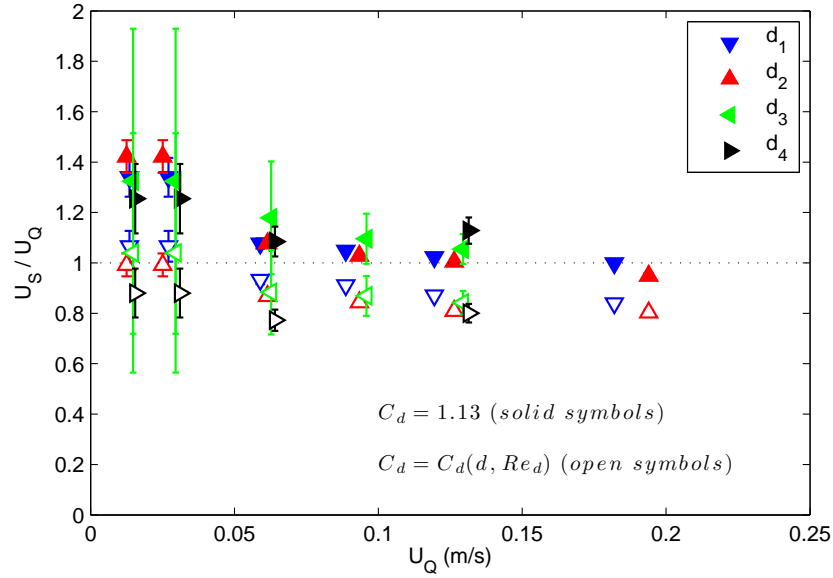


Figure 4.7: Comparison of ratios of estimated longitudinal velocities, U_S , over the mean porous velocity, U_Q , by using a constant $C_d = 1.13$ (solid symbols), and using the measured drag coefficients from Figure 4.6 (open symbols).

similarity in the values for the d_1 , $a = 4m^{-1}$, and d_2 , $a = 2m^{-1}$ cases is apparent, both with the same $\phi = 0.010$. By fitting a horizontal line to each ϕ -curve, we calculate expected asymptotic values for $C_d a d$ in terms of ϕ , finding a linear relationship, $C_d a d = 2.1\phi$, for $\phi < 0.04$. A quadratic fit is also suggested for the whole range of ϕ studied (Figure 4.11).

Ergun (1952) proposed a dimensionless expression for pressure drop in flow through packed columns, using the mean drag per unit length of cylinder, $\langle \overline{f_D} \rangle = \rho(1 - \phi)f_1/n$, where n = number of cylinders per unit area.

$$\frac{\langle \overline{f_D} \rangle}{\mu U_Q} = \alpha_0 + \alpha_1 Re_d \quad (4.5)$$

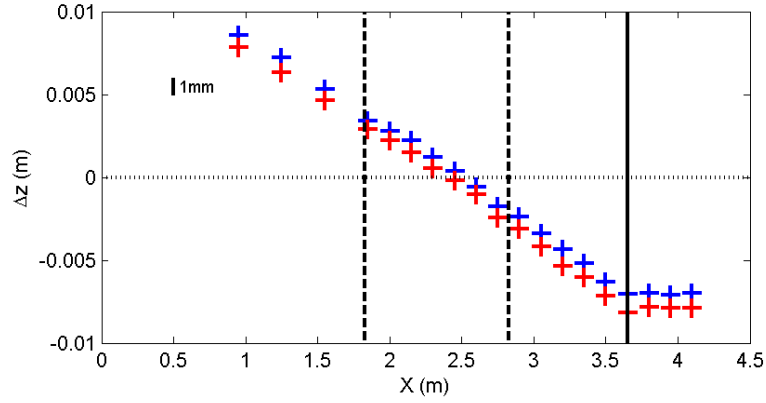


Figure 4.8: Measured surface displacements with an array of 7 ultrasonic wave gages spanning the width of the flume at 19 x-locations, for the $d=0.64\text{cm}$ cylinders array with $U_Q=14.37\text{cm/s}$. Dashed line marks the edges of the drag plate. Solid line marks the end of the cylinders array. For simplicity only maximum and minimum values at each X-location are presented

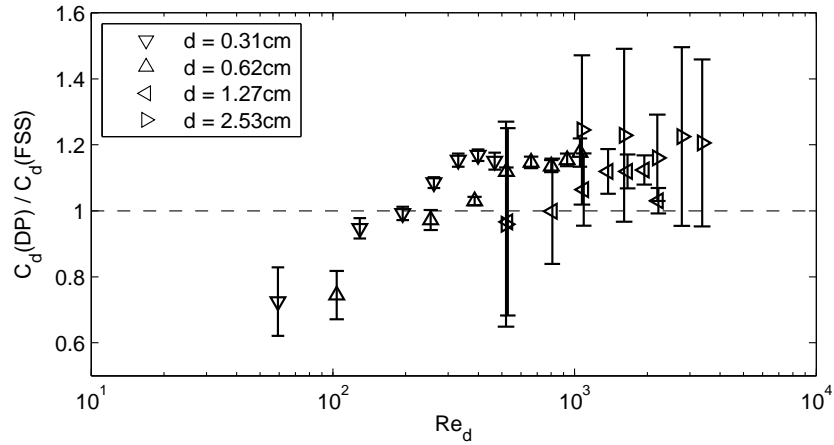


Figure 4.9: Ratios from C_d calculated from the direct drag plate measurements ($C_d(DP)$), and the estimated via momentum balance using the free surface slope ($C_d(FSS)$). Error bars correspond to variations in $C_d(FSS)$ at the maximum and minimum values of the slope obtained from the lateral measurements.

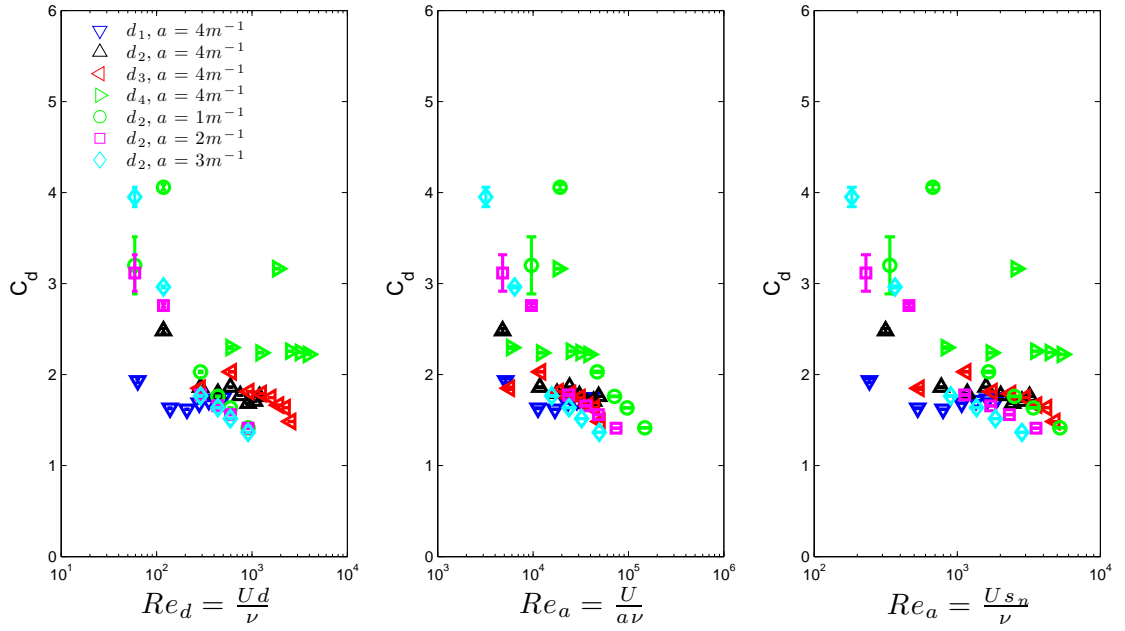


Figure 4.10: C_d values for emergent, rigid cylinders as a function of Re_d , Re_a , and Re_s .

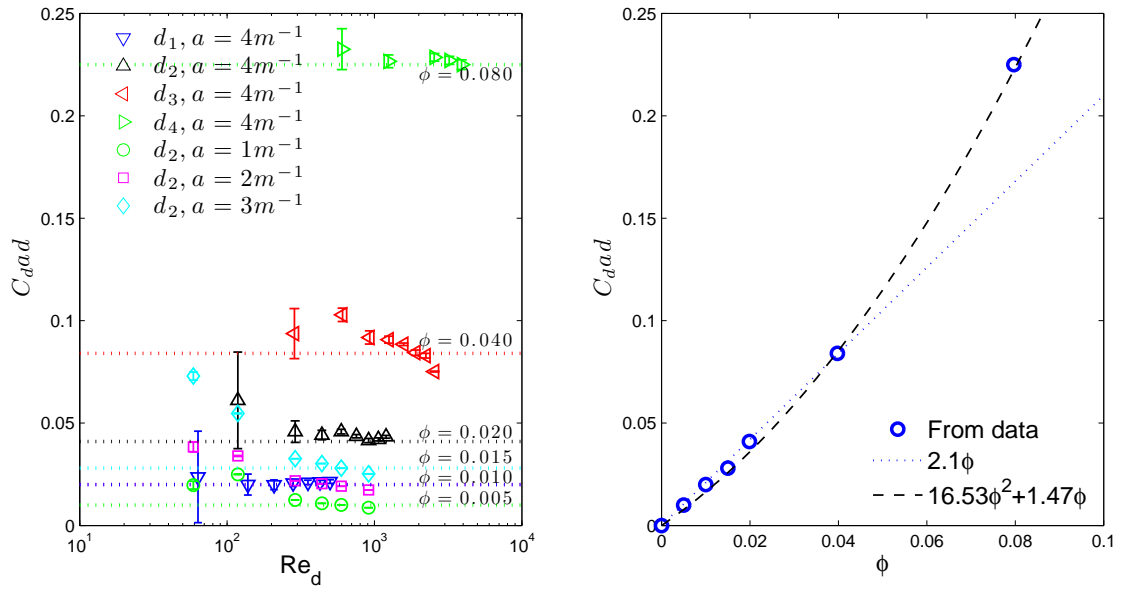


Figure 4.11: Dimensionless parameter C_{dad} as a function of Re_d and ϕ .

Here μ is the dynamic viscosity of the fluid and the ratio α_1/α_0 can be interpreted as a ratio of the inertial to viscous contributions of drag (Koch and Ladd, 1997). The drag coefficient $C_d = 2 \langle \overline{f_D} \rangle / (\rho d U_Q^2)$ can be expressed in terms of Eq. 4.5 as:

$$C_d = 2 \left(\frac{\alpha_0}{Re_d} + \alpha_1 \right) \quad (4.6)$$

Numerical simulations by Koch and Ladd (1997) confirm the validity of Ergun’s equation for flow through packed rigid cylinders. They found a monotonic decrease of α_1/α_0 with increasing ϕ , but there is no mention of how to estimate the values of α_1 and α_0 . Results from laboratory experiments by Tanino and Nepf (2008a) with rigid cylinders with $d = 0.64\text{cm}$, suggest α_1 to be a linear function of ϕ , while α_0 reaches a constant value for $\phi > 0.15$. However, as Tanino and Nepf (2008a) state, the values of such coefficients are very sensitive to the uncertainties from the data itself and the linear regressions.

Using Eq. 4.5, a linear relationship is found from our data. We perform a linear regression to find the α coefficients (Table 4.3) and respective C_d curves for each ϕ (Figure 4.12). Values of ϕ in our tests are lower than those used by Tanino and Nepf (2008a), but the same tendency towards larger C_d values as ϕ increases is noticed.

Table 4.3: Estimated values of α_1 and α_0 from Ergun’s equation.

d (cm)	ϕ	α_0	α_1
0.31	0.010	50	0.75
0.62	0.020	60	0.84
1.27	0.040	140	0.90
2.53	0.080	200	1.15
0.62	0.005	70	0.60
0.62	0.010	55	0.70
0.62	0.015	60	0.75

To compare the latter approach against our estimates from Figure 4.11, we

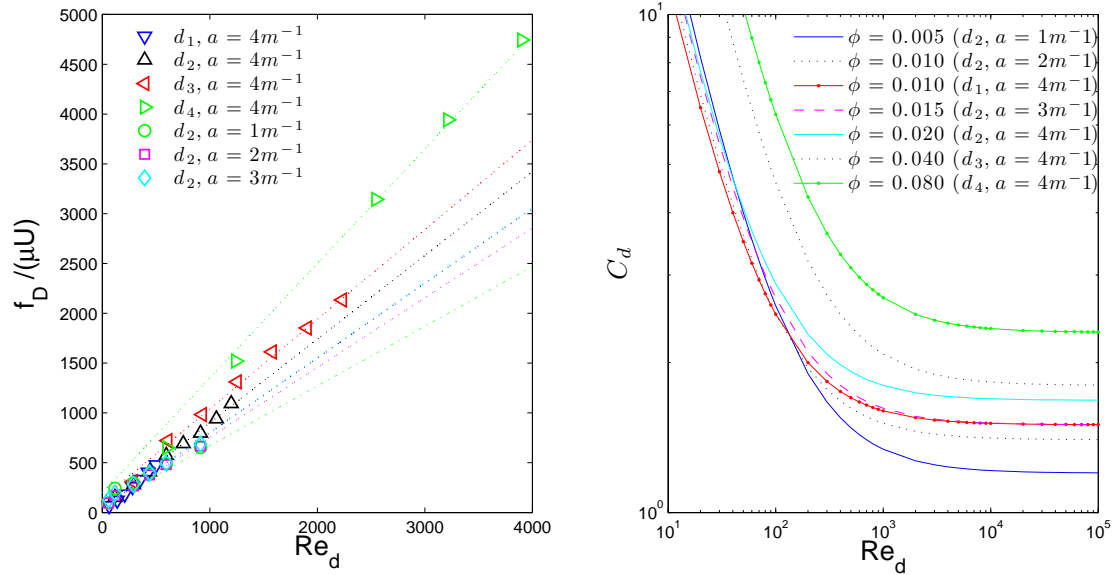


Figure 4.12: Dimensionless drag per unit length of cylinder (left) and estimated drag coefficient curves from the linear fitting to Ergun's equation (right).

plot the fitted C_d curves from Ergun's equation as $C_d ad$, and compare it against our data (Figure 4.13), noticing a monotonic increase of $C_d ad$ with ϕ . The match between the data and the estimated values suggests that using Eq. 4.6, with the α values from Table 4.3, we can now predict the values of C_d for arrays of emergent cylinders as a function of ϕ . In addition, we can also find the asymptotic values for each ϕ , and find a simpler relationship between $C_d ad$ and ϕ , independent of Re_d , for $Re_d > 1000$, as shown in Figure 4.14, similar to the one found in our first estimate (Figure 4.11).

In later sections, we test the consistency of the $C_d = f(Re_d)$, and $C_d ad = f(\phi)$ relationships found for emergent cylinders, against measurements in arrays of submerged cylinders, and arrays of flexible vegetation.

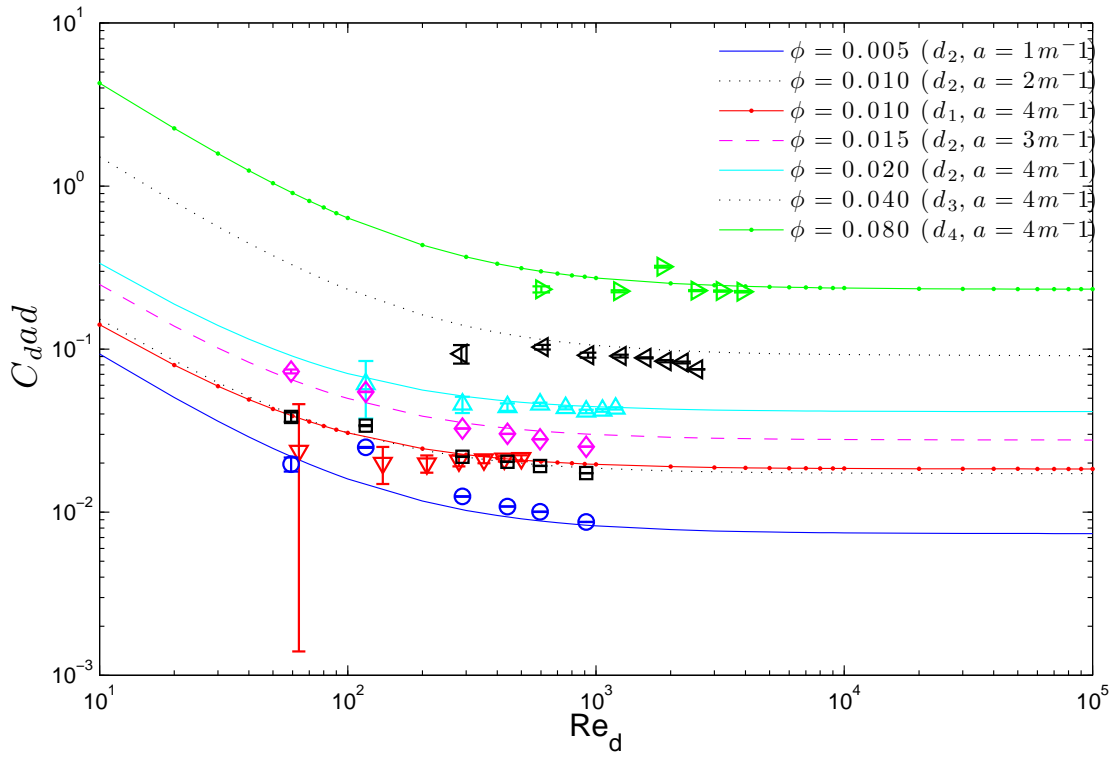


Figure 4.13: Dimensionless parameter $C_d a d$ as a function of Re_d and ϕ .

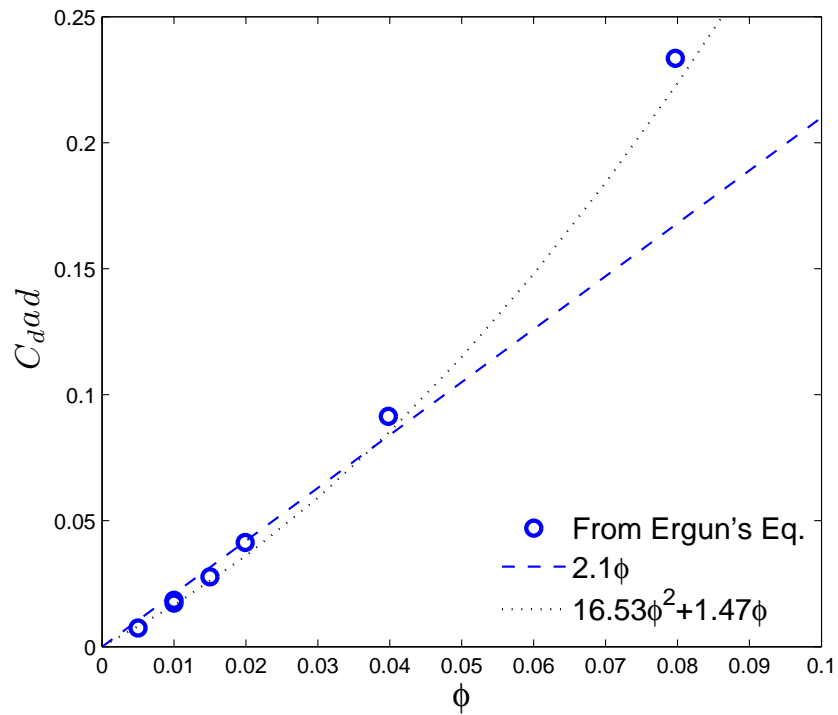


Figure 4.14: Dimensionless parameter $C_d a d$ as a function of ϕ for $Re_d > 10^3$.

4.3.2 Analysis of momentum and tke budgets

Normalized profiles of longitudinal mean velocity U/U_Q , turbulent kinetic energy $\langle \sqrt{k} \rangle / U_Q$, and Reynolds stresses $\langle \overline{u'w'} \rangle / U_Q^2$, are shown in Figure 4.15 (from 2-D PIV data, $k = \frac{1}{2} (2 \langle \overline{u'} \rangle + \langle \overline{w'} \rangle)$). We compare the velocity profiles against estimates from the free surface slope (Eq. 4.2). The data profiles only represent one transverse location, and suggest the need for further spatial averaging.

Estimates of k are obtained from a simplified turbulent kinetic energy equation, which in the absence of vertical gradients yields a balance between wake production, P_w , defined as the work done by the flow against form drag, and the viscous dissipation of turbulent kinetic energy, ϵ , accounting for the conversion of mechanical energy into internal energy (heat), as stated in Eq. 4.7 to 4.9:

$$P_w = \epsilon \quad (4.7)$$

$$\epsilon \sim \frac{k^{3/2}}{d} \quad (4.8)$$

$$P_w \sim \left(\frac{1}{1-\phi} \right) \frac{1}{2} C_{da} U^2 U \quad (4.9)$$

The dissipation scaling from Tennekes and Lumley (1972) is used, with d as the characteristic length scale (Tanino and Nepf, 2008b). The production of tke in the cylinder wakes is calculated as the work input by canopy drag. Solving the above set of equations, a relationship was found by Tanino and Nepf (2008b), for rigid, emergent cylinders:

$$\frac{\langle \sqrt{k} \rangle}{U_Q} = \gamma \left(\frac{1}{1-\phi} 0.5 C_{da} d \right)^{1/3} \quad (4.10)$$

Their experiments with random arrays of cylinders, $d = 0.64\text{cm}$, $\phi = \{0.010-0.35\}$

indicated a value $\gamma = 1.1$. Using k , U_Q , and C_{dad} data from our experiments, we find a better agreement for $\gamma = 0.6$ (see Figure 4.15, where estimates from both γ values are given, with the $\gamma = 1.1$ clearly overpredicting tke). Only one lateral measurement was taken, so no spatial averaging from PIV data was possible. However, we use ADV data, taken at 4 lateral y -locations, at a single elevation z , for several flow rates, to further investigate the value of γ . Figure 4.16 shows the mean values of γ , averaged over the 4 lateral locations at each flow rate. The mean of all experiments yields a value of $\gamma = 0.99$, but the large variations observed between lateral locations suggest that further studies with a better averaging scheme should be performed before claiming a unique, if any, value of γ .

Reynolds stresses $\langle \overline{u'w'} \rangle$, also plotted in Figure 4.15, are negligible, confirming our original assumption for the simplified momentum equation. An apparent increase of Reynolds stresses for the thickest cylinders $d_3 = 1.27cm$ and $d_4 = 2.53cm$, can be attributed to fewer shedding periods being sampled in the $t_s = 410s$ long PIV records. A non-dimensional time $t^* = t_s \cdot f$, where f is the shedding frequency of a single cylinder, reveals that for the thinnest cylinders, $d_1 = 0.31cm$, we sampled between $t^* = \{380 - 5000\}$, whereas for the thickest cylinders, $d_4 = 2.53cm$, we have $t^* = \{53 - 218\}$.

We use records from ADV measurements at mid-depth, at four lateral locations, to calculate the frequency spectra of the lateral velocity for all four diameters. Each $200Hz$ record is resampled (averaged down) at $50Hz$, ensemble averaged over 8 sub-windows, and horizontally averaged (Figure 4.17). We notice: a) a clear peak in each curve around the expected shedding frequency for a single cylinder, $f = 0.21U_Q/d$, signaling the scale at which tke is being generated, and b) the inertial range, with a $-5/3$ slope, indicating the presence of turbulence at frequencies higher than the shedding frequency, confirming the injection of tke by stem wakes.

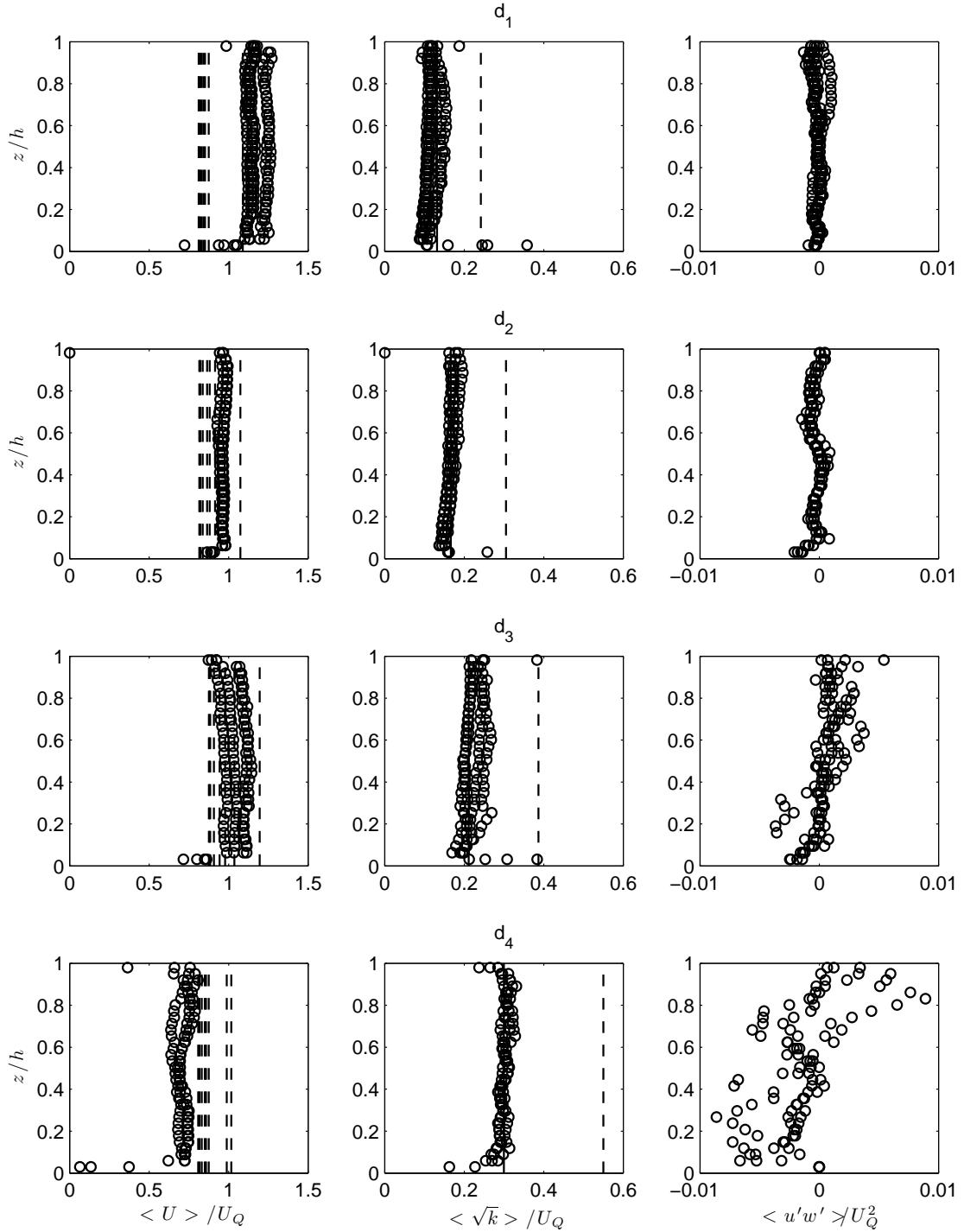


Figure 4.15: Dimensionless profiles of U/U_Q , $\langle \sqrt{k} \rangle / U_Q$, and $\langle u'w' \rangle / U_Q^2$ for all flow rates and diameters studied. Dashed lines in left column show the predicted velocity U_S/U_Q . Solid and dashed lines in middle column represent the expected $\langle \sqrt{k} \rangle / U_Q = \gamma (0.5 C_{ad} (1 - \phi)^{-1})^{1/3}$ using $\gamma = 0.6$ and $\gamma = 1.1$ respectively.

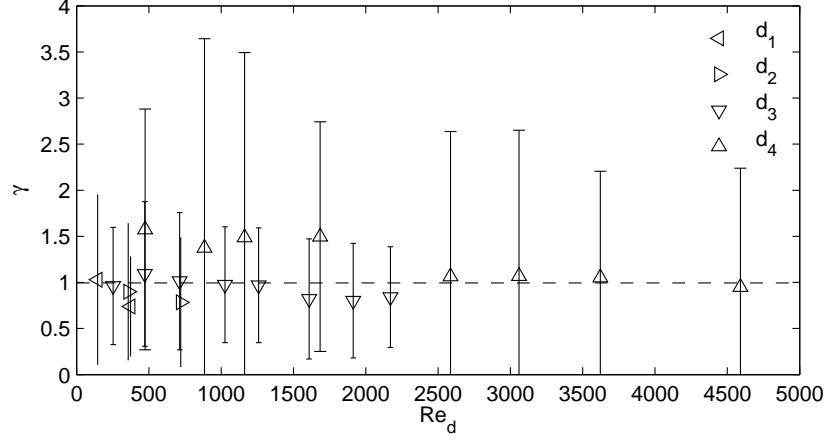


Figure 4.16: Calculation of the coefficient γ , from Eq. 4.10 and point measurements of \sqrt{k}/U_Q at four y -locations at a single elevation z for several flow rates. Dimensionless profiles of U/U_Q , $\langle\sqrt{k}\rangle/U_Q$, and $\langle u'w'\rangle/U_Q^2$ for all flow rates and diameters studied. Dashed line indicates a mean value $\gamma = 0.99$.

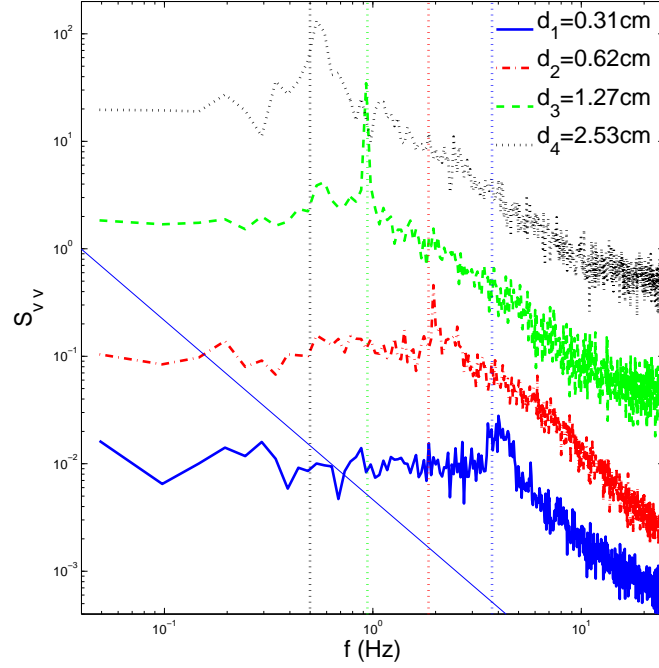


Figure 4.17: Spectra of lateral velocity at mid-depth for all diameters studied, $H/h = 1.0$. Solid line indicates the $-5/3$ inertial range. Vertical dotted lines represent the expected shedding frequency $f = 0.21U_Q/d$. $U_Q = \{5.45, 5.35, 5.47, 5.54\} \text{ cm/s}$.

4.4 Results from arrays of submerged cylinders ($H > h$)

4.4.1 Flow characterization

Analysis of the PIV data provides a good picture of the 2-dimensional, $x-z$ velocity field with high space resolution. However, if one is to study lateral, y , velocities, or requires data at higher time resolutions, then the amount and complexity of experiments, as well as the storage capacity required for the PIV images increases rapidly. In order to study the three-dimensionality of the flow for the $H/h = 1.9$ case ($h = 0.195m$ for submerged cylinders), point measurements were made with the Vectrino ADV on a $y-z$ vertical plane, transverse to the flow direction, creating a grid of 360 points (20 point vertical profiles at 18 lateral locations), with $\Delta y = 3.0cm$ and $\Delta z = 1.5cm$, at the same longitudinal location the PIV data was taken (Figure 4.18). Records of 164s at 200Hz (2^{14} samples) were acquired at each point.

The values of longitudinal mean velocity for each diameter are shown in Figure 4.18. The presence of local velocity maxima at different locations for each diameter demonstrates that secondary circulations exist across the flume width, as a result of the coherent flow structures generated within the canopy.

Figure 4.19 presents side-by-side pseudo-colored images of the three velocity components (u , v , w). The regions of up- and downwards flow are clearly defined, and evidence of secondary circulation becomes more clear. Magnitudes of the downward vertical velocities above the canopy are an order-of-magnitude less than the longitudinal velocities at the same height, but within the canopy the upward vertical velocities are of the same order as the longitudinal component.

Pseudo-colored images of the tke and Reynolds stresses are presented in Figure

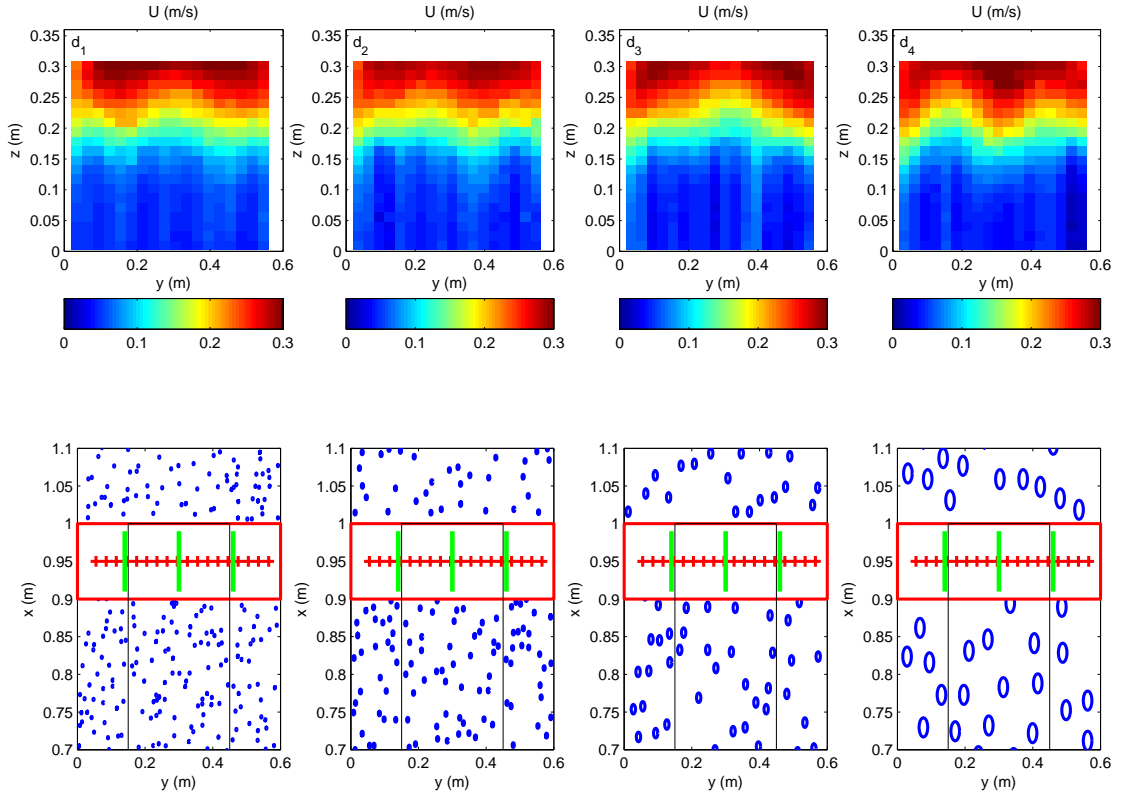


Figure 4.18: ADV measurements of $U(m/s)$ along a $y - z$ plane. The sketch indicates the y -location of the grid points in the region with cylinders removed (downstream edge of the drag plate). The three lines indicate the locations of the $x - z$ planes for PIV data. Cylinders drawn at the right scale (distorted by the $x - y$ dimensions shown). x -coordinates with respect to the upstream edge of the drag plate.

4.20. The peak of both values is expected to occur at the cylinders height, $z = h$, where $h = 0.195m$ for submerged cylinders, but it is clearly being displaced by variations in the vertical velocity, resulting on variations on the location of the peak within a $\pm 5cm$ region from the top of the cylinders.

Studying the time series of velocity and momentum transport (Figure 4.21), fluid ejections ($u' < 0, w' > 0$), and sweeps ($u' > 0, w' < 0$), can be identified for all diameters. A scatter plot analysis of u', w' for all diameters (Figure 4.22) confirms that sweeps dominate ejections within the canopy (Ghisalberti and Nepf, 2006; Ghisalberti, 2010).

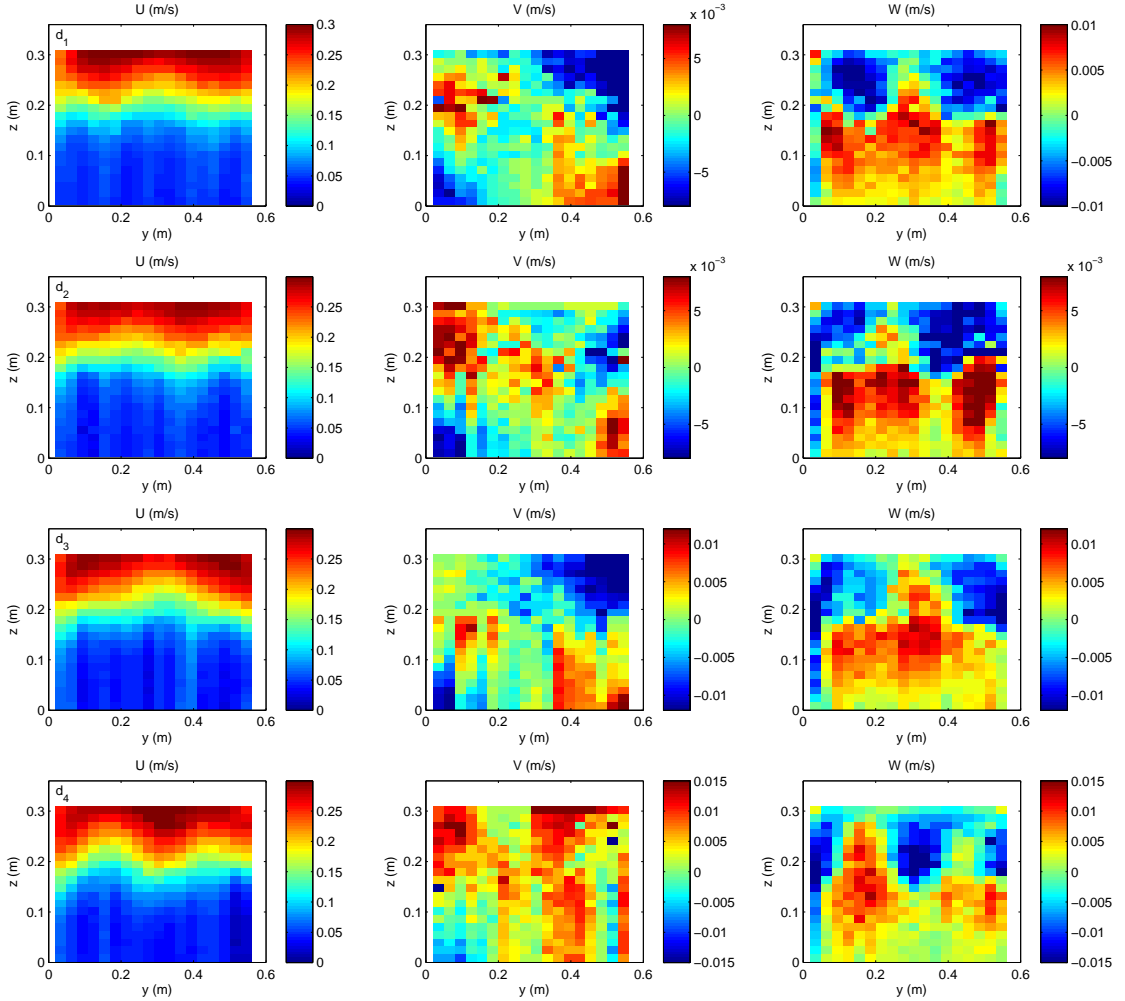


Figure 4.19: ADV measurements of longitudinal, U , lateral, V , and vertical, W (m/s), time averaged velocities along a $y - z$ plane from $d_1 = 0.31cm$ (top row) to $d_4 = 2.53cm$ (bottom row).

Spectra are calculated at three vertical locations: near bottom (wake zone), at the top of the array (exchange zone), and above the array (upper shear layer). Each record was resampled (averaged down) to $50Hz$, ensemble averaged over 8 sub-windows, and horizontally averaged. Energy input at the shear scale, from the canopy-scale eddies generated in the free-shear layer-like region, is apparent, as well as a clear inertial range ($-5/3$ slope) at frequencies higher than the cylinder shedding frequency, $f = 0.21U/d$, an indication of generation of wake kinetic energy (Figure 4.23).

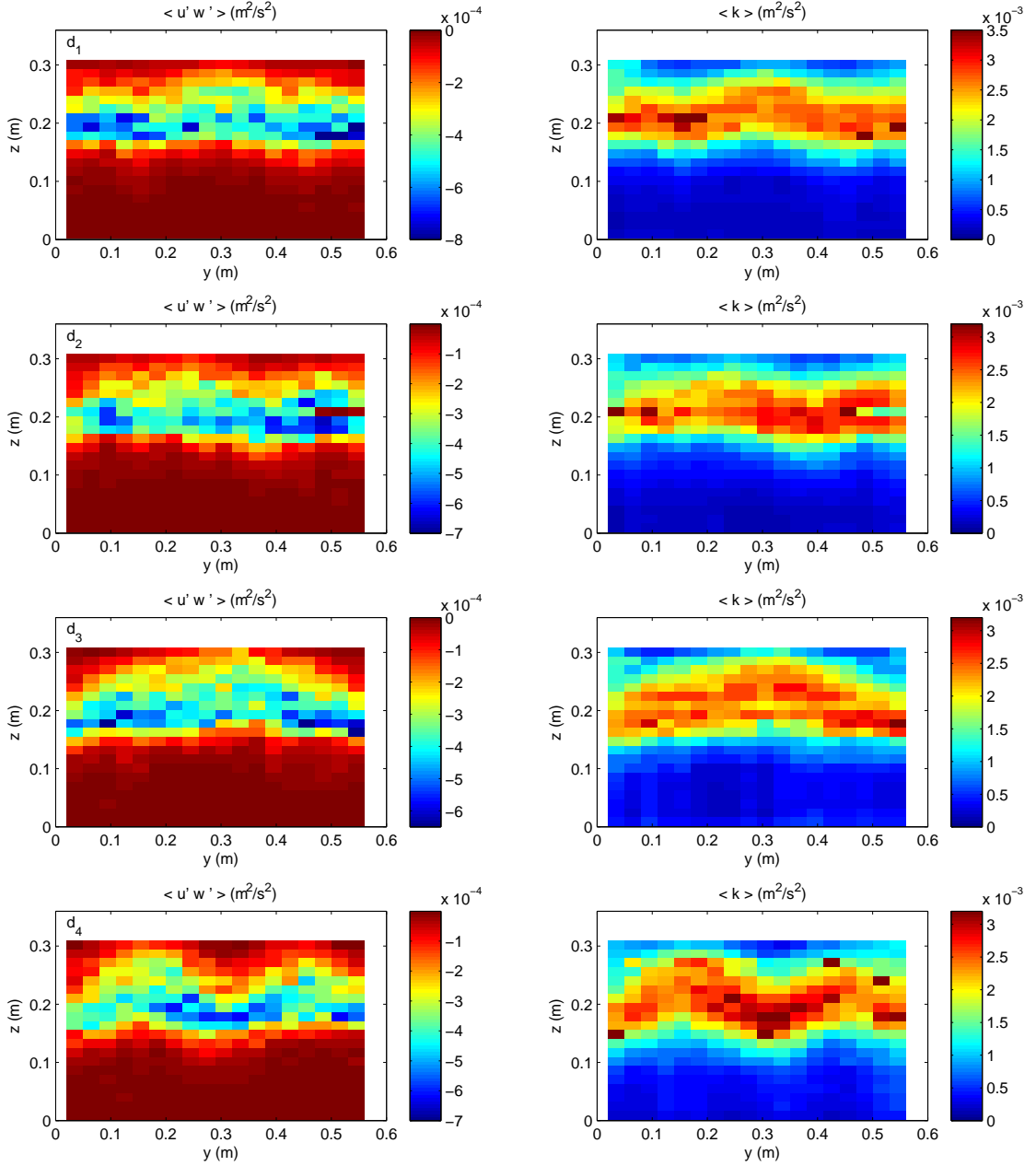


Figure 4.20: ADV measurements of $\langle u'w' \rangle$ and k (m^2/s^2) along a $y-z$ plane from d_1 (top row) to d_4 (bottom row).

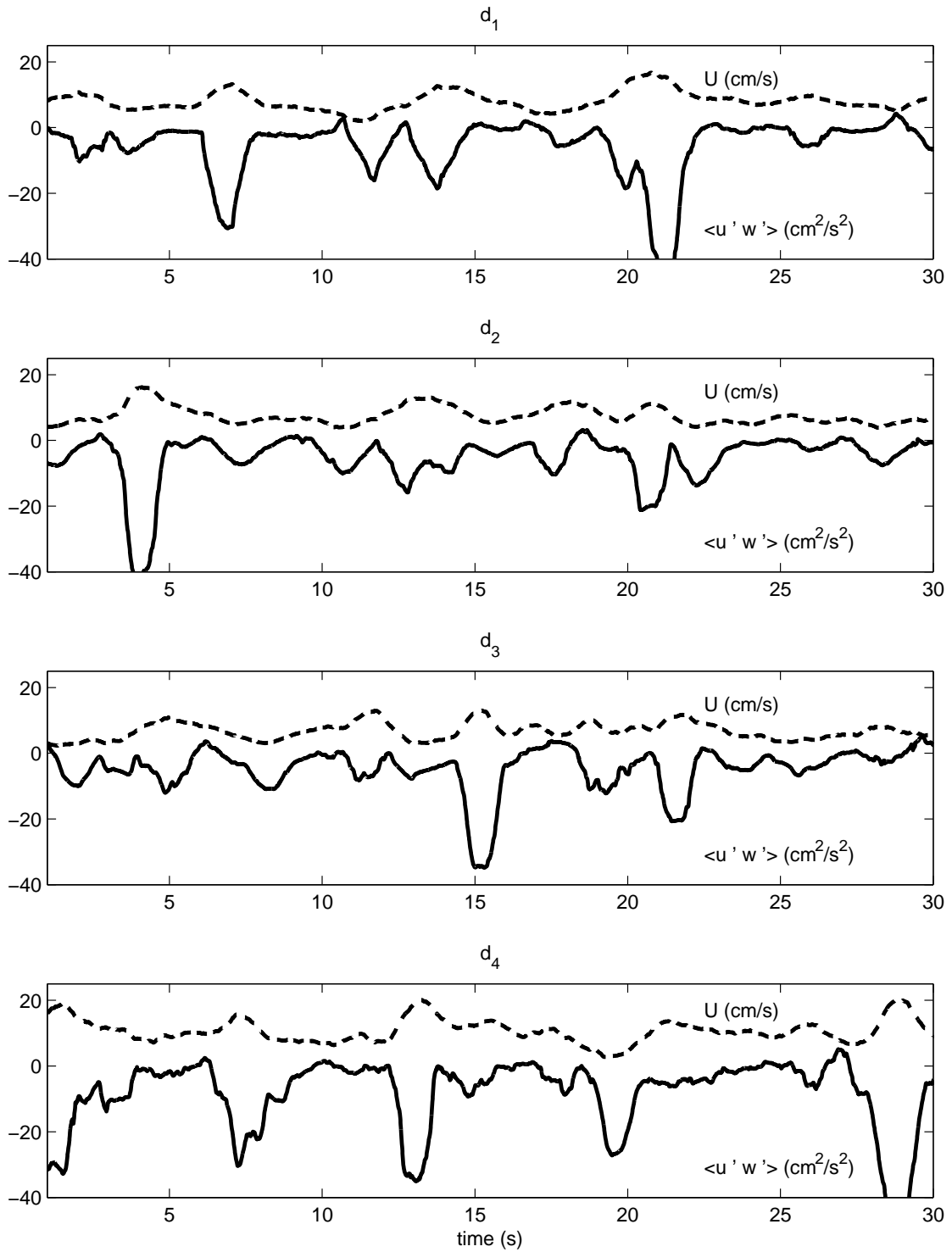


Figure 4.21: Time series of U (cm/s) (dashed line) and $\langle u'w' \rangle$ (cm^2/s^2) (solid line) at $z = 0.17\text{m}$. Fluid ejections ($u' < 0, w' > 0$), and sweeps ($u' > 0, w' < 0$), can be identified for all diameters. Time series smoothed by a 0.5s moving average.

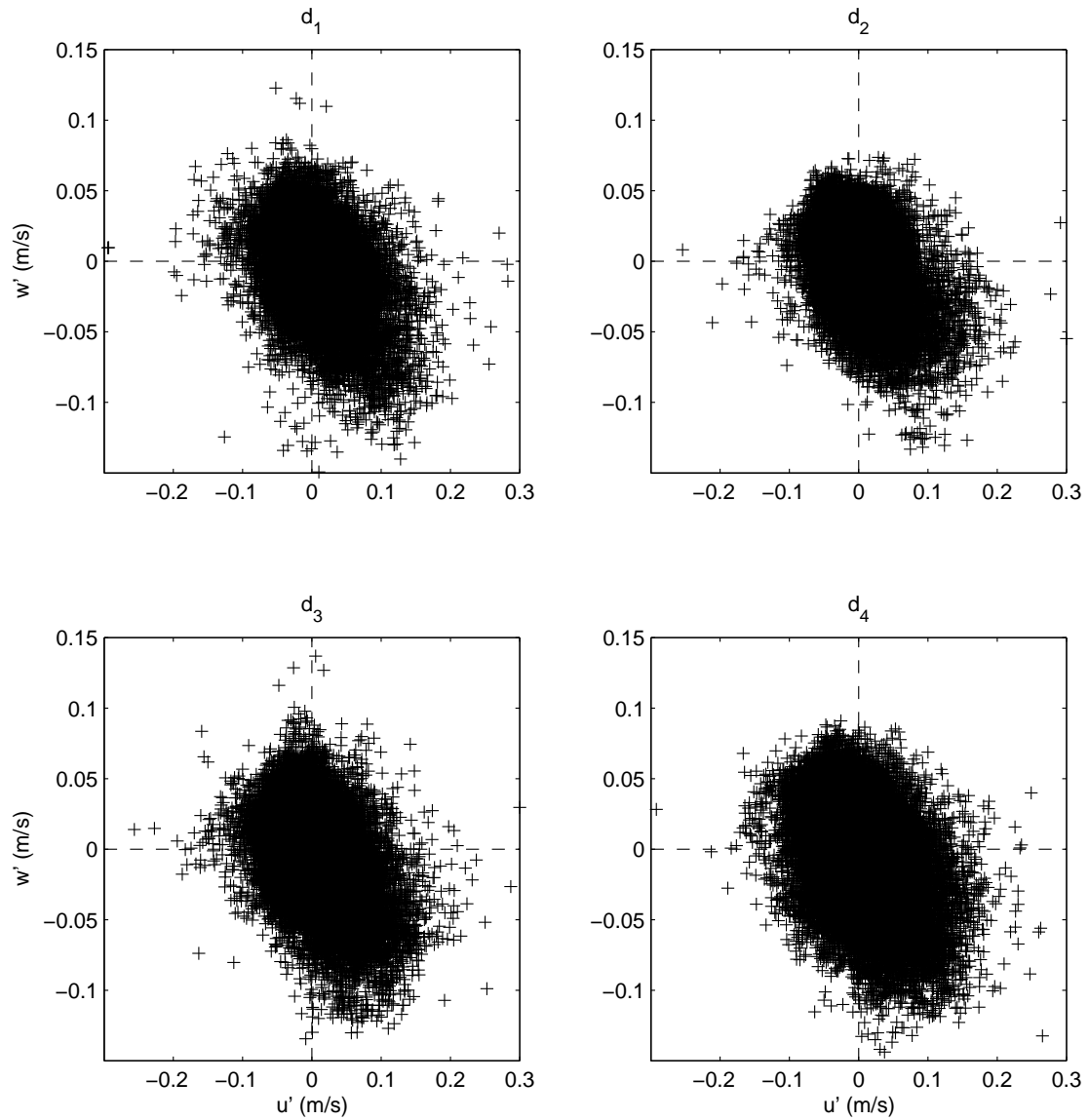


Figure 4.22: Scatter plots of u' , w' for all diameters, at $z = 0.17m$. Notice the tendency to stronger sweeps ($u' > 0, w' < 0$) than ejections ($u' < 0, w' > 0$), as seen also in Figure 4.21.

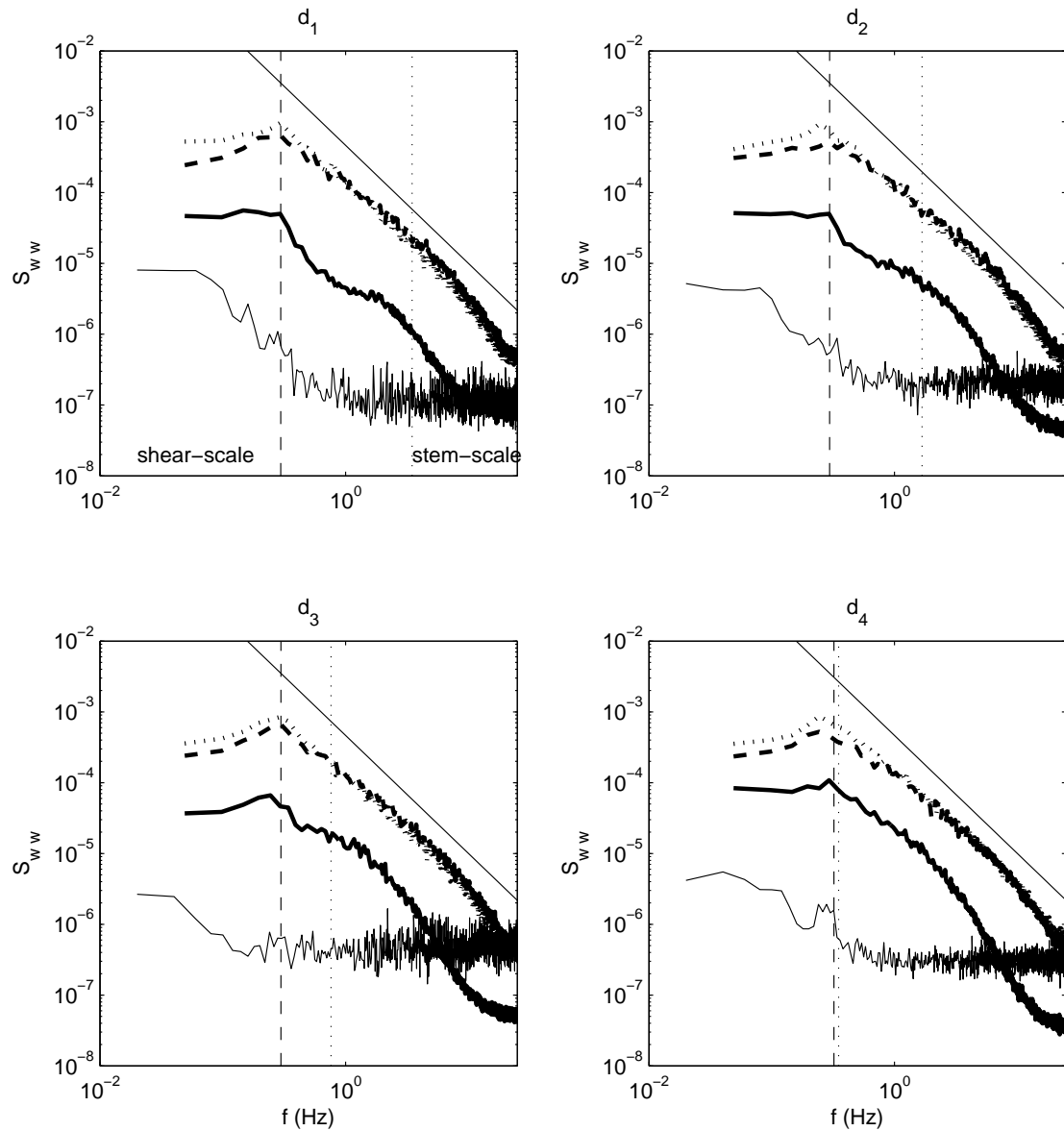


Figure 4.23: Spectra of vertical velocity at the upper shear layer (dashed line), top of the array (dotted line), and wake zone (solid line), for all diameters studied, $H/h = 1.9$. Solid straight line indicates the $-5/3$ inertial range. Vertical lines represent the observed shear frequency (dashed line), and shedding frequency $0.21U/d$ (dotted line). Thin solid line represents the frequency spectra from the measured drag.

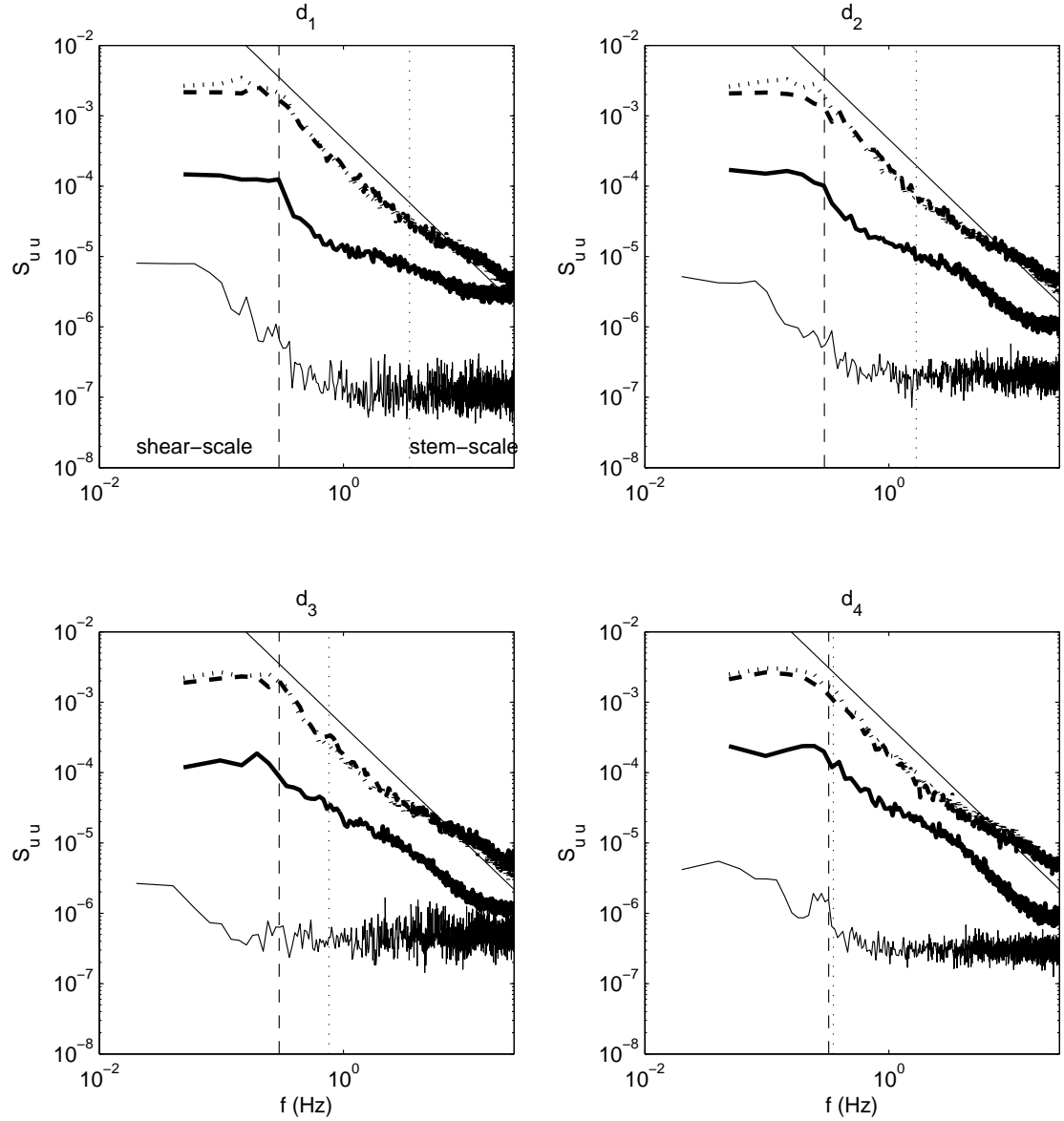


Figure 4.24: Spectra of longitudinal velocity at the upper shear layer (dashed line), top of the array (dotted line), and wake zone (solid line), for all diameters studied, $H/h = 1.9$. Solid line indicates the $-5/3$ inertial range. Vertical lines represent the shear frequency $0.4U_{hc}/h$ (dashed line), and shedding frequency $0.2U/d$ (dotted line). Thin solid line represents the frequency spectra from the measured drag.

4.4.2 Analysis of drag and velocities

Two submergence ratios were studied: $H/h = 1.9$ and 1.25 . Relevant parameters for each test are presented in Tables 4.4 and 4.5. PIV was conducted at three lateral locations, $y = \{0.14, 0.30, 0.56\}m$, to get three 2-D, $x - z$ planes for spatial (lateral) averaging. Sample profiles of U , $\langle k \rangle$, and $\langle \overline{u'w'} \rangle$ for two diameters, at $Q = 0.007m^3/s$, and with $H/h = 1.9$, are shown in Figure 4.25, along with the mean and 95CI values calculated from the uncertainty analysis, using a bootstrap method (Efron and Tibshirani, 1993).

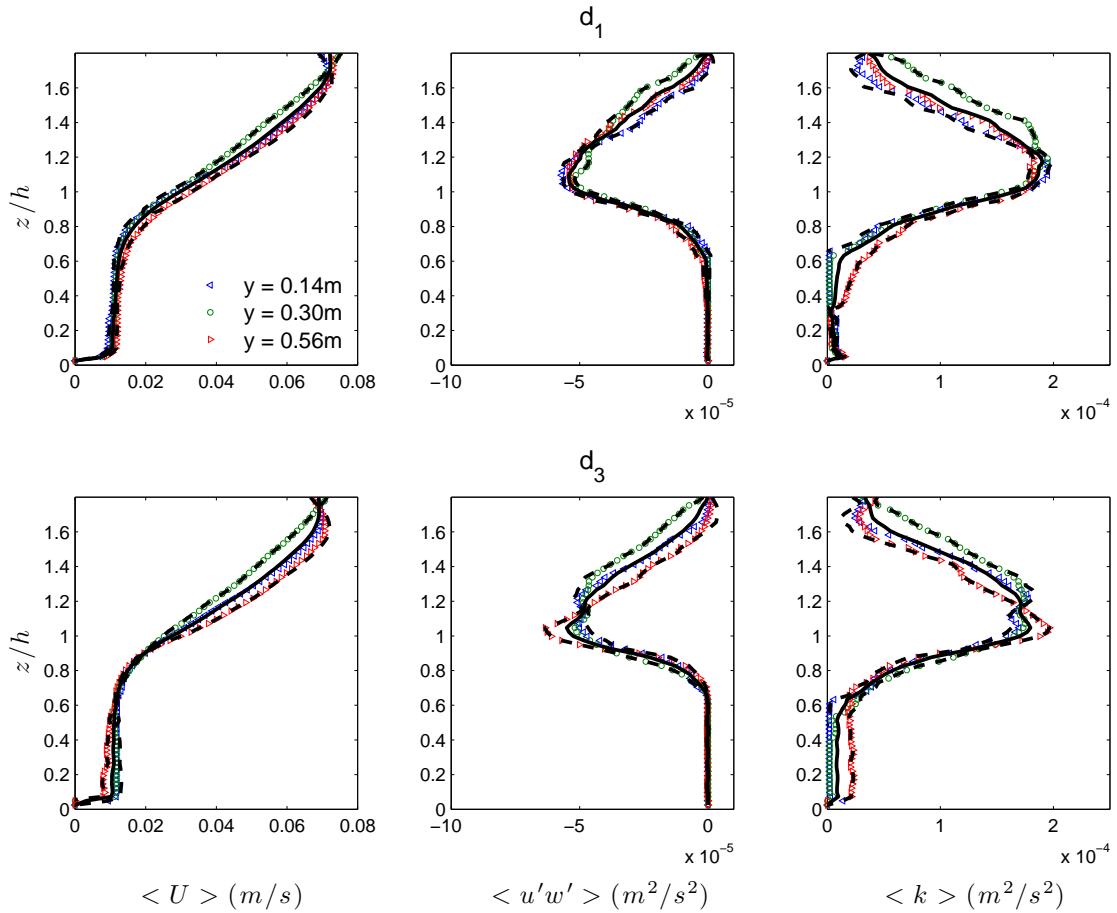


Figure 4.25: Vertical profiles of U , $\langle \overline{u'w'} \rangle$, and $\langle k \rangle$ for a single flow rate, for d_1 (top) and d_3 (bottom), at the three sections studied, $y = \{0.14, 0.30, 0.56\}m$ ($H/h = 1.9$). Elevation z is normalized by the height of the cylinders, h . Solid and dashed lines indicate the mean and 95CI, respectively.

Table 4.4: Relevant parameters for the submerged case PIV experiments, $a = 4.0m^{-1}$, $h = 0.195m$, $H/h = 1.90$.

	d	Q	U_h	Re_d	z_1	t_{ml}	U_1	ΔU	u_*
	(cm)	$(m^3/s) \times 10^{-3}$	(cm/s)	$\frac{U_h d}{\nu}$	(cm)	(cm)	(cm/s)	(cm/s)	(cm/s)
Q_{04}	0.31	7.0	1.48	46	11.6	20.8	1.3	5.9	0.74
Q_{08}	0.31	14.6	3.33	103	10.1	22.3	2.8	12.2	1.69
Q_{16}	0.31	30.3	7.39	228	8.8	23.6	5.7	24.9	3.44
Q_{04}	0.62	7.0	1.26	78	12.5	21.7	1.1	6.0	0.75
Q_{08}	0.62	14.7	2.43	150	12.2	22.2	2.2	12.8	1.69
Q_{16}	0.62	30.5	5.52	340	7.8	26.4	4.2	26.4	3.64
Q_{04}	1.27	7.0	1.38	175	13.0	20.3	1.2	5.7	0.74
Q_{08}	1.27	14.7	2.99	380	11.1	22.6	2.5	12.5	1.48
Q_{04}	2.53	6.9	1.53	385	12.9	20.4	1.3	5.6	0.70
Q_{08}	2.53	14.6	3.12	790	9.7	23.6	2.5	12.2	1.48
Q_{16}	2.53	30.3	6.51	1640	8.8	24.5	5.1	25.6	3.14

Table 4.5: Relevant parameters for the submerged case PIV experiments, $a = 4.0m^{-1}$, $h = 0.195m$, $H/h = 1.25$.

	d	Q	U_h	Re_d	z_1	t_{ml}	U_1	ΔU	u_*
	(cm)	$(m^3/s) \times 10^{-3}$	(cm/s)	$\frac{U_h d}{\nu}$	(cm)	(cm)	(cm/s)	(cm/s)	(cm/s)
Q_{02}	0.31	3.0	1.90	60	11.7	11.7	1.8	2.8	0.51
Q_{04}	0.31	6.6	3.89	120	10.4	13.0	3.7	6.0	1.05
Q_{08}	0.31	14.0	8.32	255	10.0	13.0	7.9	11.5	2.19
Q_{12}	0.31	21.5	12.92	400	10.0	13.0	12.3	16.9	3.21
Q_{02}	0.62	3.0	1.41	88	11.7	13.0	1.3	3.6	0.54
Q_{04}	0.62	6.6	2.95	180	9.5	15.2	2.6	7.6	1.16
Q_{08}	0.62	14.1	6.31	390	10.8	13.0	5.7	14.1	2.40
Q_{12}	0.62	21.7	9.62	595	9.5	14.3	8.9	21.1	3.56
Q_{02}	1.27	3.2	1.68	212	12.1	11.7	1.53	3.5	0.54
Q_{04}	1.27	6.7	3.47	440	9.5	14.7	3.11	7.3	1.15
Q_{08}	1.27	14.0	6.80	860	7.4	16.9	5.5	16.7	2.74
Q_{12}	1.27	21.6	11.67	1475	7.4	16.5	10.2	22.8	3.81
Q_{02}	2.53	3.1	2.07	521	10.8	13.4	1.7	3.8	0.55
Q_{04}	2.53	6.6	4.30	1080	6.1	18.2	3.5	7.8	1.14
Q_{08}	2.53	14.0	9.04	2280	3.9	19.9	7.2	15.2	2.40

Similar measurements are repeated for the four diameters at several flow rates. Data from each section is normalized by a friction velocity scale, $u_* = |\langle \overline{u'w'} \rangle_h|^{1/2}$, where $\langle \overline{u'w'} \rangle_h$ is the value of the Reynolds stress at the top of the canopy, and an average of the 3 lateral sections is calculated to get the spatial, horizontally averaged profiles, as shown in Figure 4.26, where the data collapse onto a single profile for each diameter. Data from all diameters are plotted in Figure 4.27, where the self-similarity is noticed for all cases.

The same analysis is conducted for the nearly emergent case, $H/h = 1.25$, yielding the results shown in Figure 4.28 (for each diameter), and Figure 4.29 (all cases). We notice variations between diameters in the non-dimensional velocity, larger than those for the deeper submergence ratio $H/h = 1.9$, but with no distinctive pattern between them. There is, however, a noticeable relative increase in the non-dimensional profiles of $\langle k \rangle$ in the range $z/h < 1$, for both H/h , as the diameter increases, consistent with the results for rigid cylinders. Using Eq. 4.10, with drag coefficients calculated from the values in Table 4.3, we compare estimated values of $\langle k \rangle$ for the emergent case to the values obtained within the cylinders in both submerged studies, now changing the normalization from $\sqrt{\langle k \rangle}/U_Q$ to $\sqrt{\langle k \rangle}/U(z)$, since a bulk U_Q only works for emergent cylinders. Results, shown in Figure 4.30, using $\gamma = 0.6$ found for emergent cylinders, give a good approximation for the nearly emergent case ($H/h = 1.25$), but is not consistent for the fully submerged ($H/h = 1.9$).

We used the measured, spatially averaged, velocity profiles to investigate drag on submerged arrays. The drag plate was used to directly measure drag for each submergence ratio at several flow rates (Figure 4.31). PIV was not used for all flow rates, only those listed in Tables 4.4 and 4.5. Instead, we use the analysis from cases where PIV was conducted, and couple it with the measured flow rates to get estimates of the velocity within the array. We use a depth averaged velocity,

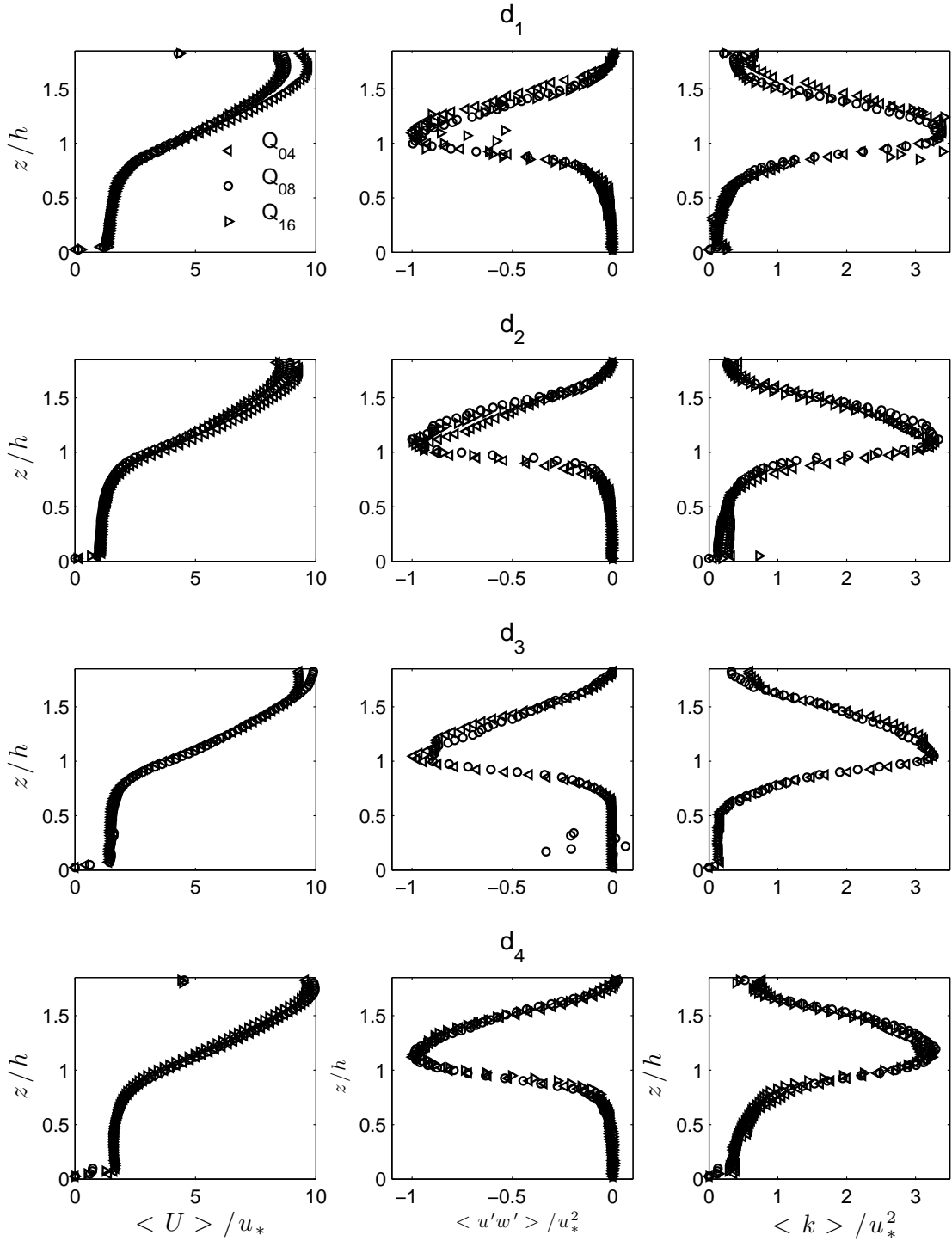


Figure 4.26: Normalized, horizontally averaged vertical profiles U/u_* , $\langle k \rangle / u_*^2$, and $\langle u'w' \rangle / u_*^2$, for all flow rates studied, at each diameter d_i ($H/h = 1.9$).

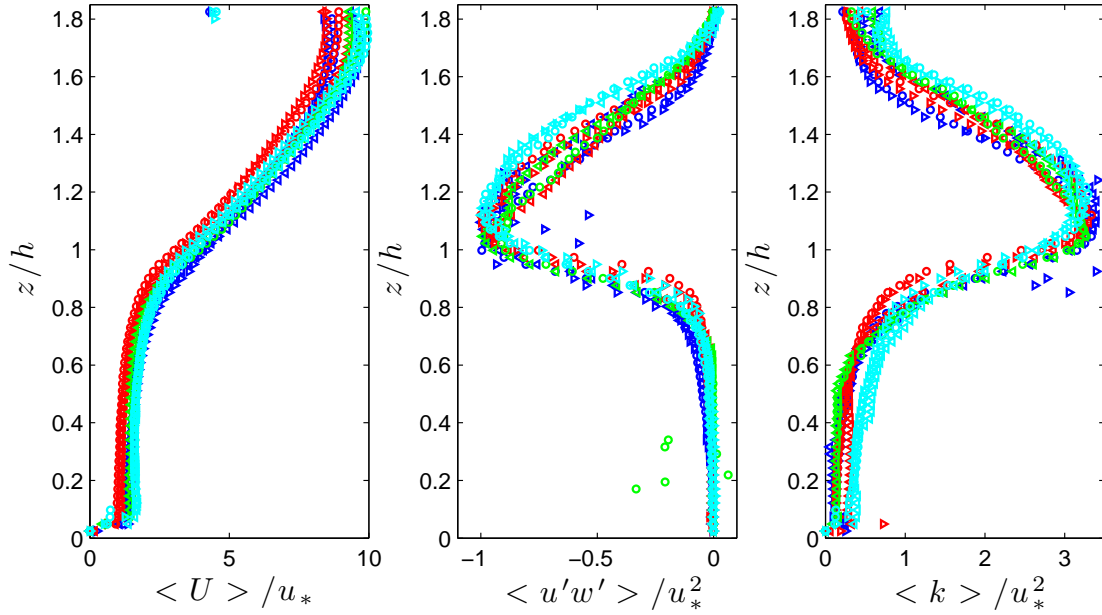


Figure 4.27: Normalized, horizontally averaged vertical profiles U/u_* , $\langle k \rangle / u_*^2$, and $\langle u'w' \rangle / u_*^2$ for all diameters and flow rates studied ($H/h = 1.9$).

U_h , integrated from the bottom to the top of the cylinders ($0 < z/h < 1$). Linear relationships are found between Q and U_h (Figure 4.32), which allows us to use all the drag measurements regardless of availability of velocity data from PIV. A linear relationship is also found between Q and the maximum velocity, U_{max} , for each case (Figure 4.33).

By calculating U_h for all cases studied, a relationship between the measured drag, D , and Reynolds number $Re_d = U_h d / \nu$ can be found similar to the emergent case. Results for D and C_d (Eq. 4.3) are shown in Figure 4.34 for both submergence ratios. We plot the values of C_{dad} in Figure 4.36. These values are lower than the expected C_{dad} values from the emergent cylinders data and Ergun's equation (dotted line Figure 4.36).

We can compare the C_d values calculated from drag measurements to estimated values from the momentum equation. For submerged, rigid arrays, we have:

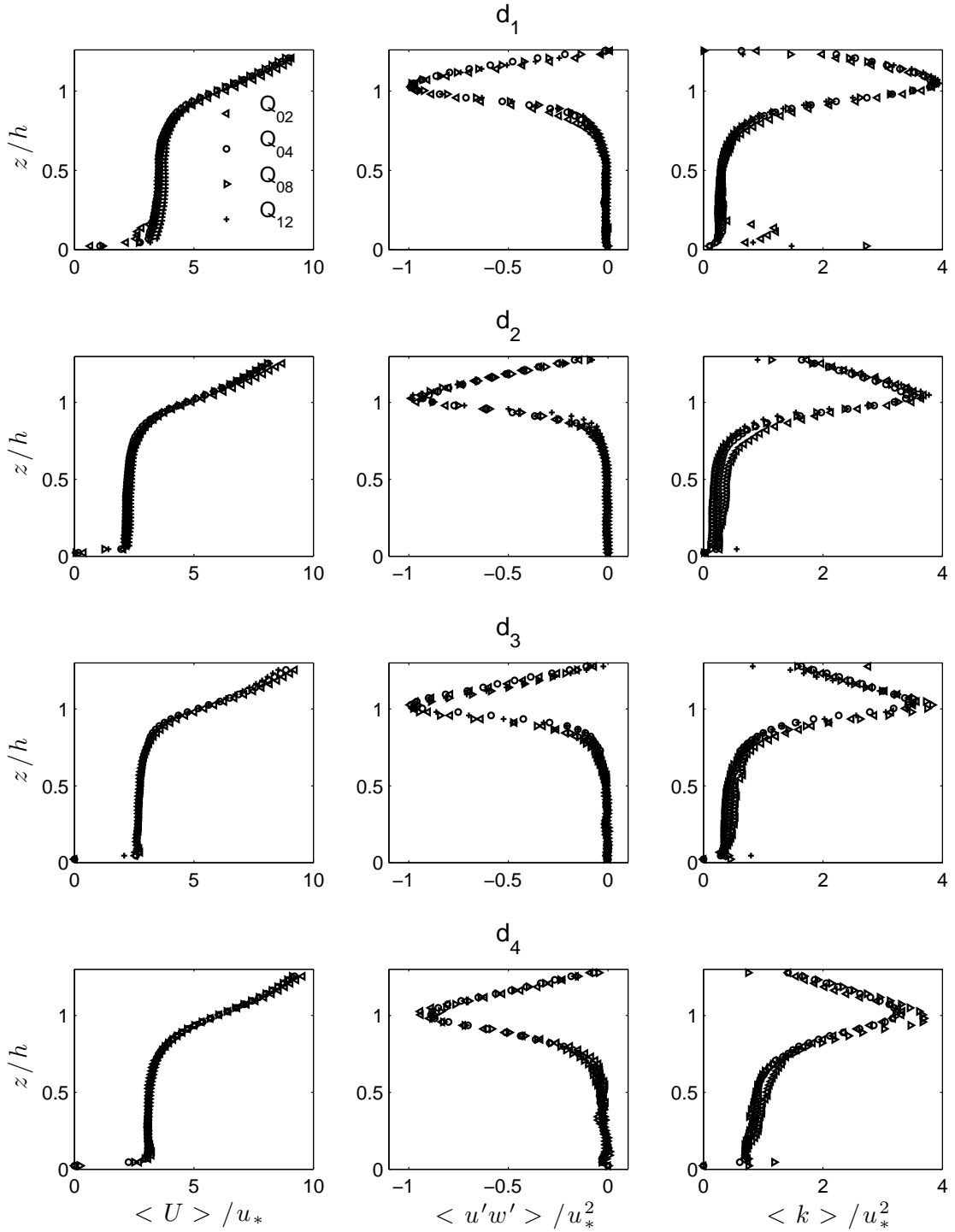


Figure 4.28: Normalized, horizontally averaged vertical profiles U/u_* , $\langle k \rangle / u_*^2$, and $\langle u'w' \rangle / u_*^2$, for all flow rates studied, at each diameter d_i ($H/h = 1.25$).

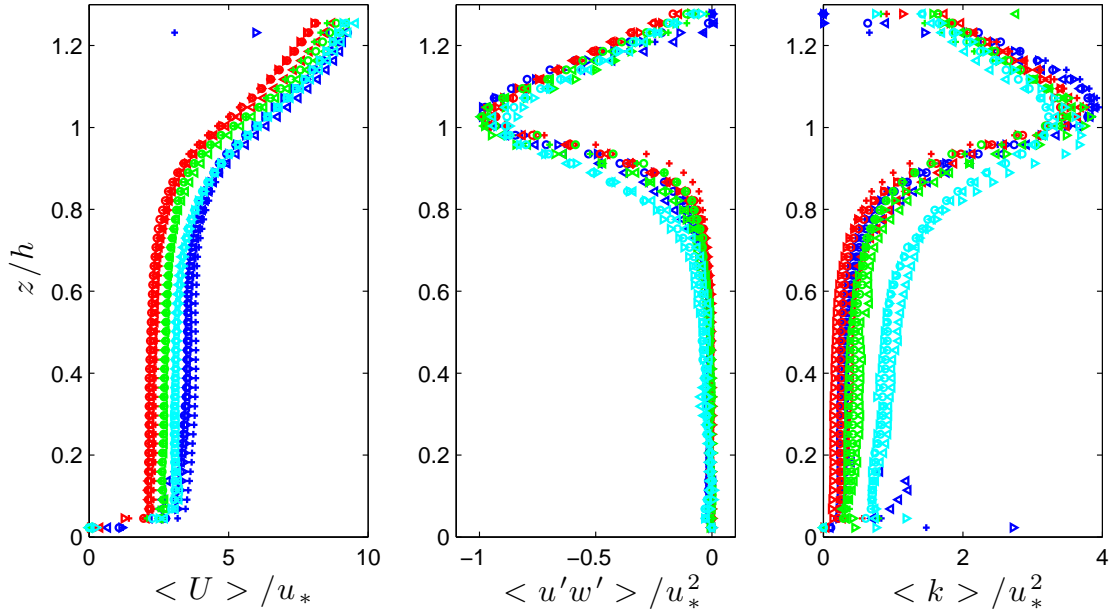


Figure 4.29: Normalized, horizontally averaged vertical profiles U/u_* , $\langle k \rangle / u_*^2$, and $\langle u'w' \rangle / u_*^2$ for all diameters and flow rates studied ($H/h = 1.25$).

$$0 = -gS - \frac{\partial \langle u'w' \rangle}{\partial z} - f_1 \quad (4.11)$$

From Eq. 4.11, a local drag coefficient $C'_d(z)$ (Dunn et al., 1996; Ghisalberti and Nepf, 2004) can be calculated (Eq. 4.12, which can be used to calculate a bulk C_d (Eq. 4.13). Vertical gradients are evaluated with a central difference scheme.

$$C'_d(z) = \frac{-gS - \frac{\partial \langle u'w' \rangle}{\partial z}(z)}{\frac{1}{2}aU(z)^2} \quad (4.12)$$

$$C_d = \frac{1}{h} \int_0^h C'_d dz \quad (4.13)$$

Looking at the vertical profiles of $C'_d(z)/C_d$ (Figure 4.35), a maximum is observed near $z/h = 0.9$, and a clear decrease towards zero at the top of the cylinders, which

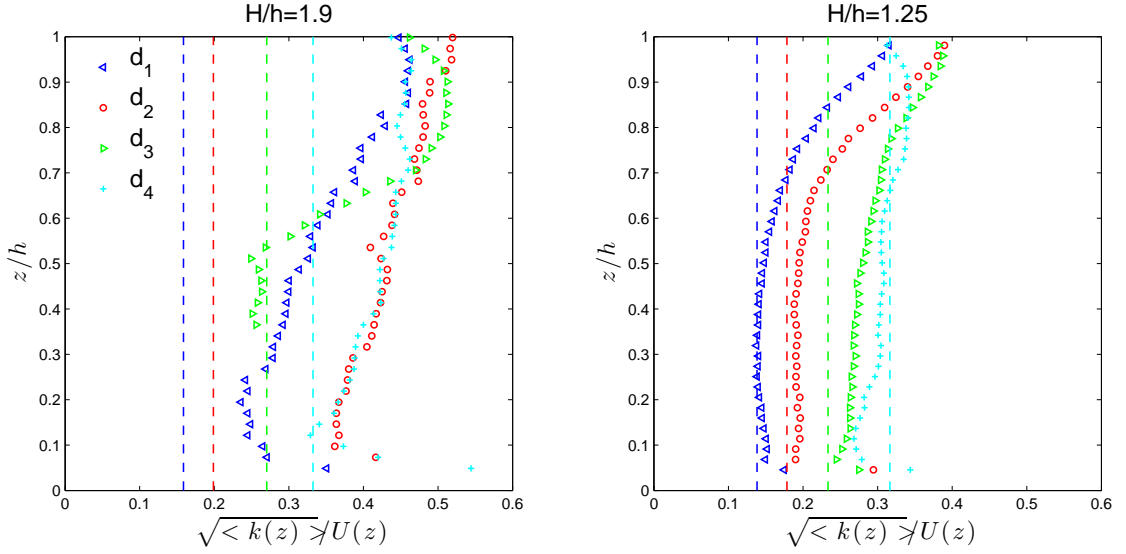


Figure 4.30: Predicted and observed normalized values of $\langle k \rangle$. For clarity only data up to $z/h = 1$ are shown.

has previously been described as representative of the free-end effects on cylinder drag, where strong longitudinal vortices are generated near the tip, increasing wake pressure and reducing drag (Ghisalberti and Nepf, 2004). We compare side-by-side the estimated values of the bulk C_d (Eq. 4.13) and the measured C_d values (Eq. 4.3) in Figure 4.36.

As with the emergent arrays, we use the non-dimensional drag per unit length of cylinder, $f_D/\mu U_h$, to investigate the Reynolds number dependence of C_d . The results resemble a quadratic relationship rather than the expected linearity (Figure 4.37-left). A similar behavior is found by Koch and Ladd (1997), but only at very low $Re_d < 1$, with a transition to a linear dependence (Eq. (4.5)) around $Re_d \approx 3$. Attempts to fit the data to create a set of curves $C_d(Re_d)$ are conducted, assuming both linearity (Eqs. 4.5-4.6, Figure 4.37-center), and a quadratic form (Eqs. 4.14-4.15, Figure 4.37-right).

$$\frac{\langle \overline{f_D} \rangle}{\mu U_Q} = \beta_0 + \beta_1 Re_d + \beta_2 Re_d^2 \quad (4.14)$$

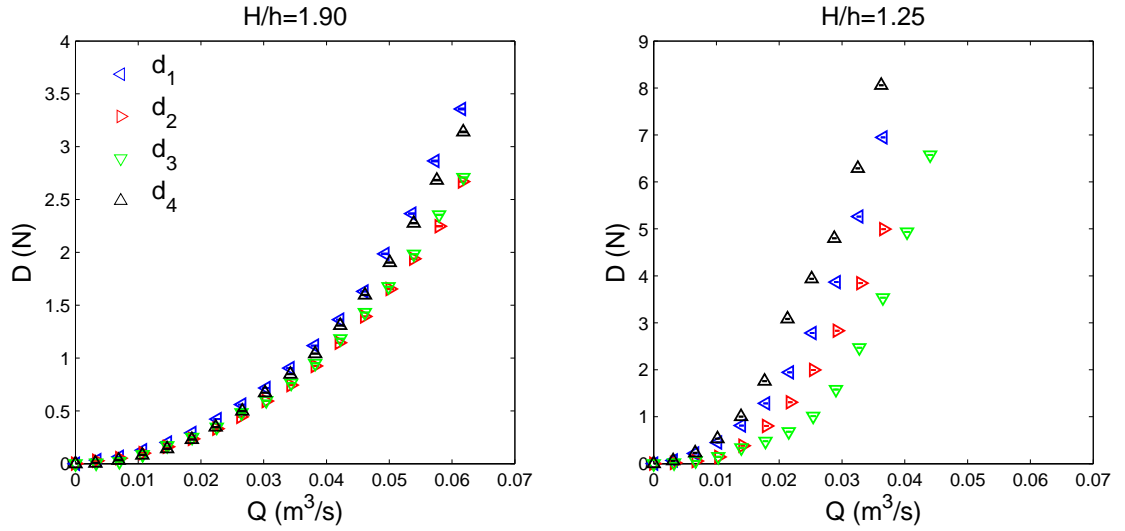


Figure 4.31: Measured drag, D (N), as a function of Q (m^3/s) for both submergence ratios. Vertical error bars (smaller than symbols) indicate 95%CI.

$$C_d = 2 \left(\frac{\beta_0}{Re_d} + \beta_1 + \beta_2 Re_d \right) \quad (4.15)$$

The linear fit fails to capture the apparent increase in C_d as Re_d increases, while the quadratic fit suggests a rapid and continuous growth of C_d . We noticed that the Re_d values at which C_d starts increasing are not the same for all diameters, and hypothesize that it occurs due to the transition from laminar to turbulent cylinder wakes. For a single cylinder, vortex shedding is expected around $Re_d \approx 50$, and the wakes to become turbulent around $Re_d \approx 200$ (Kundu and Cohen, 2004), but these transition points depend on the level of turbulence of the flow (Williamson, 1996). Increased intensity of fluctuations in the flow approaching a cylinder (as those generated by the wakes of upstream cylinders) will delay the onset of vortex shedding and consequently delay the transition to turbulence (Nepf and Vivoni, 2000), which can explain why this occurs at different Re_d for each diameter. The additional shear-scale turbulence from the drag discontinuity at the canopy top would explain why we observe this behavior in submerged cylinders, but not in the emergent array.

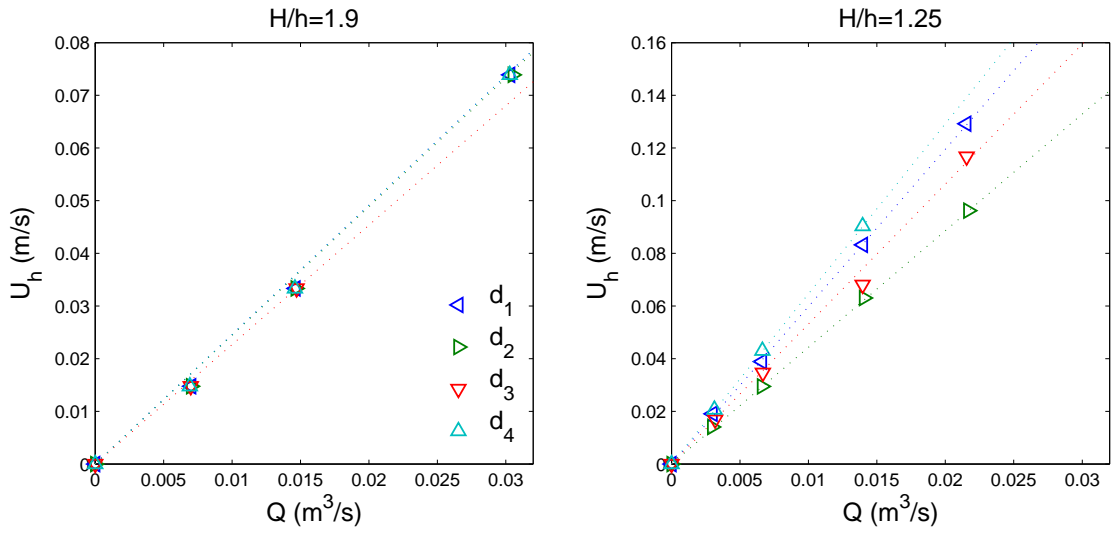


Figure 4.32: Depth averaged velocity within the array as a function of Q for both submergence ratios studied. Dotted lines represent linear fits to the data.

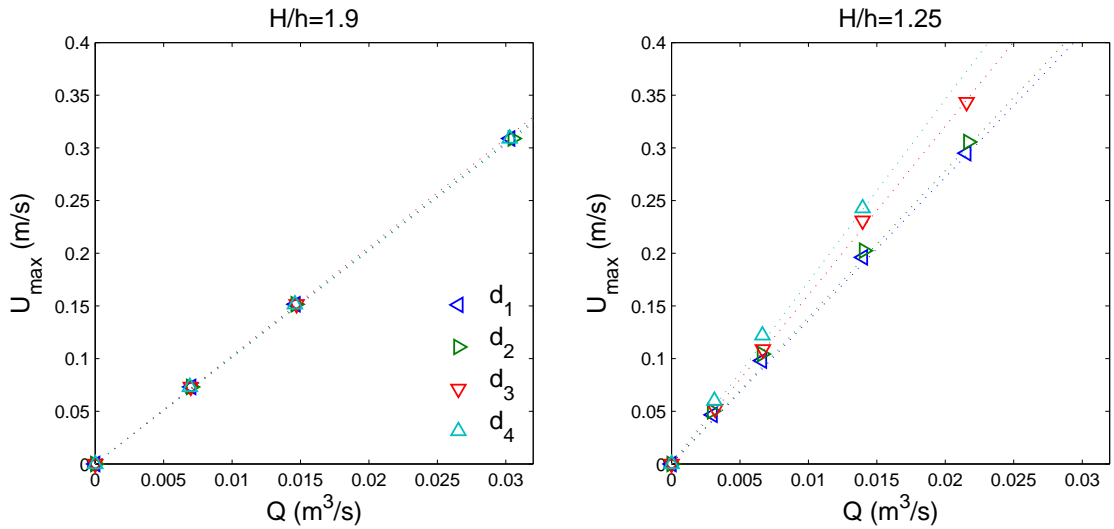


Figure 4.33: Maximum longitudinal velocity as a function of Q for both submergence ratios studied. Dotted lines represent linear fits to the data.

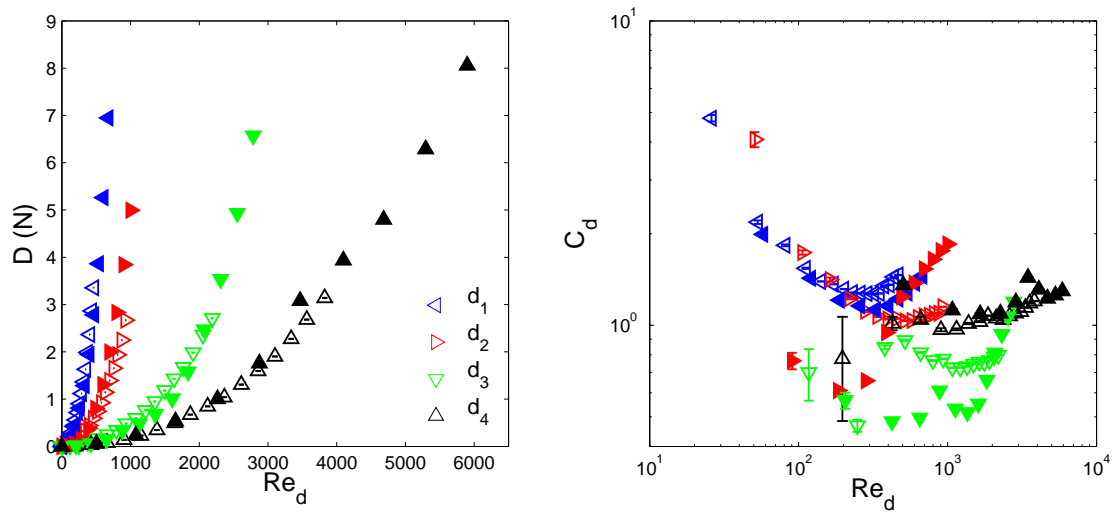


Figure 4.34: Measured drag, D , and C_d , as a function of Re_d for $H/h = 1.9$ (open symbols) and $H/h = 1.25$ (solid symbols).

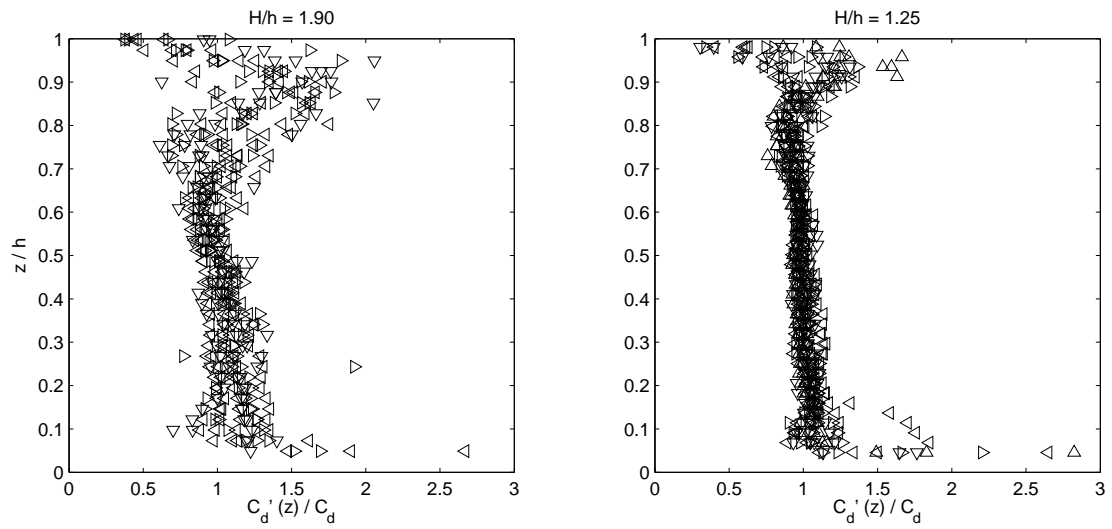


Figure 4.35: Vertical profiles of the ratio $C'_d(z)/C_d$ for submergence ratios $H/h = 1.9$ and $H/h = 1.25$.

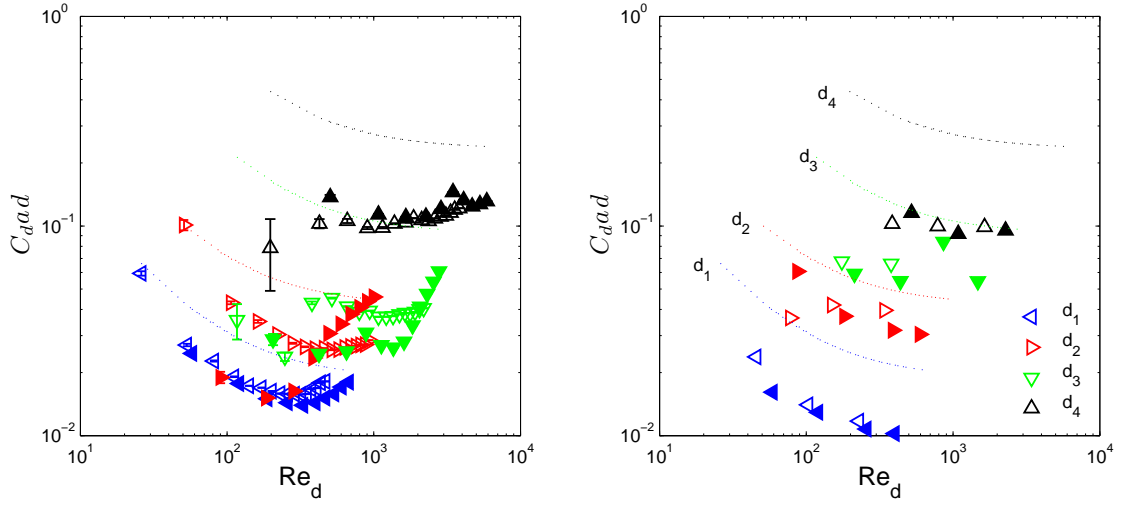


Figure 4.36: C_{dad} as a function of Re_d for $H/h = 1.9$ (open symbols) and $H/h = 1.25$ (solid symbols), calculated from the measured drag (left) and estimated values from momentum equation (right). Dotted lines indicate the value of C_{dad} expected from emergent cylinders.

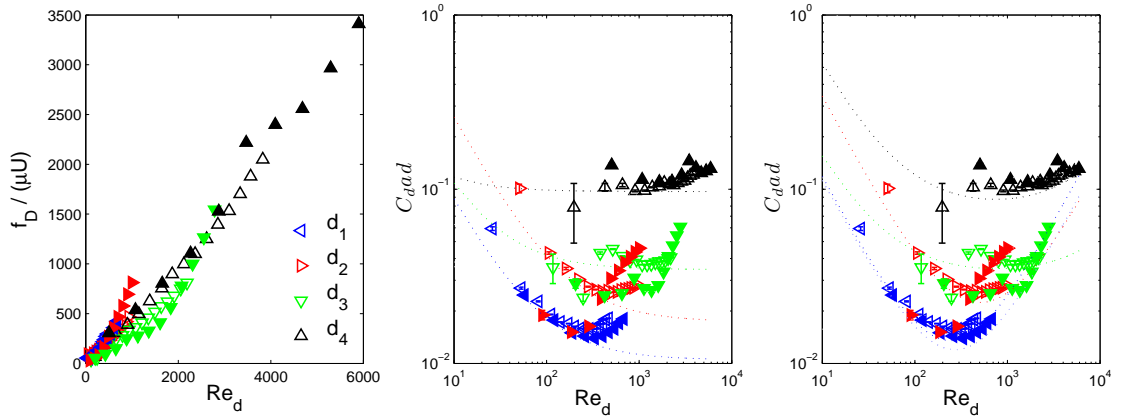


Figure 4.37: C_{dad} as a function of Re_d for $H/h = 1.9$ (open symbols) and $H/h = 1.25$ (solid symbols). Dotted lines indicate the linear (center) and quadratic (right) fits.

4.4.3 Analysis of momentum and tke budgets

As discussed in Section 1.3, the momentum equation for flow through submerged arrays of rigid cylinders is expected to be a balance of pressure, stress gradients, and canopy drag, as stated in Eq. 1.8.

In Figure 4.38, we present the calculated, temporally- and horizontally-averaged values for each term at one particular flow rate for both submergence ratios. The vertical profiles are calculated from PIV data at each of the three lateral sections and averaged horizontally, and we use the actual measured drag coefficients (bulk C_d , constant over h). We also include the viscous stress and advective terms (I and IV, Eq. 4.16) to investigate their relevance, the first being negligible for all cases, while the latter appears to reach the same levels as the Reynolds stress gradient, which can be attributed to a) the flow not being fully developed for all flow rates, as evidenced by the lack of a fully linear Reynolds stress profile from the canopy top to the free surface in Figure 4.26, and b) the localized relatively high magnitude vertical velocities found for $H/h = 1.90$ (Figure 4.19), which could be averaged out had we used more than three lateral sections.

$$0 = -W \frac{\partial \langle \bar{u} \rangle}{\partial z} - gS - \frac{\partial \langle \overline{u'w'} \rangle}{\partial z} + \nu \frac{\partial^2 \langle \bar{u} \rangle}{\partial z^2} - \frac{1}{2} C_{da} U^2 \quad (4.16)$$

$$0 = I + II + III + IV + V$$

The tke budget is also investigated. In particular, the challenge of measuring the rate of dissipation of tke has been addressed by several research groups. We calculate dissipation from the PIV data, using the second order velocity structure function D_{LL} , which has been found to be one of the most robust methods to estimate ϵ (Doron et al., 2001; Variano and Cowen, 2008; DeJong et al., 2009).

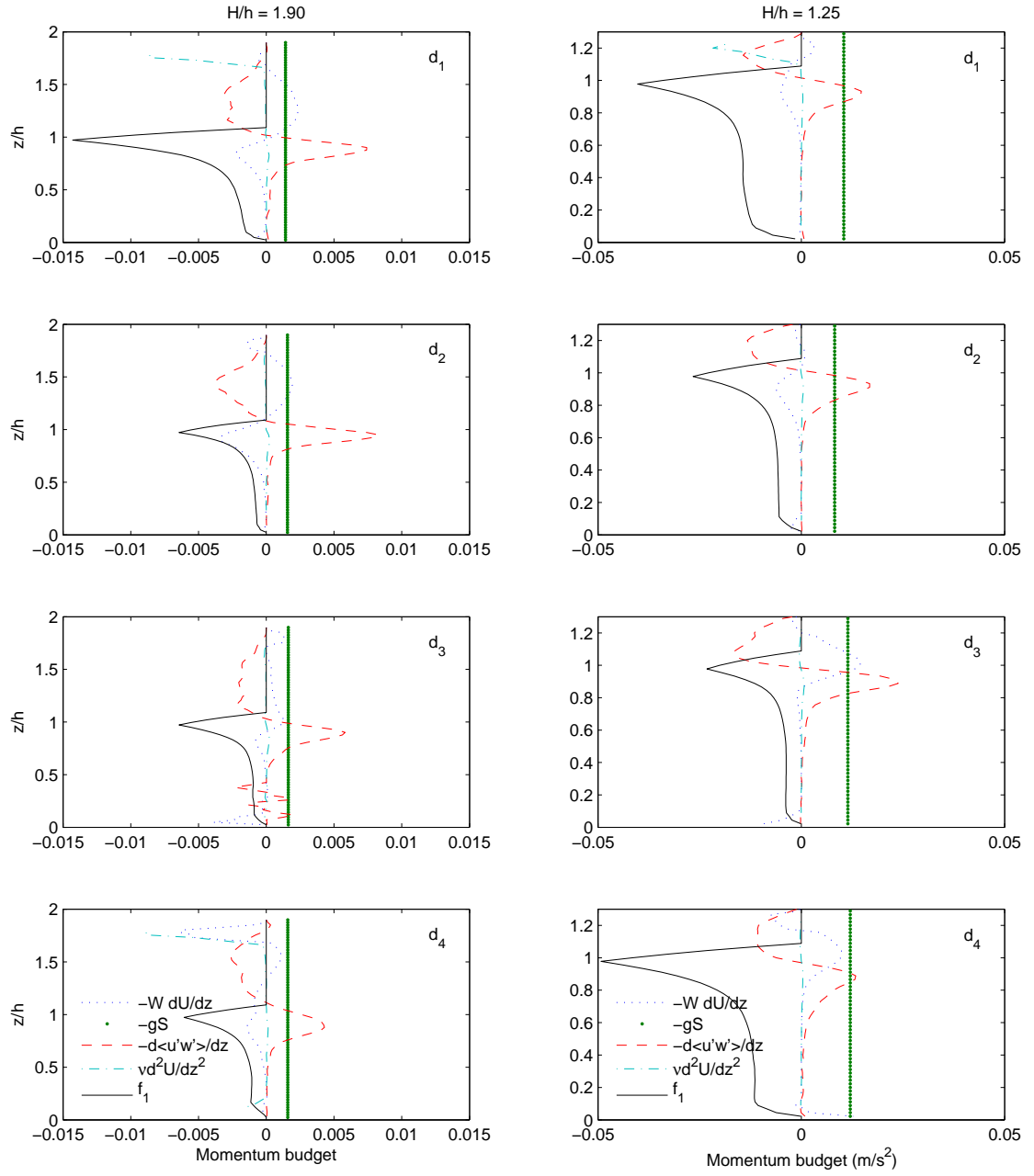


Figure 4.38: Momentum budget terms (Eq. 4.16) for the four studied arrays of submerged, rigid cylinders, $d = \{0.31, 0.62, 1.27, 2.53\}cm$, at $H/h = 1.9$, $Re_d = \{100, 150, 380, 790\}$ (left column), and $H/h = 1.25$, $Re_d = \{260, 390, 860, 2280\}$ (right column),

By definition, D_{LL} is the covariance of the difference in velocity between two points $x + r$ and x (Pope, 2000).

$$D_{LL} = \langle [U(x + r, t) - U(x, t)][U(x + r, t) - U(x, t)] \rangle \quad (4.17)$$

In the inertial subrange, D_{LL} can be expressed in terms of ϵ , r , and a universal constant $C_2 = 2.0$ (Pope, 2000). Dissipation is thus calculated by a linear fit in the inertial subrange from a compensated D_{LL} (Eq. 4.18).

$$\epsilon_{DLL}^{2/3} = \frac{D_{LL}}{C_2 r^{2/3}} \quad (4.18)$$

Calculation of dissipation at three elevations for a single flow rate are presented in Figure 4.39. Vertical profiles of dissipation are calculated first at each of the three lateral locations, and then horizontally averaged.

We test two dissipation estimates. Shear scale canopy dissipation, defined as $\epsilon_s = \frac{1}{2}C_d a U (\langle 2\overline{u^2} \rangle + \langle \overline{v^2} \rangle)$ (Finnigan, 2000; Ghisalberti and Nepf, 2004), represents the conversion of shear scale turbulence into wake scale eddies, valid at the exchange zone ($z_1 < z < h$) of the mixing layer. Wake dissipation, $\epsilon_w = k^{3/2}/d$, indicates the rate at which wake scale turbulence is dissipated into heat. We found large variations between ϵ_{DLL} , ϵ_s , and ϵ_w (Figure 4.40). It is noticed that for $H/h = 1.9$, ϵ_w does a better job in regions far from the influence of the mixing layer, but for the upper region of the canopy, ϵ_s gives better approximations. For the $H/h = 1.25$ case ϵ_w closely follows the calculated ϵ_{DLL} . Notice that both estimates can be only used within the array (i.e. $z/h < 1$).

The rest of the z -dependent, temporally- and horizontally-averaged terms on

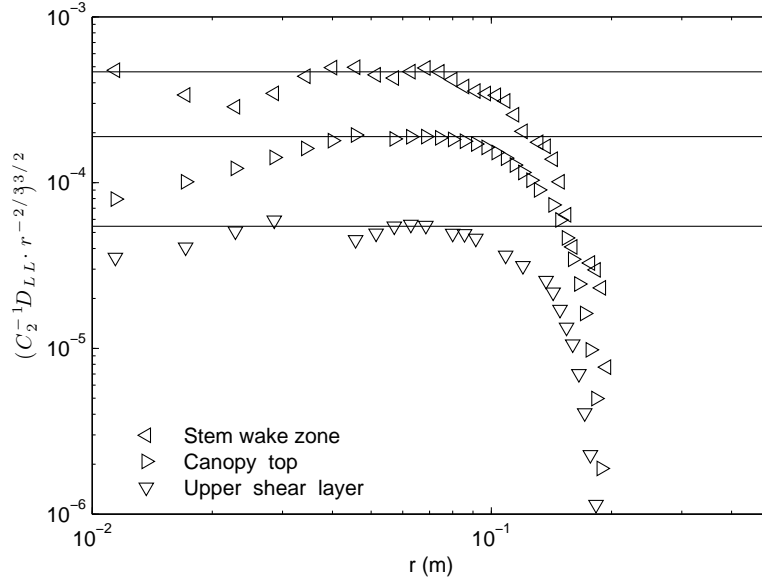


Figure 4.39: Determination of dissipation from a compensated second order structure function (Eq. 4.18). Fits for three elevations at a single flow rate for the $d = 0.0253m$ array are presented.

the tke budget, Eq. 4.19, are likewise calculated from the PIV data at each y -section and horizontally averaged. The shear production, P_s , is the rate at which tke is produced by the work of the Reynolds stress against the mean velocity gradient. Wake production, P_w , is the work done by the flow against form drag, and T is the turbulent transport, affected by the multiple scale eddies over the water column. Each term is defined in Eq. 4.19 to 4.22.

$$0 = T(z) + P_s(z) + P_w(z) - \epsilon(z) \quad (4.19)$$

$$P_s = -\langle u'w' \rangle \frac{\partial U}{\partial z} \quad (4.20)$$

$$P_w = \frac{1}{2} a C_d U^2 |U| \quad (4.21)$$

$$T = \frac{\partial}{\partial z} \left[\nu_t \frac{\partial k}{\partial z} \right] \quad (4.22)$$

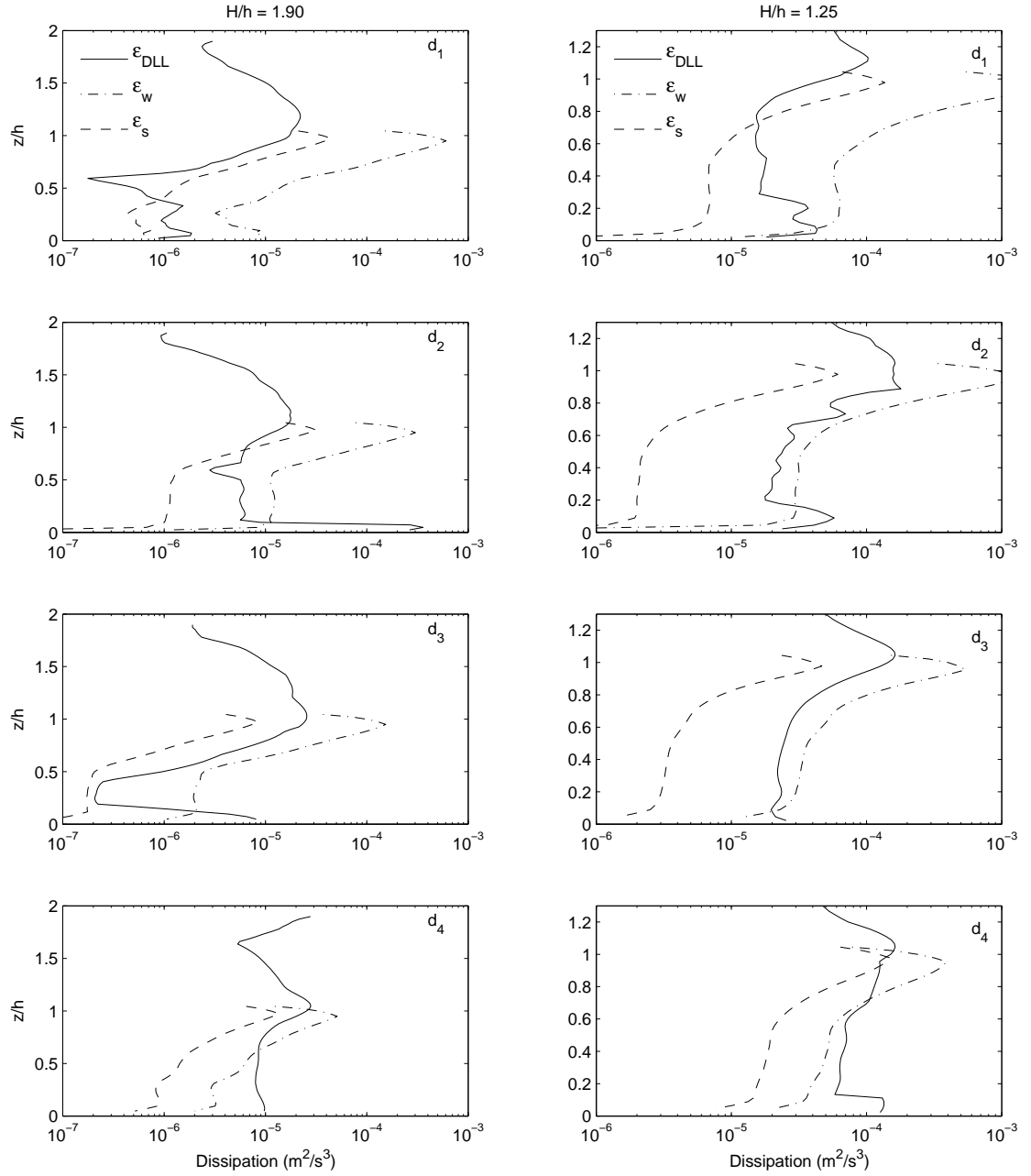


Figure 4.40: Dissipation values from the second order structure function, ϵ_{DLL} (solid line), compared against the model estimates ϵ_s (dashed line) and ϵ_w (dash dotted line), valid only in the shear and wake regions respectively, for the four studied arrays of submerged, rigid cylinders, $d = \{0.31, 0.62, 1.27, 2.53\} \text{cm}$, at $H/h = 1.9$, $Re_d = \{50, 80, 180, 390\}$ (left column), and $H/h = 1.25$, $Re_d = \{120, 180, 440, 1080\}$ (right column).

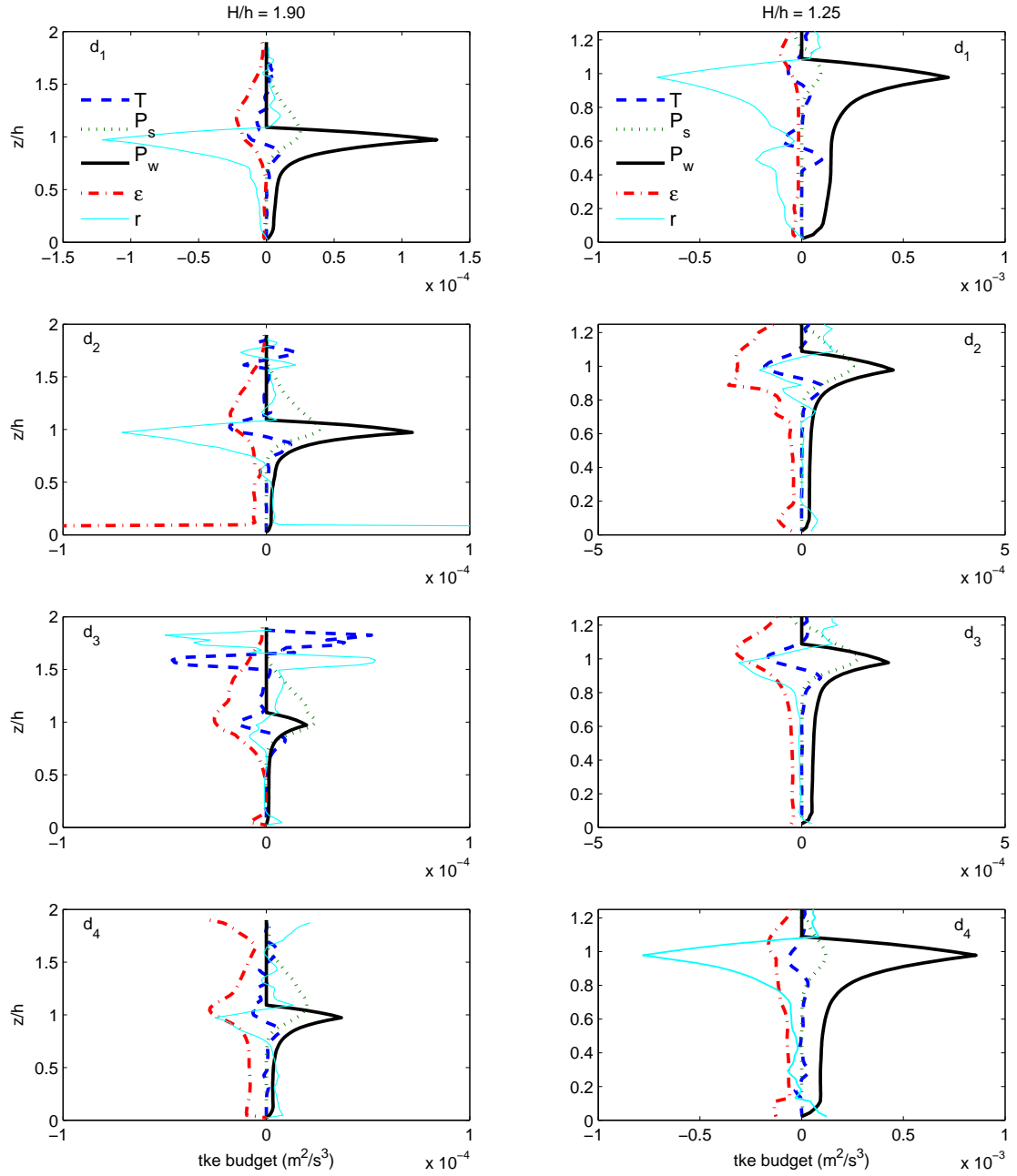


Figure 4.41: TKE budget terms (Eq. 5.6) for the four studied arrays of submerged, rigid cylinders, $d = \{0.31, 0.62, 1.27, 2.53\} \text{ cm}$, at $H/h = 1.9$, $Re_d = \{50, 80, 180, 390\}$ (left column), and $H/h = 1.25$, $Re_d = \{120, 180, 440, 1080\}$ (right column).

Results are shown in Figure 4.41. Well within the array we notice a balance between wake production and dissipation, with shear production becoming important at the canopy top, where we notice a loss in turbulent transport. We notice a large, unbalanced value of P_w for d_1 at both submergence ratios (Figure 4.41). The definition of P_w implies that all energy extracted by drag on the stems appears as tke, and as we discussed in Section 4.4.2, fluctuations in the flow due to upstream cylinders can delay the onset of vortex shedding and the transition to turbulent wakes until $Re_d > 200$ (Williamson, 1996; Nepf and Vivoni, 2000), and in the absence of vortex shedding, viscous drag dissipates mean flow energy without generating tke, rendering our calculated P_w as only an upper limit for $Re_d \lesssim 200$.

4.5 Conclusions

Data from experiments on rigid, emergent cylinders yields a family of C_d curves, as a function of solid volume fraction ϕ . We find advantages in using the non-dimensional parameter $C_d ad$, instead of C_d , namely a more clear graphic representation of the dependence $C_d = C_d(\phi)$, and a simpler way to estimate $C_d ad$ for $Re_d > 1000$.

Predicted C_d values, using the curves found from rigid cylinder experiments, give a good approximation to the order of magnitude of the measured coefficients in submerged conditions, but they over predict C_d for as much as 50%. We hypothesize that this apparent reduction on C_d for submerged arrays in comparison to the emergent case, can be attributed to interaction between cylinder wakes and the coherent structures from the shear layer, which would explain the observed behavior of C_d for the submerged case.

Analysis of velocity spectra clearly show two relevant scales at which tke is injected into the flow. For emergent arrays, the wake-scale controls the generation

of tke , while for submerged arrays both the shear-scale and wake-scale appear, where the shear-scale eddies dominate.

The drag coefficient is often left as a calibration parameter, to close the balance of the momentum and tke budgets. Estimates of dissipation using a scaling argument, assuming the cylinder diameter as the length scale, yield good approximations when compared to the more robust estimate from D_{LL} , especially for $H/h = 1.25$. The measured drag coefficients perform satisfactorily at balancing momentum and tke budgets, raising our expectations to use predicted values, from our rigid cylinder studies, in more complex canopy morphologies.

Chapter 5

Flow through and above canopies of flexible, live vegetation

5.1 Introduction

Studies of vegetated flow often rely on indirect estimations of drag and drag coefficients. Reynolds stress profiles, free surface slope, and momentum balance are commonly used to estimate the drag (Dunn et al., 1996; Nepf, 1999; Ackerman and Hoover, 2001; Lightbody and Nepf, 2006; Ghisalberti and Nepf, 2006; Luhar et al., 2008). Other research groups have taken a direct approach to measure vegetated drag, either with laboratory set-ups (Fathi-Maghadam and Kouwen, 1997; Freeman et al., 2000; Sand-Jensen, 2003), or building submersible, field devices (Callaghan et al., 2007).

Sand-Jensen (2003) measured the drag on live stems of different species placed on a $0.15 \times 0.17\text{m}$ platform suspended from a rail above a flume, connected to a spring balance to measure the force. Given the small size of the platform, that the stems were placed on the platform only, and that it did not cover the whole flume width (0.30m), further studies would be required to extrapolate their developing

flow results to predict drag under large-scale natural conditions. Fathi-Maghadam and Kouwen (1997) measured bulk velocities and drag on model trees by mounting a system of load cells on a force-balance apparatus flush with the flume bottom. In a related study, Freeman et al. (2000) covered a flume with different species of vegetation and measured the drag in a selected single plant at mid-width mounted on a platform allowed to displace over ball bearings, which compressed a strain gage that recorded the exerted drag. However, to infer meaningful drag one must spatially average over multiple plants under appropriate forcing and the approaches discussed above are not capable of achieving this. Callaghan et al. (2007) built a submersible drag measurement system, consisting of a movable trolley allowed to displace in one direction over ball bearings to compress a load cell. The system is enclosed in a rigid housing that allows it to mount flush with the bottom of either a laboratory flume or a natural stream. Its dimensions ($0.724m \times 0.208m$) suggest that it can measure forces over several elements, but it has only been tested with a single element attached to it.

Other researchers have addressed the parametrization of the plant morphology (bending and characteristic obstructed areas) to estimate the drag (Sand-Jensen, 2003, 2005; Green, 2005b; Sukhodolov, 2005; Statzner et al., 2006). They develop an interesting discussion as to what are the most appropriate parameters for a standard calculation of drag coefficients on flexible vegetation, whether they include the projected frontal area of harvested stems (first approach in Section 2.7), the frontal area of the bent plants (our second approach in Section 2.7), or even lateral and top-view projections.

We carried out a detailed analysis of the projected frontal area of the vegetation as it bends and sways with increasing flow rates. We used quantitative imaging to capture the mean values of obstructed area and its temporal variability, generating time series of $a(z)$ that allow us to clearly see the changes in canopy height and

the periodicity of the plant oscillations.

In this Chapter, we investigate how the coupling of the velocity-dependent a profiles and the direct drag measurements can aid in calculating more accurate drag coefficients than that estimated from velocity statistics.

5.2 Experimental procedure

A 3.66m long canopy of $\sim 25\text{cm}$ tall live stems of Eurasian watermilfoil (*Myriophyllum spicatum*), was created in an 8.0m long recirculating open-channel flume (see Sections 2.2 and 2.4 for details). While the plant height used for this study only represents the shortest canopies found in the field, the relationships found from our results are expected to be representative of and applicable to natural conditions, given its high flexibility and essentially constant stem diameter and branching pattern (i.e., independent of plant height). *Myriophyllum spicatum* is found in lakes, ponds, reservoirs and low energy areas of rivers and streams, thus usually experiences very low flow speeds. The same PIV setup as used for the measurements made in the rigid cylinder arrays was used (Figure 5.1), with an Argon-Ion laser, and a rotating mirror to generate the light sheet from the top (details in Section 2.6).

Three plant densities were studied, $n = \{100, 300, 500\}\text{stems}/\text{m}^2$. Experiments were conducted at two water depths, $H = 0.37$, and 0.20m . Field and laboratory observations on canopies of *Myriophyllum spicatum* have found a decline in milfoil population due to the presence of an aquatic lepidopteran larva, *Acentria ephemerella* (Johnson et al., 1998; Gross et al., 2001). *Acentria*'s primary feeding site is the apical meristem, inhibiting shoot growth and thus preventing the formation of taller and denser canopies. By studying the flow field on different plant densities and submergence conditions, we expect to provide valuable infor-



Figure 5.1: Side view of the flume and the PIV setup, flow from left to right. The head of the Argon-Ion laser is noticed at the left, followed by the shutter and an array of mirrors to bring the light sheet from the top. Notice the stems removed at the downstream edge of the drag plate for PIV access, below the location of the rotating mirror.

mation as to how the reduction of canopy height and population of *Myriophyllum spicatum*, as observed under the abundance of *Acentria*, changes the flow conditions, which can in turn impact the effectivity of the herbivore as a natural control for milfoil invasions.

Given the increased complexity of the plant morphology as compared with the rigid cylinders, PIV analysis was conducted at 7 lateral locations, $y = \{9, 16, 23, 30, 37, 44, 51\}cm$, to get more accurate laterally averaged statistics. Sets of 1030 images were captured at $2Hz$ for the 6 off-centerline lateral locations and of 8200 images at $20Hz$ for the centerline location, with a Δt ranging from $10ms$ to $50ms$, yielding $1Hz$ and $10Hz$ velocity fields, respectively. Images are post-processed as detailed in Section 2.6. Figure 5.2 presents an example of the measured velocity variations from the seven vertical profiles for a submerged, and an emergent experiment, along with the mean and 95CI from an uncertainty analysis using a bootstrap method (Efron and Tibshirani, 1993).

Four flow rates were studied for the emergent, $H = 0.37m$ case, and six for the emergent, $H = 0.20m$ case. For the two highest flow rates of the emergent case, the plants bend, creating a nearly emergent situation, similar to the $H/h = 1.25$ scenario for rigid cylinders. Flow rates, free surface slope, and drag, are measured

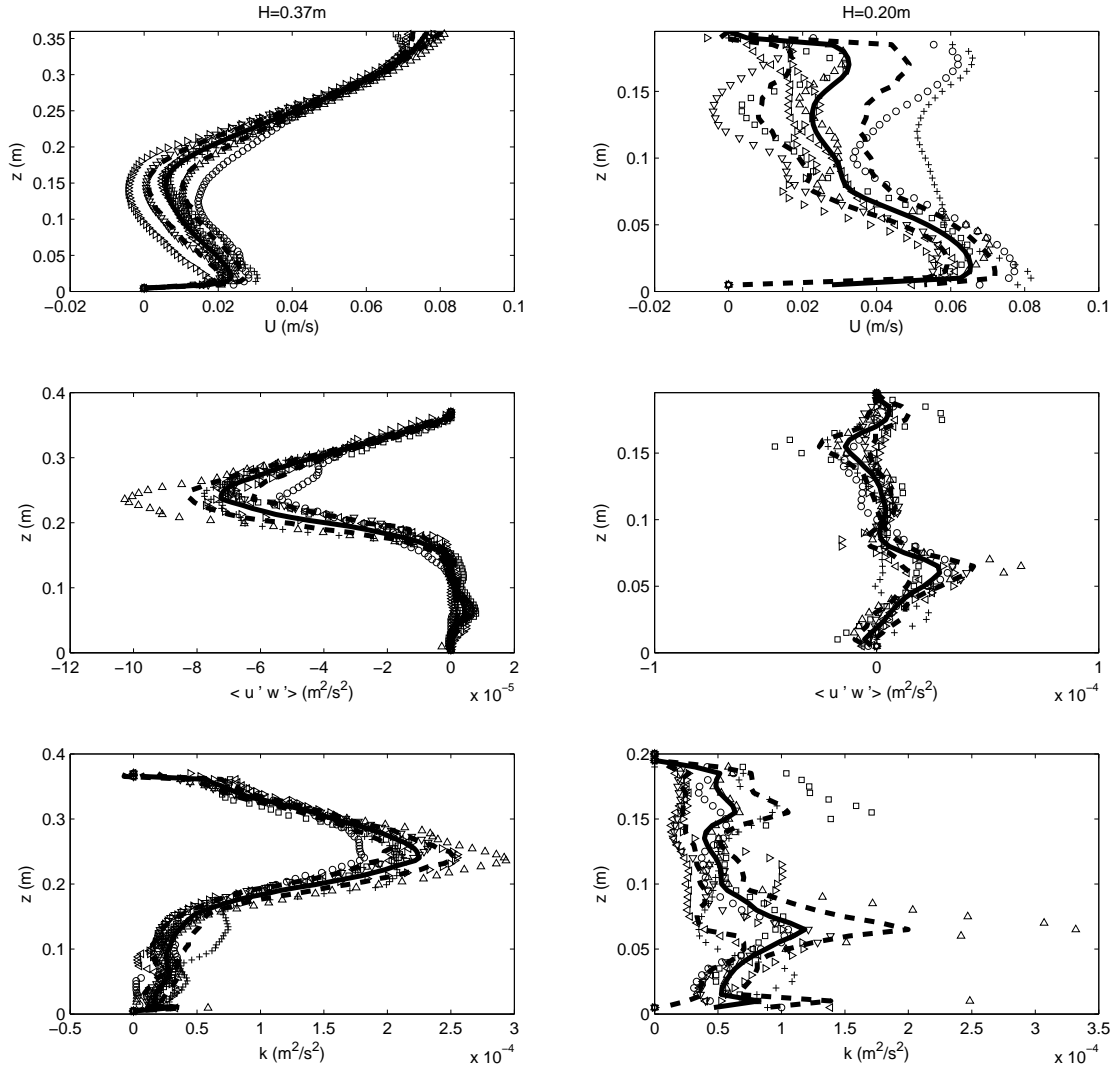


Figure 5.2: Vertical profiles of longitudinal velocity, U (top), Reynolds stresses, $\langle u'w' \rangle$ (middle), and turbulent kinetic energy, k (bottom), at the seven sections studied (open symbols) for a single flow rate for the submerged (left) and emergent cases (right). Solid and dashed lines indicate the horizontal average and the 95CI, respectively.

for each experiment at each y -location and later averaged.

Relevant parameters for each experiment, such as flow rate, Q , measured canopy height, h , submergence ratio, H/h , mean velocity at the canopy top, U_{hp} , depth averaged velocity, U_h , depth averaged frontal area, a_h , maximum frontal area observed, a_{max} , amplitude and period of the observed *monami*, A_w and T , are presented in Tables 5.1 and 5.2. Details on the calculation of each parameter are given shortly.

5.3 Results

5.3.1 Characterization of real vegetation

Quantitative imaging was used to measure a , as detailed in Section 2.7. From the time series of frontal area, a periodic waving (*monami*) is noticed for all emergent ($H = 0.37m$) experiments (Figure 5.3). The period, T (s), and wave amplitude, A_w (m), for each submerged experiment are measured from figures of the time series and confirmed by looking at the frequency spectra.

The results are presented in Table 5.1. Stems of *Myriophyllum spicatum* are fairly buoyant ($SG = 0.8$ (Koegel et al., 1973)), very flexible, and unable to stand upright outside of the water, so it is bouyancy that provides the restoring force as the stems are pushed down, as opposed to other species (e.g., *Spartina alterniflora*, *Cladium jamaicense*) where rigidity limits the motion of the stems.

A time averaged, vertical profile $a(z)$ is obtained for each flow rate (Figure 5.4). For both cases, $H = 0.37$ and $0.20m$, the plant reconfiguration as the flow rate increases is evident, reducing almost 50% the plant height for the deeper series, and creating a transition from emergent to nearly emergent in the shallow case. Figure 5.4 clearly shows the implications of using a single, bulk a value, or even

Table 5.1: Relevant parameters for the $H = 0.37m$ case, with flexible vegetation.

	n (stems/m ²)	Q (m ³ /s) $\times 10^{-3}$	h (m)	H/h	U_{hp} (m/s) $\times 10^{-2}$	U_h (m/s) $\times 10^{-2}$	Re_{de} $\frac{U_h d_{eh}}{\nu}$	a_h (m ⁻¹) $\frac{1}{h} \int a(z)$	a_{max} (m ⁻¹)	A_w (m) $\times 10^{-2}$	T (s)
Q_{02}	100	2.8	0.248	1.48	1.52	1.17	50	0.40	0.74	0.3	14.0
Q_{04}	100	6.3	0.236	1.53	3.35	2.38	95	0.40	0.72	0.6	8.5
Q_{08}	100	13.3	0.185	1.95	4.89	4.25	180	0.42	0.73	1.7	9.2
Q_{16}	100	27.8	0.134	2.66	9.41	7.85	300	0.39	0.59	3.0	5.6
Q_{02}	300	3.1	0.250	1.48	1.85	0.92	50	1.68	3.19	0.3	12.5
Q_{04}	300	6.7	0.241	1.53	3.63	1.88	100	1.57	3.06	1.7	17.1
Q_{08}	300	14.0	0.200	1.85	6.04	3.62	185	1.53	2.73	3.5	12.4
Q_{16}	300	29.0	0.160	2.31	11.84	7.15	315	1.32	2.63	1.0	4.1
Q_{02}	500	3.1	0.245	1.48	1.76	0.64	30	2.14	3.63	0.5	39.2
Q_{04}	500	6.8	0.236	1.50	3.55	1.53	65	2.07	3.33	2.4	26.3
Q_{08}	500	14.5	0.217	1.63	7.46	3.48	125	1.79	3.32	4.6	19.8
Q_{16}	500	30.2	0.185	1.90	13.05	6.45	195	1.52	2.87	2.6	10.0

Table 5.2: Relevant parameters for the $H = 0.20m$ case, with flexible vegetation.

	n (stems/m ²)	Q (m ³ /s) $\times 10^{-3}$	h (m)	H/h	U_h (m/s) $\times 10^{-2}$	Re_{de} $\frac{U_h d_{eh}}{\nu}$	a_h (m ⁻¹) $\frac{1}{h} \int a(z)$	a_{max} (m ⁻¹)
Q_{01}	100	1.5	0.195	1.0	1.25	55	0.43	0.91
Q_{02}	100	2.6	0.195	1.0	2.80	130	0.47	1.06
Q_{03}	100	4.3	0.195	1.0	4.20	150	0.37	0.72
Q_{04}	100	5.8	0.195	1.0	5.50	220	0.40	0.59
Q_{05}	100	7.5	0.175	1.1	6.96	235	0.34	0.56
Q_{08}	100	12.8	0.140	1.4	10.81	375	0.35	0.56
Q_{01}	300	1.5	0.195	1.0	1.11	45	1.25	1.94
Q_{02}	300	2.6	0.195	1.0	2.33	100	1.32	2.63
Q_{03}	300	4.3	0.195	1.0	3.63	130	1.09	2.68
Q_{04}	300	5.8	0.195	1.0	4.96	200	1.23	2.73
Q_{05}	300	7.5	0.165	1.2	6.25	255	1.23	2.49
Q_{08}	300	12.8	0.140	1.4	9.52	340	1.08	2.03
Q_{01}	500	1.5	0.195	1.0	1.08	55	2.52	4.22
Q_{02}	500	2.6	0.195	1.0	2.06	107	2.62	4.40
Q_{03}	500	4.3	0.195	1.0	3.33	160	2.44	3.87
Q_{04}	500	6.0	0.195	1.0	4.80	200	2.08	3.53
Q_{05}	500	7.7	0.190	1.0	6.35	230	1.81	3.28
Q_{08}	500	13.1	0.160	1.2	9.65	310	1.62	2.56

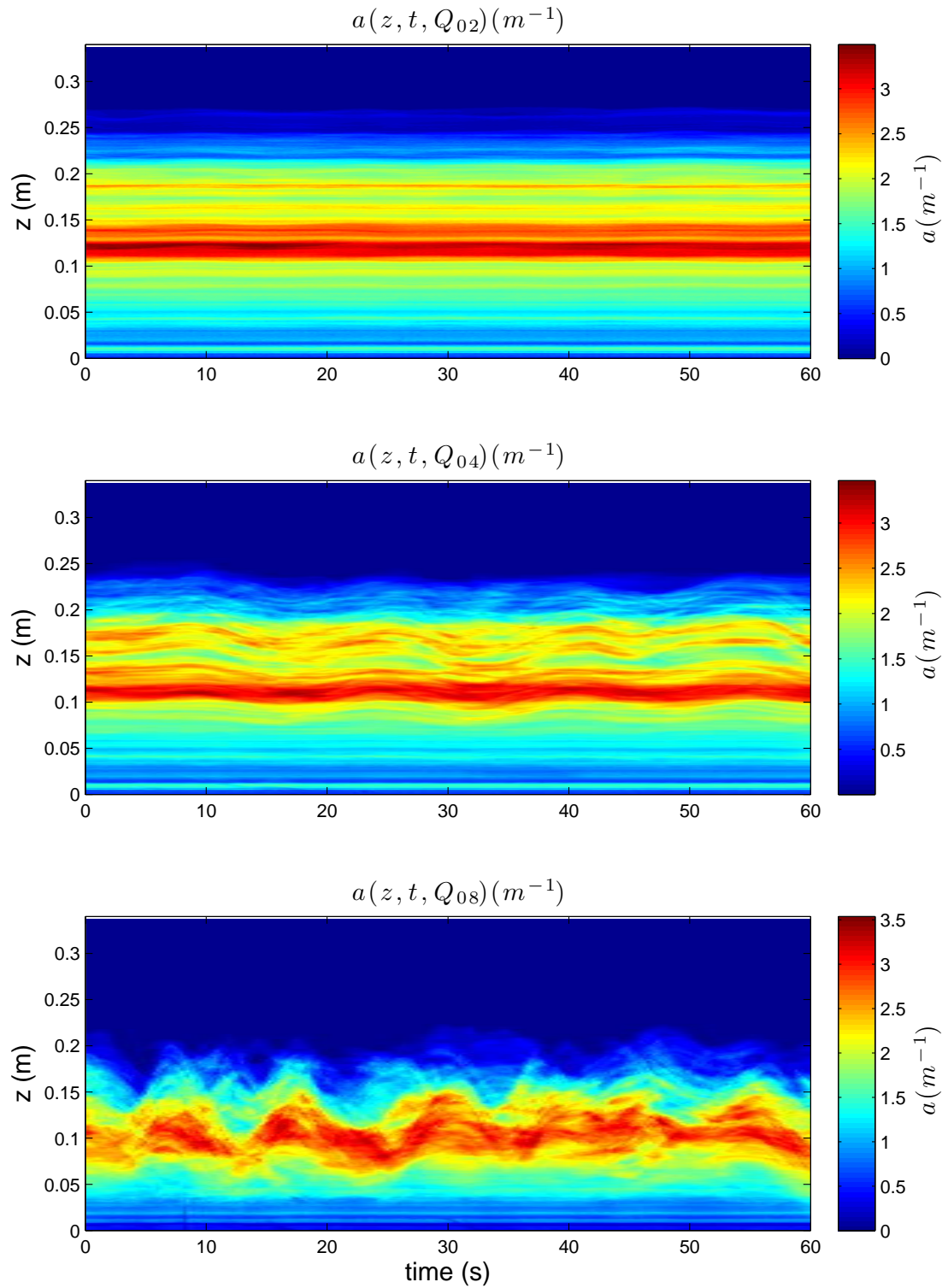


Figure 5.3: Time series of the measured vertical profiles of a (m^{-1}), for $n = 300 stems/m^2$, at $H = 0.37m$ for three of the flow rates studied.

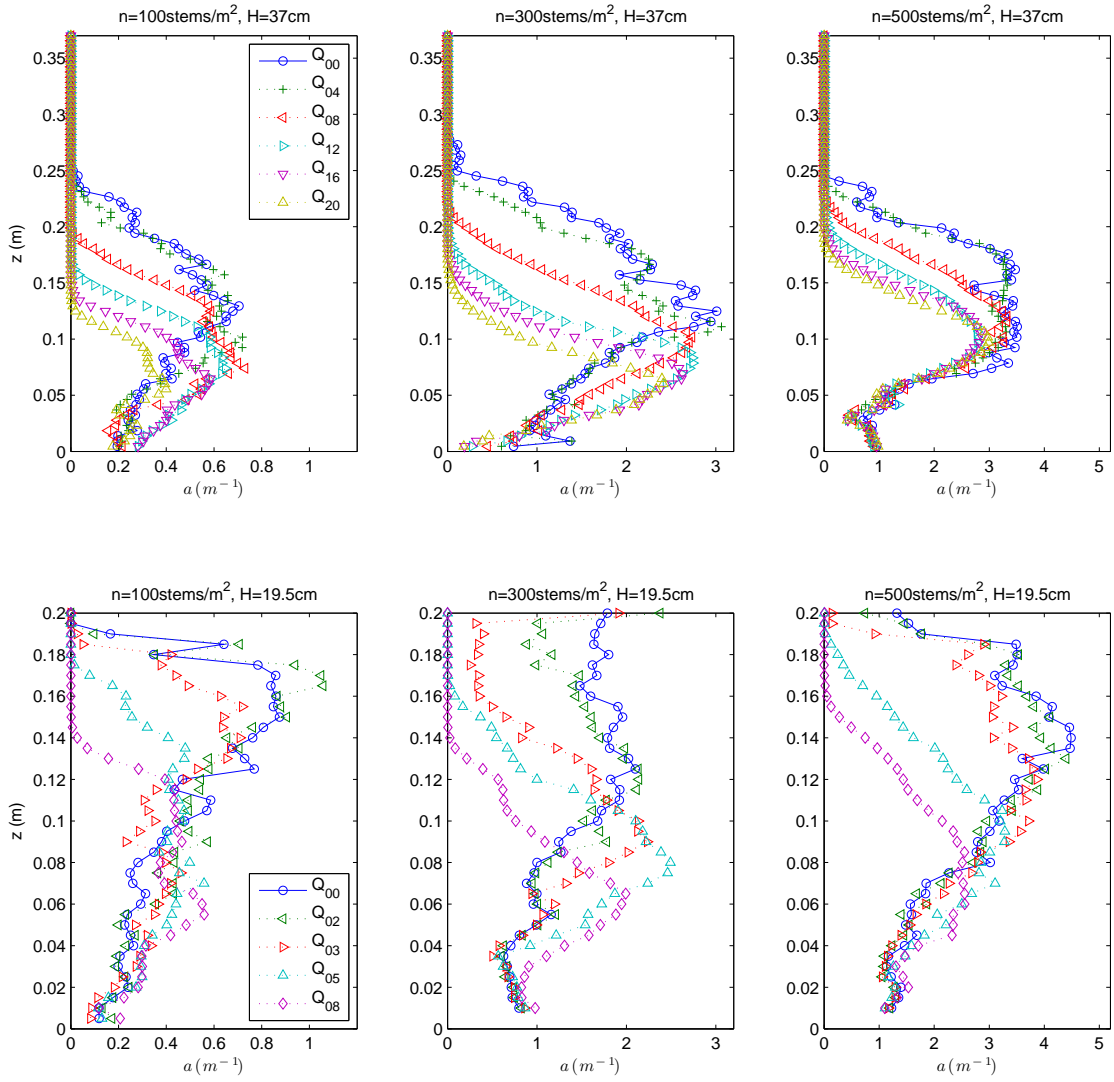


Figure 5.4: Time averaged vertical profiles of a (m^{-1}), for $n = 100, 300,$ and 500 stems/m^2 . Submerged (top row) and emergent (bottom row) series are presented. Notice the decrease in h as the flow rate increases.

a single profile $a(z)$ without considering bending of the plants, which in this case would not only overestimate the obstructed area, but could lead us to completely miss the physical processes occurring in the nearly emergent case, by treating it as fully emergent.

Since h varies with velocity, we define it hereafter as the maximum height recorded from the time series, which is seen to correspond to the mean peak on the Reynolds stress profile.

5.3.2 Flow characterization

We study the three-dimensionality of the flow by taking point measurements of the three components of velocity with an ADV along a vertical, $y - z$ plane, transverse to the flow, at the same longitudinal location where PIV data are acquired. We produce a grid of $\Delta y = 3.0\text{cm}$ and $\Delta z = 1.5\text{cm}$, yielding 396 grid points (22 vertical \times 18 horizontal) for the $H = 0.37\text{m}$ case, and 180 grid points (10 vertical \times 18 horizontal) for the $H = 0.20\text{m}$ case. Records of 164s at 200Hz (2^{14} samples) were acquired at each point. Results for mean velocities, as well as Reynolds stresses and tke are presented in Figures 5.5 and 5.6.

For the submerged case we notice a similar structure as with the rigid cylinders, with regions of downward velocity above the canopy and upward velocity regions within the plants. Due to bending of the plants, now we see large variations in the vertical location of the peak of both Reynolds stress and tke. Both present a maximum value (in magnitude) around the $0.1\text{m} < y < 0.2\text{m}$, corresponding to a local minimum in the longitudinal velocity, which also shows a high upwards vertical velocity, fitting the expected behavior of fluid ejections ($u' < 0$, $w' > 0$) observed in rigid cylinders as well. Analysis of the time series of velocity and Reynolds stresses at the canopy top (Figure 5.7) shows the presence of both sweeps

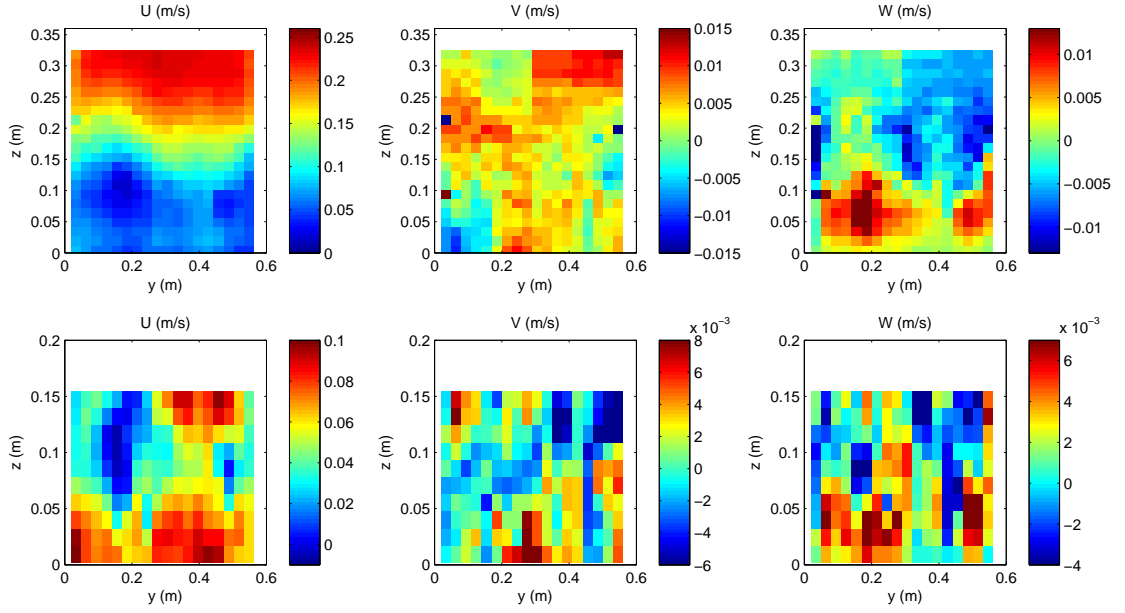


Figure 5.5: ADV measurements of U , V , and W (m/s) along a $y - z$ plane for $n = 500 stems/m^2$, for the submerged $H = 0.37m$ (top row) and emergent $H = 0.20m$ case (bottom row).

($u' > 0, w' < 0$) and ejections ($u' < 0, w' > 0$). These events are also confirmed by a scatter plot of u', w' (Figure 5.8).

Analysis of the power spectra shows the input of energy at the shear scale, which matches the frequency of the observed *monami* (Figure 5.9). At this velocity, the shear-scale eddies seem to propagate along most of the water depth. We notice smaller peaks at higher frequencies for the spectra within the canopy, indicating the input from the different stem scales. The waving frequency of the stems is calculated from frequency spectra of the time series of the frontal area images, using a horizontal average at $z = h$.

Data from the emergent case shows a region with slightly negative U velocities, around $0.1m < y < 0.2m$, where Reynolds stresses are fully damped, and we observe a positive (near bottom) and negative (near top) peak around $0.30m < y < 0.50m$, suggesting that bending of the plants at the right side of the flume is already taking place, demonstrating the large heterogeneity of the canopy, and

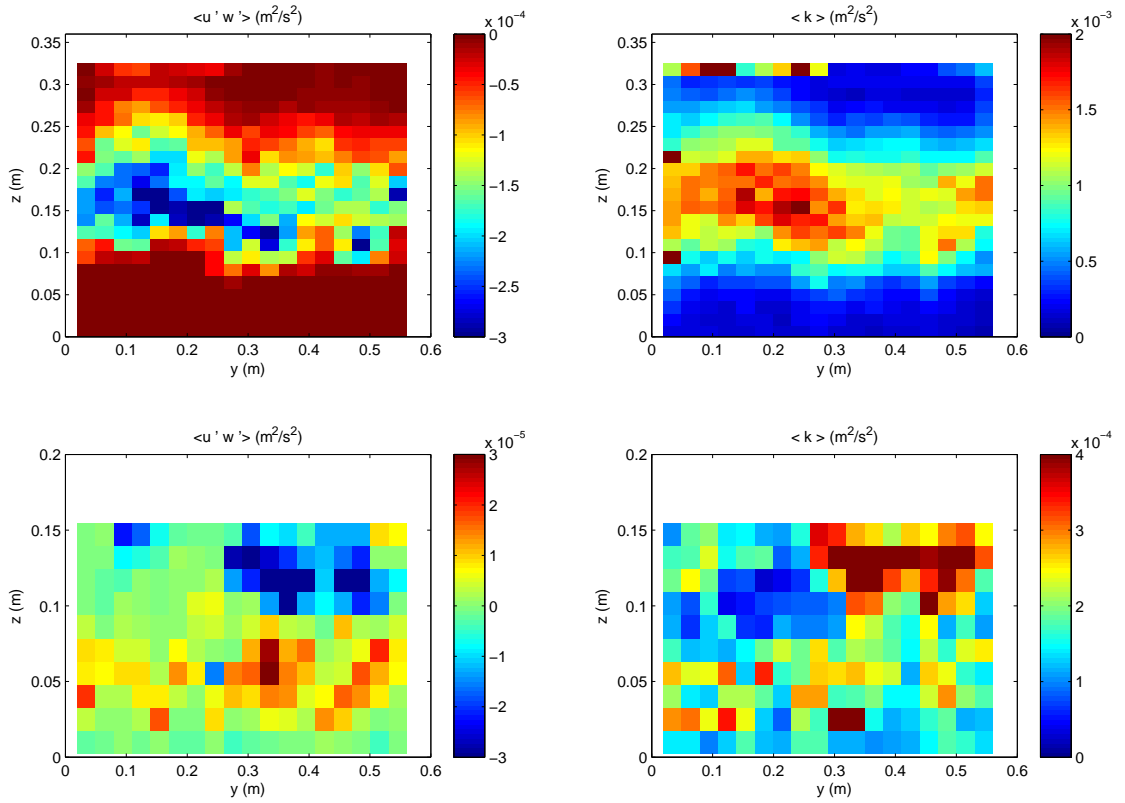


Figure 5.6: ADV measurements of $\langle u'w' \rangle$ and k (m^2/s^2) along a $y - z$ plane for $n = 500 stems/m^2$, for the submerged $H = 0.37m$ (top row) and emergent $H = 0.20m$ case (bottom row).

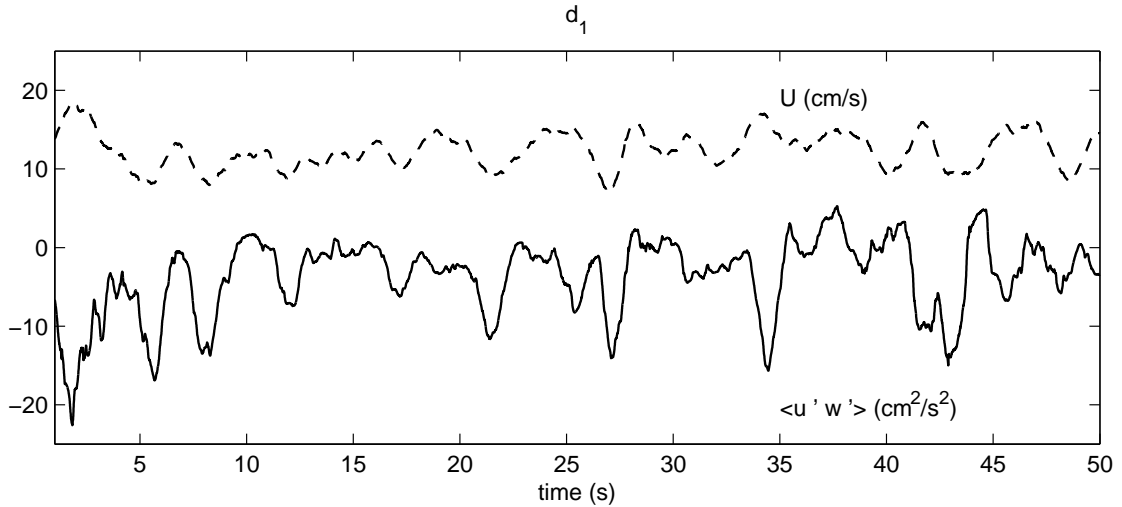


Figure 5.7: Time series of U (cm/s) (dashed line) and $\langle u'w' \rangle$ (cm^2/s^2) (solid line) at $z = 0.15m$ (canopy top). Fluid ejections ($u' < 0, w' > 0$), and sweeps ($u' > 0, w' < 0$), can be identified. Time series smoothed by a $0.5s$ moving average.

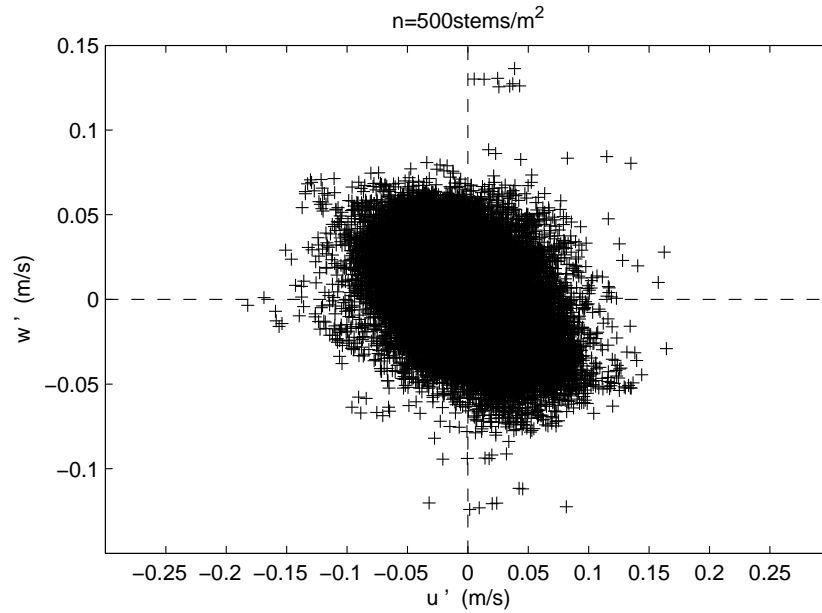


Figure 5.8: Scatter plot of u' , w' , at $z = 0.15m$. The presence of sweeps ($u' > 0$, $w' < 0$) and ejections ($u' < 0$, $w' > 0$) is apparent.

confirming the need for several measurement locations.

5.3.3 Analysis of drag and velocities

Using the h values from the frontal area analysis (Tables 5.1 and 5.2), we can present the non-dimensional results as shown in Figures 5.10 to 5.11. The data shown are laterally averaged from the seven $x-z$ planes studied. For the submerged case, statistics are normalized using $u_*^2 = -\langle u'w' \rangle|_{z=h}$ (Figure 5.10). It is noticed that: A) for the larger submergence ratio the flow is not fully developed, with the Reynolds stress going to zero long before reaching the free surface. B) As opposed to the rigid cylinders, where a clear two-region flow was observed, here we see what resembles two shear layers within the same profile: one created by the shear at the top of the plants, and a smaller, upside down, mixing layer created by local vertical gradients of obstructed area, due to the tree-like structure of the stems. C) If one wants to focus only in the canopy top shear layer, a different normalization,

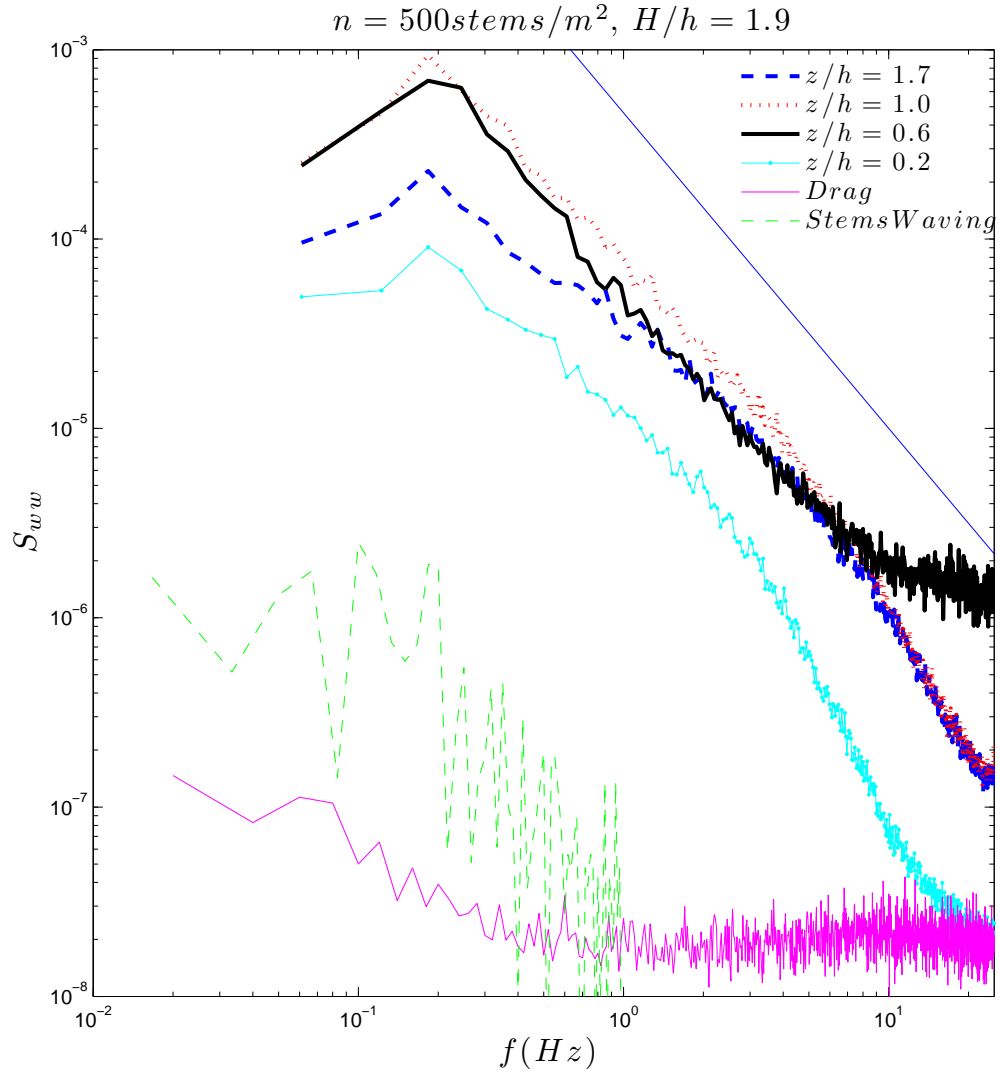


Figure 5.9: Spectra of vertical velocity at four vertical locations: upper shear layer (dashed line), top of the array (dotted line), and within the canopy at the denser (solid line) and less dense, near bottom region (dot-dash line). Solid line indicates the $-5/3$ inertial range. Thin solid line represents the frequency spectra from the measured drag, and thin dashed line shows the weaving frequency of the stems.

based on the self-similarity of mixing layers, should be used to collapse all the non-dimensional profiles around the exchange zone (Ghisalberti and Nepf, 2004).

Two approaches are used for normalization in the emergent case: the first one using U_Q , to be consistent with the experiments on cylinders (Figure 5.11), and the second using the maximum velocity within the canopy (u_M), which performs better at collapsing all data into a single curve (Figure 5.12). The transition from the emergent to submerged regime is evident in Figure 5.12, noticing that a) the near bottom, within-canopy, mixing layer structure, also noticed in the fully emergent case, remains unchanged as the stems bend, b) for fully emergent vegetation, the relative magnitude of the kinetic energy $\langle \bar{k} \rangle / u_M^2$ is similar to the levels reported for rigid cylinders, while Reynolds stress levels, $\langle \overline{u'w'} \rangle / u_M^2$, are now larger, c) as the flow transitions to nearly emergent, both values reach a maximum nearly an order of magnitude larger than their fully submerged counterparts.

Figure 5.13 shows the measured drags, averaged over the 7 lateral runs, as a function of flow rate. The range of flow rates studied had to be reduced with respect to the rigid case to avoid damage to the stems. Comparing Figure 5.13 (flexible plants) to Figure 4.31 (rigid cylinders), we notice that: A) the $n = 500 \text{ stems}/m^2$ series, having similar values of a as the rigid cylinders experiments (see Table 5.1) yields drag values of the same order as the rigid arrays for similar flow rates, and B) for each n , instead of a clear quadratic growth $D \sim Q^2$, we observe an almost linear behavior, assumed to be caused by the reduction in frontal area as the plants start bending.

We start our analysis by using two approaches to define a bulk drag coefficient C_{DB} (Eq. 5.1 and 5.2). A first bulk drag coefficient, C_{DB1} is defined based on the total obstructed area from stems on the drag plate, A_{fh} (m^2), and a depth averaged velocity, U_h (from the bottom to the top of the canopy). A second coefficient, C_{DB2} , is defined based on the z -dependent values of $A_f(z)U(z)^2$.

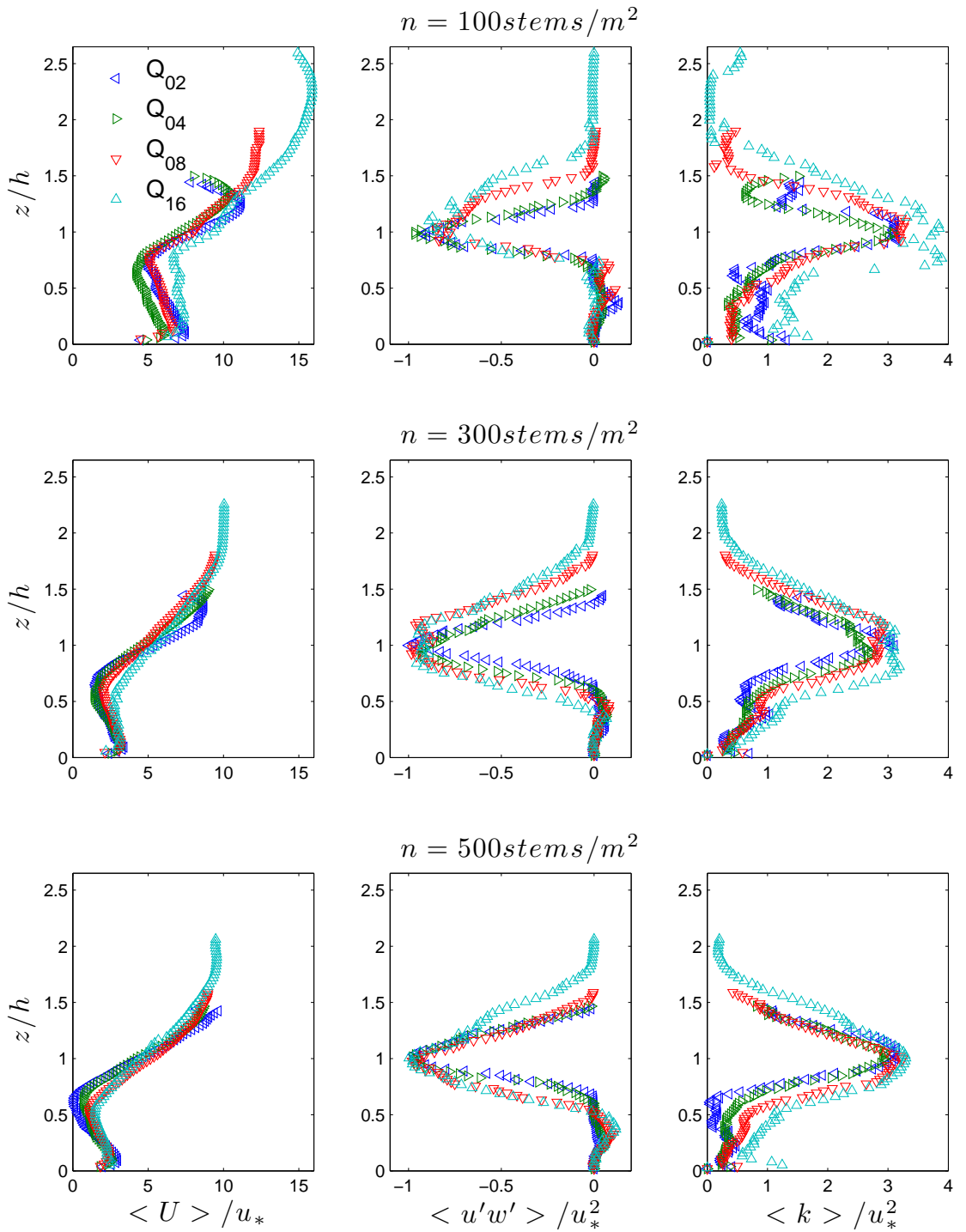


Figure 5.10: Normalized, horizontally averaged vertical profiles U/u_* , $\langle k \rangle / u_*^2$, and $\langle u'w' \rangle / u_*^2$, for $H = 0.37\text{m}$, with $u_*^2 = -\langle u'w' \rangle|_{z=h}$, for all flow rates studied, at each plant density, $n = 100, 300, 500 \text{ stems/m}^2$.

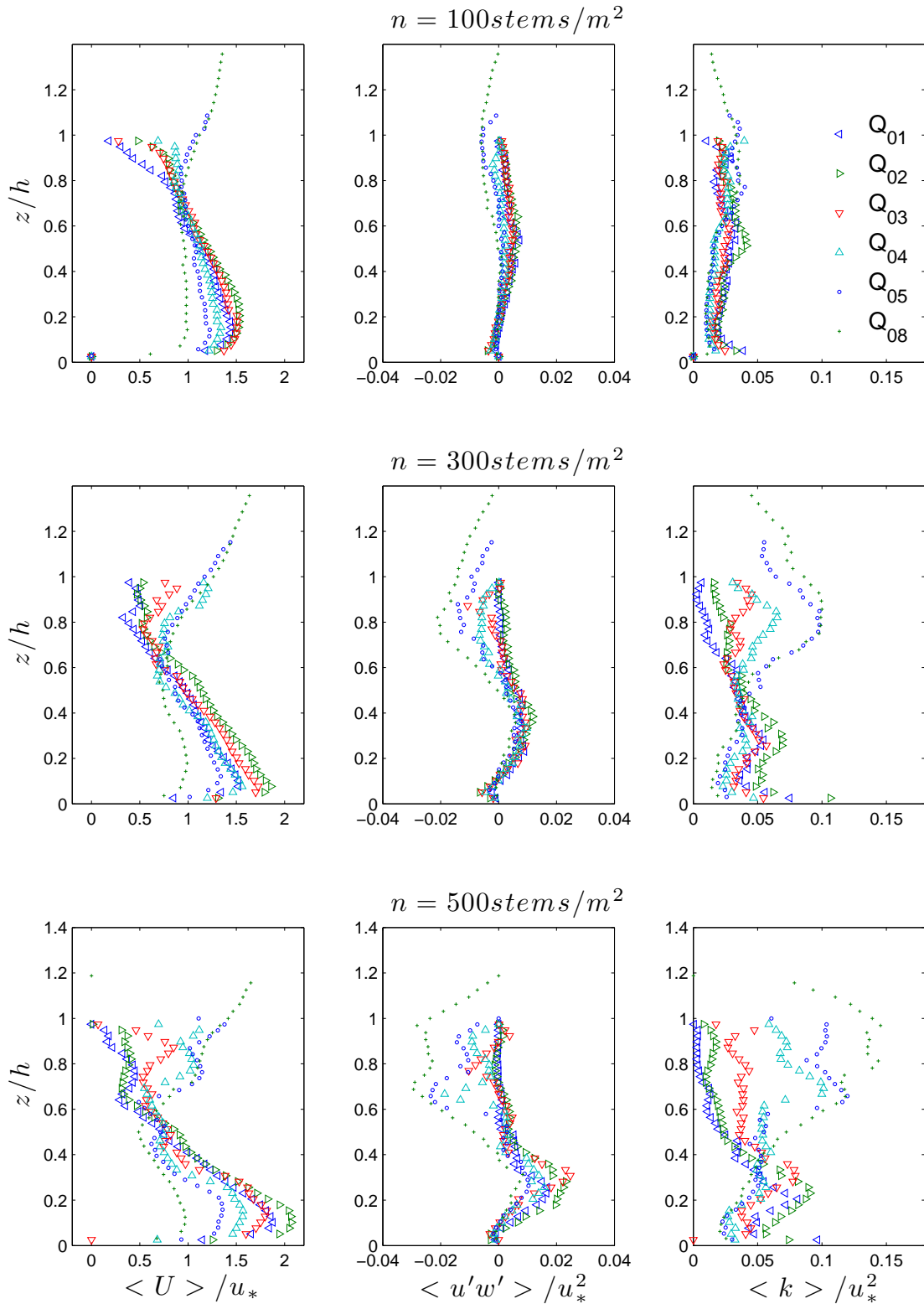


Figure 5.11: Normalized, horizontally averaged vertical profiles U/u_* , $\langle k \rangle / u_*^2$, and $\langle u'w' \rangle / u_*^2$, for $H = 0.20\text{m}$, with $u_* = U_Q$, for all flow rates studied, at each plant density, $n = 100, 300, 500 \text{ stems/m}^2$.

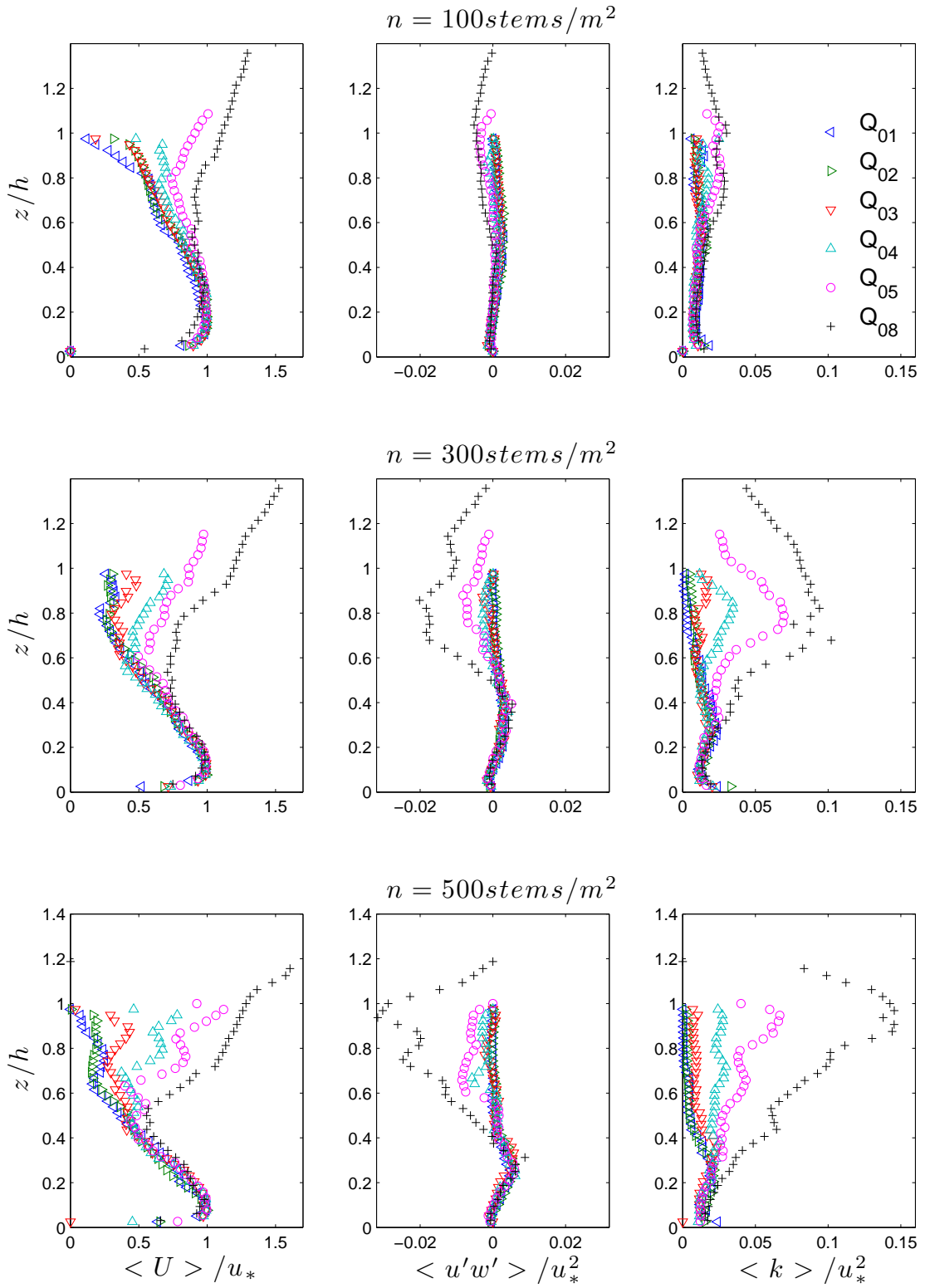


Figure 5.12: Normalized, horizontally averaged vertical profiles U/u_* , $\langle k \rangle / u_*^2$, and $\langle u'w' \rangle / u_*^2$, for $H = 0.20m$, with u_* taken as the maximum velocity within the plants, for all flow rates studied, at each plant density, $n = 100, 300, 500 \text{ stems}/m^2$.

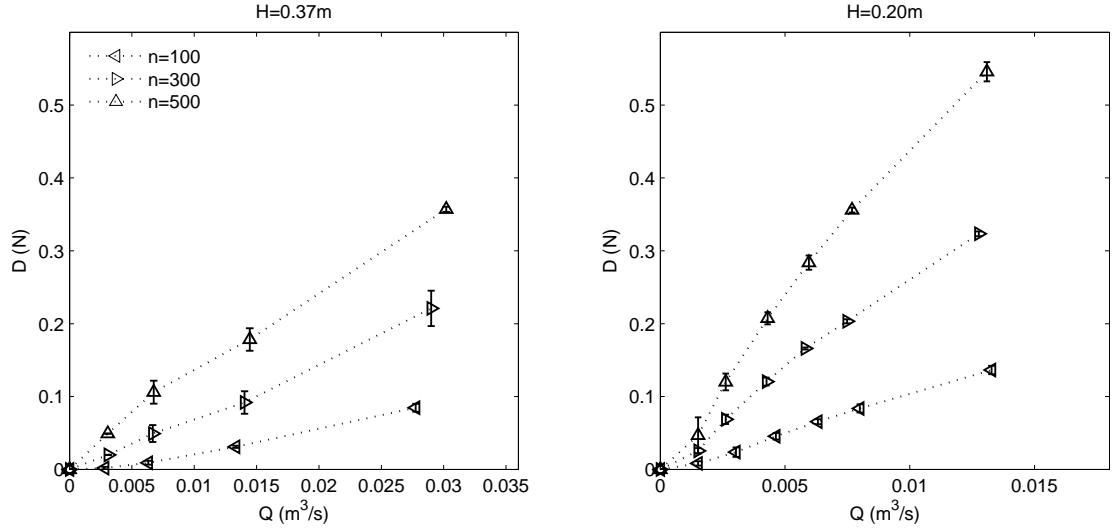


Figure 5.13: Measured drag as function of Q . Presented values averaged from 7 runs. Vertical bars for 95CI.

$$D = \frac{1}{2}\rho C_{dB1}(A_{fh})(U_h)^2 \quad (5.1)$$

$$D = \frac{1}{2}\rho C_{dB2} \int_0^h A_f(z) U(z)^2 dz \quad (5.2)$$

To be consistent with the previous analysis on rigid elements, the calculated values of C_{dB1} and C_{dB2} are plotted against a Reynolds number based on an effective diameter, $Re_{de} = U_h d_{eh} / \nu$, where we define $d_e = a/n$, from the simplified definition of $a = nd$ for rigid cylinders. Since d_e for real plants varies with depth, a depth averaged value, d_{eh} , is used. Results are shown in Figure 5.14. Both coefficients, with the exception of the least dense case ($n = 100 \text{ stems/m}^2$) at $H = 0.37m$, present a rapid decrease up to $Re_{de} = 300$, asymptotically towards a seemingly constant value around $C_{dB} \simeq 1.9$.

The non dimensional parameter used for rigid cylinders, C_{dad} , is here modified with a depth averaged a_h , and the effective diameter d_e , as $C_{dB} a_h d_e$. As it appears in Figure 5.15, the $H = 0.20m$ experiments present larger values for denser arrays

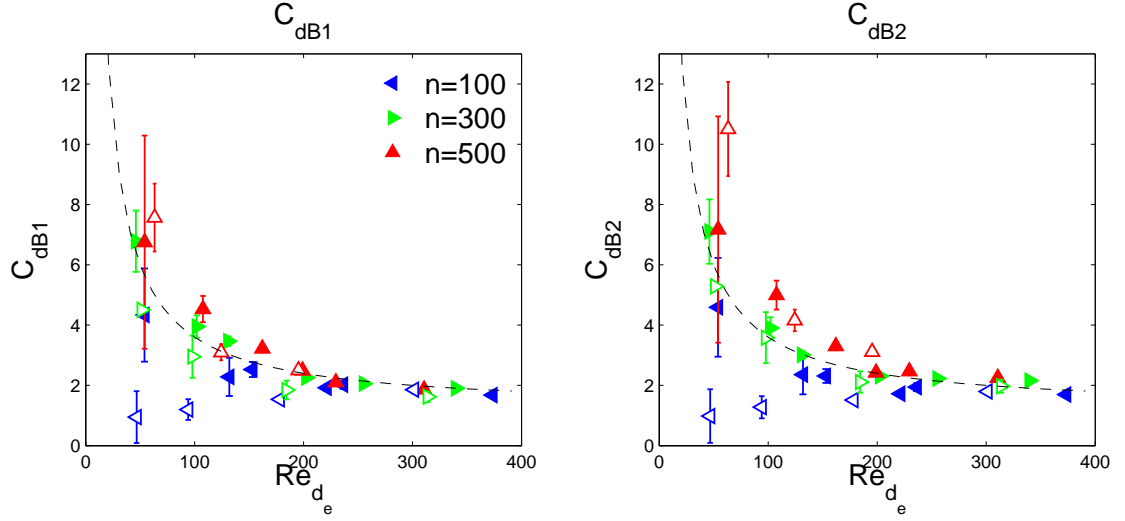


Figure 5.14: Bulk drag coefficients C_{dB1} and C_{dB2} , as defined in Eq. 5.1 and 5.2, for $H = 0.37m$ (open symbols) and $H = 0.20m$ (solid symbols). Vertical bars for 95CI. Dashed line for Ergun's equation fit, $\alpha_1 = 0.6$, $\alpha_0 = 70$.

(larger ϕ). Data from each case do not present the clear trend noticed in the rigid case, and the now shorter range of Re_{de} does not allow us to estimate a function $C_{dad} = C_{dad}(\phi)$ as with previous results.

In order to use Ergun's equation parameters α_0 , and α_1 , found from our experiments in rigid cylinders, to predict drag coefficients in real plants, we need to: 1) estimate the volume occupied by the plants, according to the linear relationship found in Figure 2.6 as a function of a ($V_{plants}(cm^3) = 3.5 \times 10^4 a(cm^{-1})$), 2) use the calculated volume to find the respective solid volume fraction, $\phi = V_{plants}/V_{fluid}$; and 3) use the appropriate α parameters (Table 4.3) for each calculated ϕ to calculate C_d . Values of solid volume fraction for plants are quite low ($\phi = \{0.0004 - 0.0022\}$ and $\phi = \{0.0005 - 0.0034\}$ for submerged and emergent plants, respectively) compared to the rigid cylinders studied ($\phi = \{0.005 - 0.080\}$). We use the α values from the lowest ϕ ($\phi = 0.005$, $\alpha_1 = 0.6$, $\alpha_0 = 70$) and get estimates for C_{dahde} (Eq. 5.3).

$$C_d a_h d_e = 2 \left(0.60 + \frac{70}{Re_d} \right) \frac{a_h^2}{n} \quad (5.3)$$

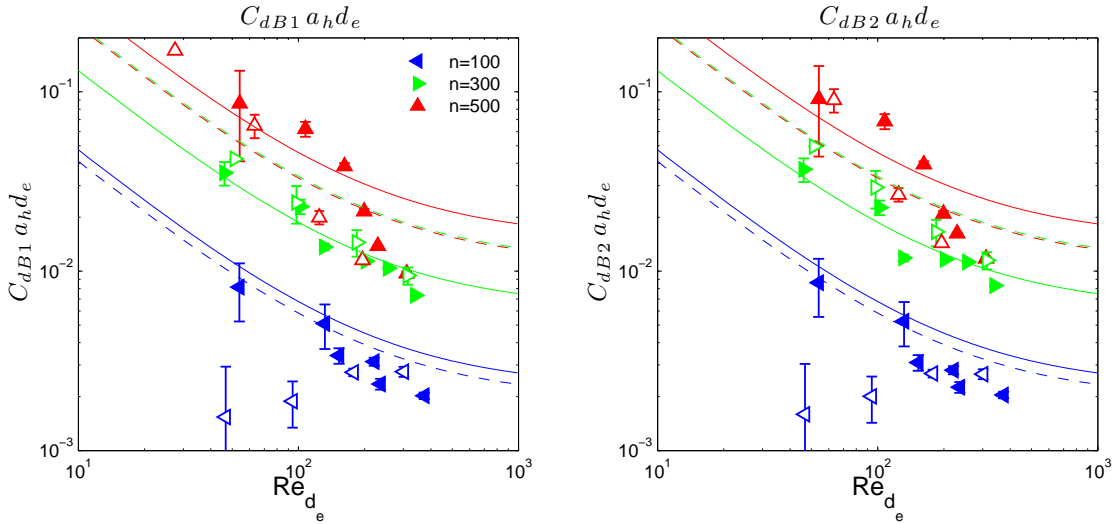


Figure 5.15: Measured and estimated values of $C_{dB1} a_h d_e$ and $C_{dB2} a_h d_e$, for $H = 0.37m$ (open symbols, dashed lines) and $H = 0.20m$ (solid symbols, solid line). Vertical bars for 95CI.

The estimated values, using a constant $a_h(n, Q = 0)$ throughout each series, show a good agreement with the measured values, performing better for the emergent ($H = 0.20m$) case, as shown in Figure 5.15. Using the measured a for each particular experiment, the match between predicted and measured values improves, as shown in Figure 5.16, where the ratio of measured to estimated $C_d a_h d_e$ values is presented, with most values falling between a $\pm 20\%$ margin, getting better for larger Re_{d_e} .

Since we are using the same α values for all cases, we can assume that at this lower range of ϕ , the dependence $C_d = C_d(\phi)$ is either minimal, or being indirectly accounted for by using Re_{d_e} from $d_e = a/n$, and a single fit for all flexible experiments can be found from the C_{dB} data, with $\alpha_1 = 0.6$, $\alpha_0 = 70$

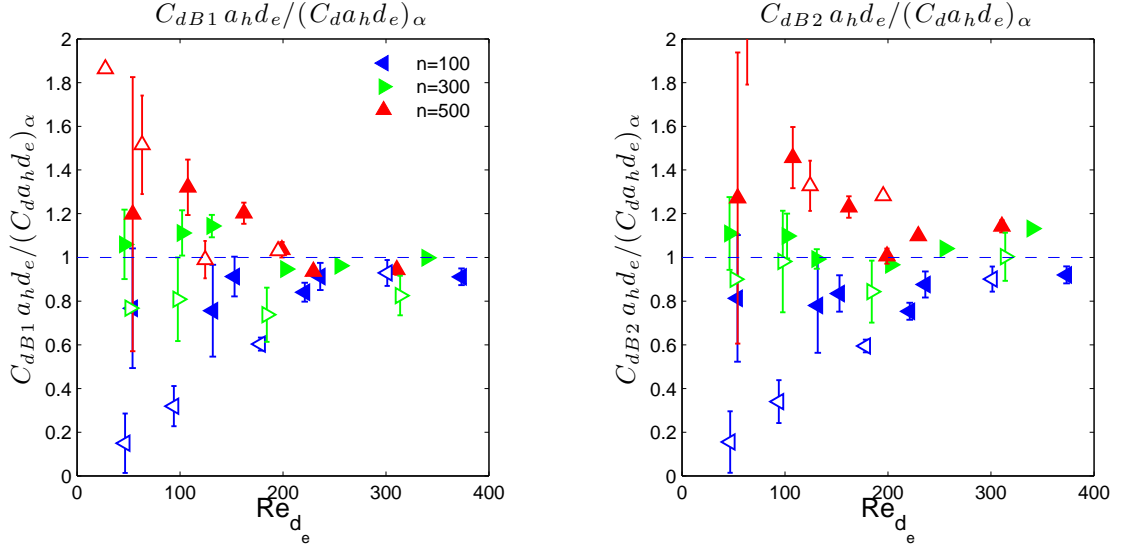


Figure 5.16: Measured to estimated ratios for $C_{dB1}a_h d_e$ and $C_{dB2}a_h d_e$, for $H = 0.37m$ (open symbols) and $H = 0.20m$ (solid symbols). Vertical bars for 95CI.

(Figure 5.14). If we compare the measured and estimated C_d values, we get the exact same ratios as shown in Figure 5.16. With the observed fit for the results from the bulk drag coefficient C_{dB1} , we can now get local drag coefficients, $C_d(z)$, as a function of $U(z)$ and $a(z)$ (Figure 5.17).

The vertical profiles of C_d (Figure 5.17) for all cases coincide in a clear decrease as the flow rate increases, with more uniform values for large a . Since we know $C_d(z)$, we can estimate the vertical profiles of the drag force per unit fluid mass: $f_{1e}(z) = \frac{1}{2}C_d(z)a(z)U(z)^2$ (Figure 5.18).

To compare against the measured drag per unit fluid mass, $f_{1m} = \frac{D}{\rho V}$, where ρ is the fluid density, and $V = A_{dp}h_p$, with A_{dp} being the area of the drag plate, we average the f_{1e} profiles over depth, and calculate the ratio between measured and estimated values of f_1 (Figure 5.19, left). The estimated C_d values seem to mostly underestimate drag for the slowest flows ($Re_{d_e} < 200$), while the agreement between both quantities improves as Re_{d_e} increases. It is observed that for $Re_{d_e} < 200$ the deviation between measured and predicted values is correlated with n ,

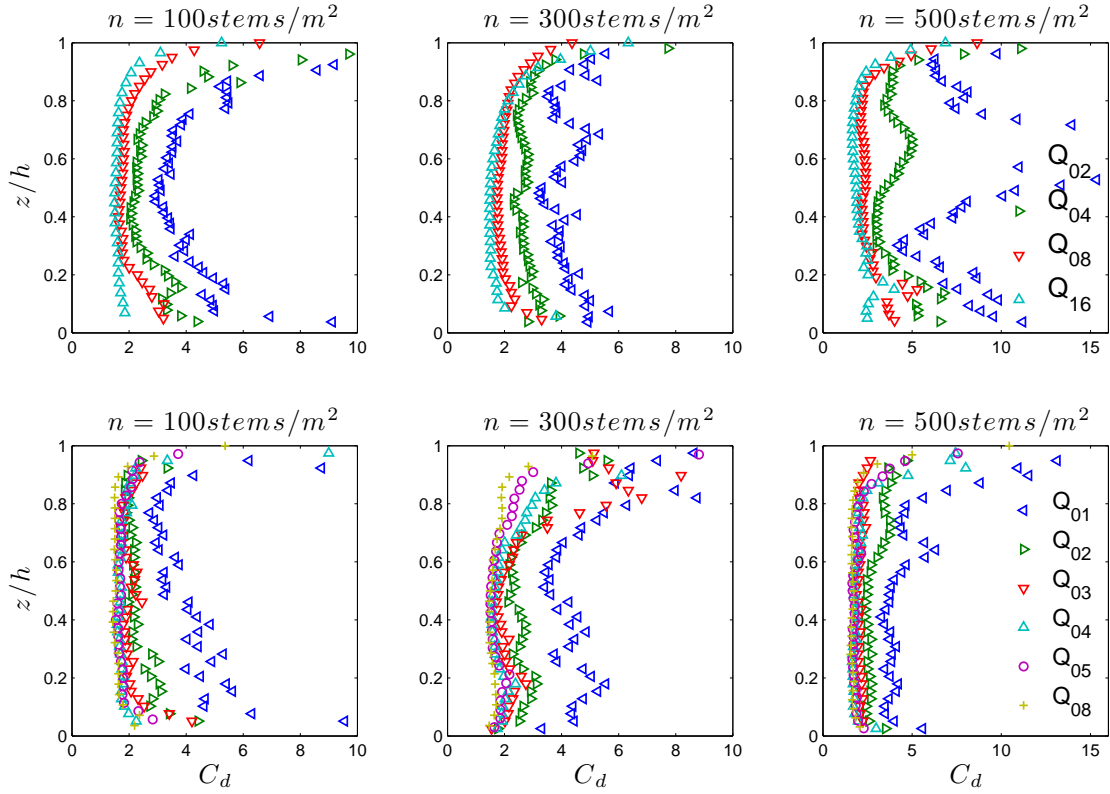


Figure 5.17: Predicted $C_d(z)$ values for $H = 0.37\text{m}$ (top row) and $H = 0.20\text{m}$ (bottom row).

noticed to a larger degree in the submerged case. Estimated values of drag using our approach outperform the assumption of a constant $C_d = 1.0$ (Figure 5.19, right).

In summary, we found a good agreement between the measured drag coefficients and the values estimated from a methodology based on rigid cylinders results. The process followed to calculate drag coefficients can be extended to other laboratory and field studies, as outlined below.

For laboratory experiments, we can measure the frontal area and the volume of the plants to estimate the solid volume fraction, or use empirical curves of volume vs. frontal area (e.g., 2.6) to estimate ϕ , and move onto step 5. If we only have data from macrophyte surveys, the following steps are proposed:

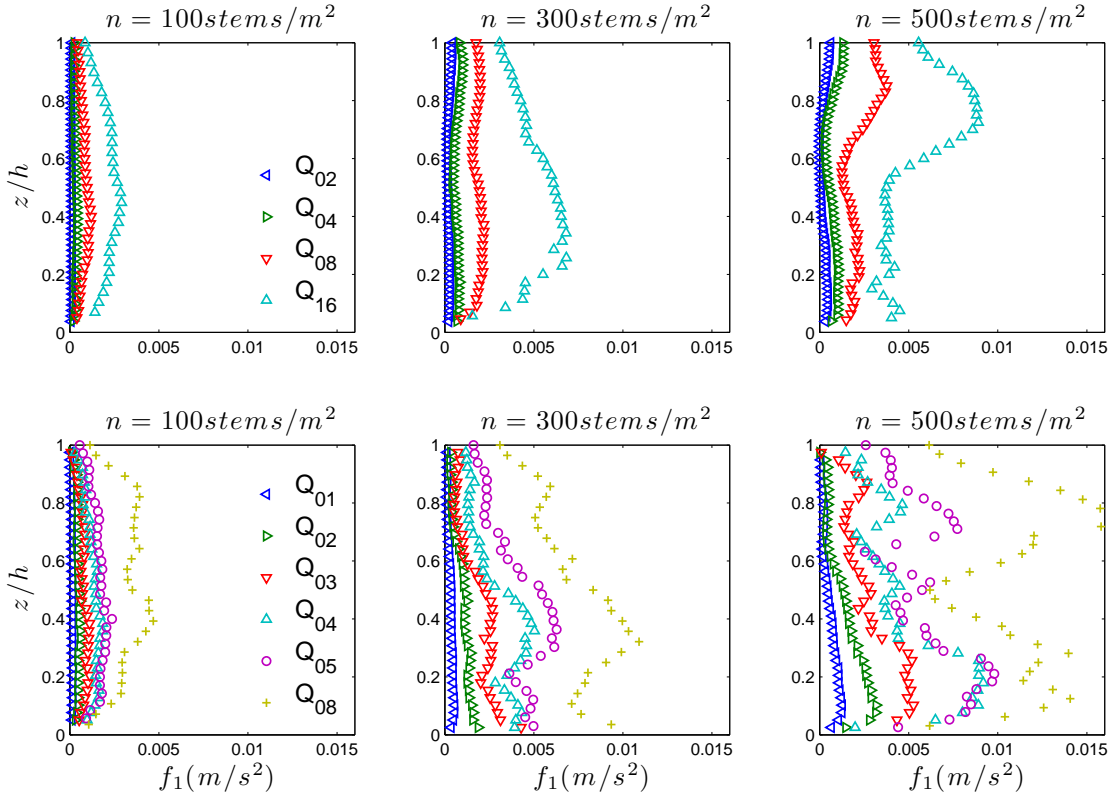


Figure 5.18: Vertical profiles of predicted values of drag force per unit fluid mass for $H = 0.37m$ (top row) and $H = 0.20m$ (bottom row).

1. Using biomass values and species composition from field surveys, we estimate the biomass corresponding to the species of interest.
2. Using empirical curves of biomass vs frontal area for a particular species (e.g., Figure 2.7), one can estimate the total frontal area per unit volume.
3. Using curves of volume vs frontal area (2.6), the volume occupied by the plants, and thus solid volume fraction ϕ , can be estimated.
4. For a more detailed analysis, to obtain height dependent drag coefficients, with the estimated total a , and knowing the mean length of the stems, we can estimate how the total area a is distributed along the water column from typical vertical profiles of $a(z)$ (Figure 2.7).
5. The coefficients α_0 and α_1 are chosen according to the estimated ϕ (Table

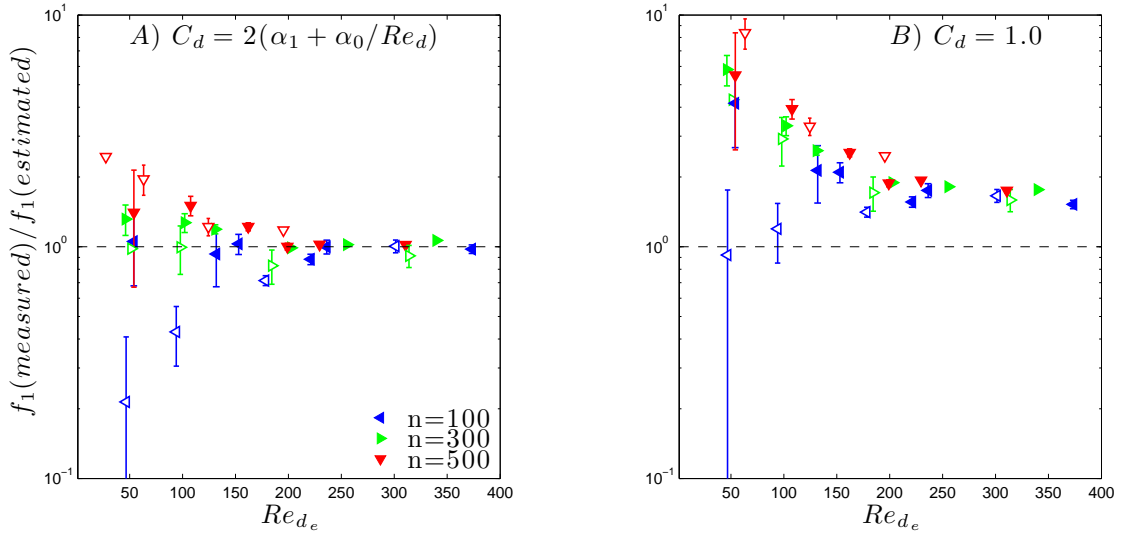


Figure 5.19: Ratio of measured to estimated f_1 , using the calculated $C_d(z)$ (left), and assuming a constant $C_d = 1.0$ (right), for $H = 0.37m$ (open symbols) and $H = 0.20m$ (solid symbols). Vertical bars for 95CI.

4.3).

6. Using Eq. 4.6, we predict the values of C_d .

The *a priori* determination of C_d not only will allow us to know the expected drag on canopies of real vegetation, it will help us to predict the penetration depth of large, mixing layer-scale eddies into submerged canopies, which control mass and momentum exchange (Nepf and Ghisalberti, 2008); C_d can be used to estimate the turbulent kinetic energy, which in turn is used to calculate longitudinal dispersion (Lightbody and Nepf, 2006), turbulent diffusion coefficients and lateral dispersion in random arrays (Tanino and Nepf, 2008b) to describe nutrient and pollutant transport in plant canopies; it allows calculation of how turbulent kinetic energy is being distributed along the water column, detecting the more energetic and turbulent regions of the canopy directly affecting organisms living within; and overall allows for more accurate predictions of velocity profiles, indispensable for restoration efforts in streams and coastal regions, as well as to determine how vegetated regions help mitigate the impacts of storms and tsunamis on coastal regions

(Kathiresan and Rajendran, 2005; Kerr et al., 2006; Vermaat and Thampanya, 2006).

5.3.4 Analysis of momentum and the budget

We investigate the relevance of each term in the simplified, temporally- and horizontally-averaged, z -dependent momentum equation (Eq. 5.4).

$$\begin{aligned}
 0 &= -W \frac{\partial \langle \bar{u} \rangle}{\partial z} - gS - \frac{\partial \langle \bar{u}'w' \rangle}{\partial z} + \nu \frac{\partial^2 \langle \bar{u} \rangle}{\partial z^2} - \frac{1}{2} C_d a U^2 \\
 0 &= I + II + III + IV + V
 \end{aligned} \tag{5.4}$$

In Figure 5.20 we present the momentum budget terms for the $H = 0.39m$ case, at low (left column) and high (right column) flow rates. Similar results for the $H = 0.20m$ series are presented in Figure 5.21. All temporally- and horizontally-averaged vertical profiles are obtained by averaging over the x -direction from PIV data, and then averaging over the seven transverse, y -sections studied. Vertical profiles of drag coefficients are estimated from Eq. 5.5.

$$C_d(z) a(z) d_e(z) = 2 \left(0.60 + \frac{70}{Re_{d_e}(z)} \right) \frac{a(z)^2}{n} \tag{5.5}$$

For the emergent case, there is a clear balance between only the pressure and drag terms (II and V), where the estimated C_d values perform successfully at balancing the momentum budget.

A more complex scenario is noticed for submerged vegetation. The viscous term (IV) is still negligible compared to the other contributions. The advective term (I) now appears of the same order as the Reynolds stress gradient (III).

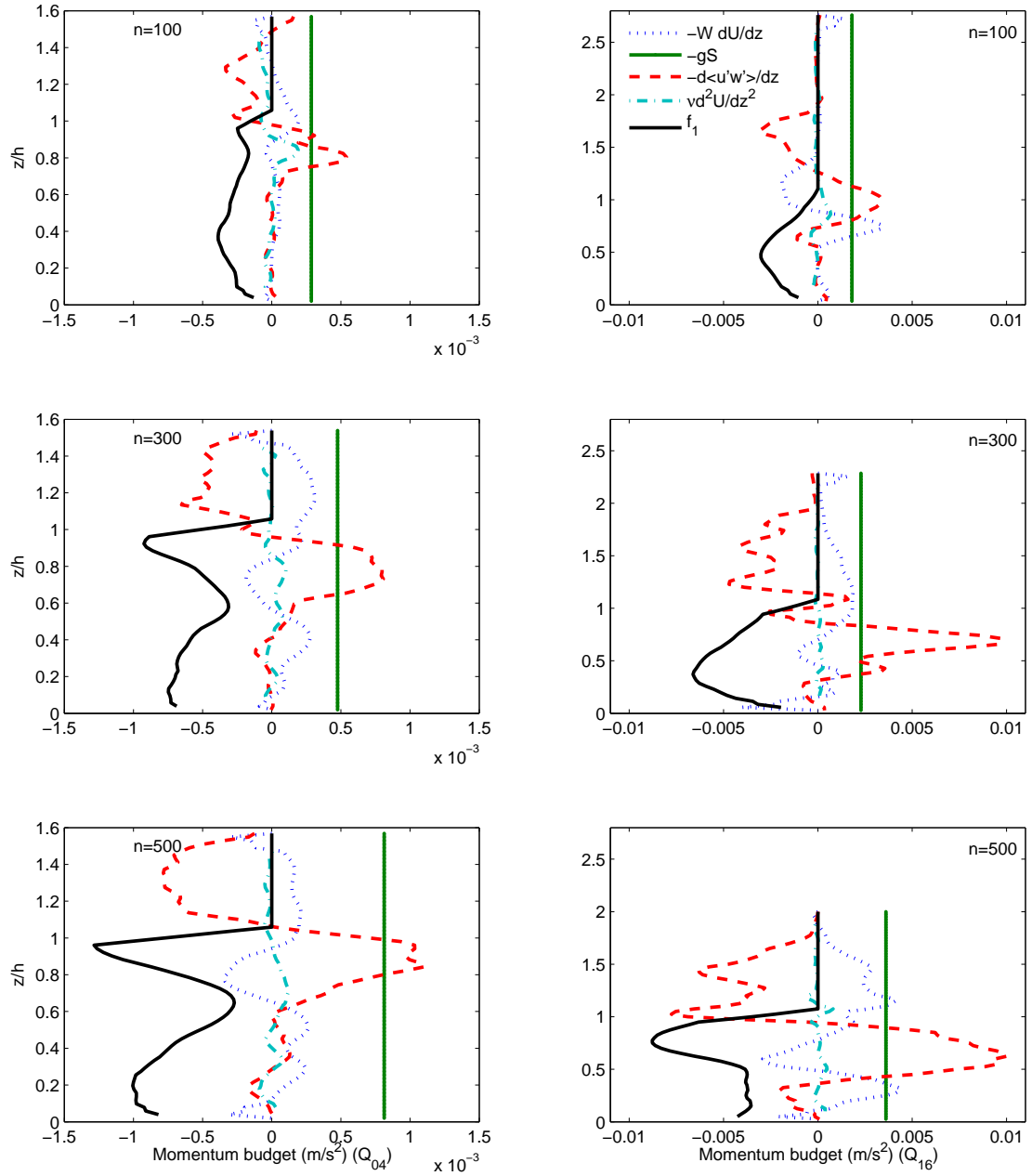


Figure 5.20: Momentum budget terms (Eq. 5.4) for all plant densities, $n = \{100, 300, 500\} \text{ stems/m}^2$ (top to bottom), for the $H = 0.37\text{m}$ case, for test Q_{04} , $Re_{d_e} = \{95, 100, 65\}$ (left column), and test Q_{16} , $Re_{d_e} = \{300, 315, 195\}$.

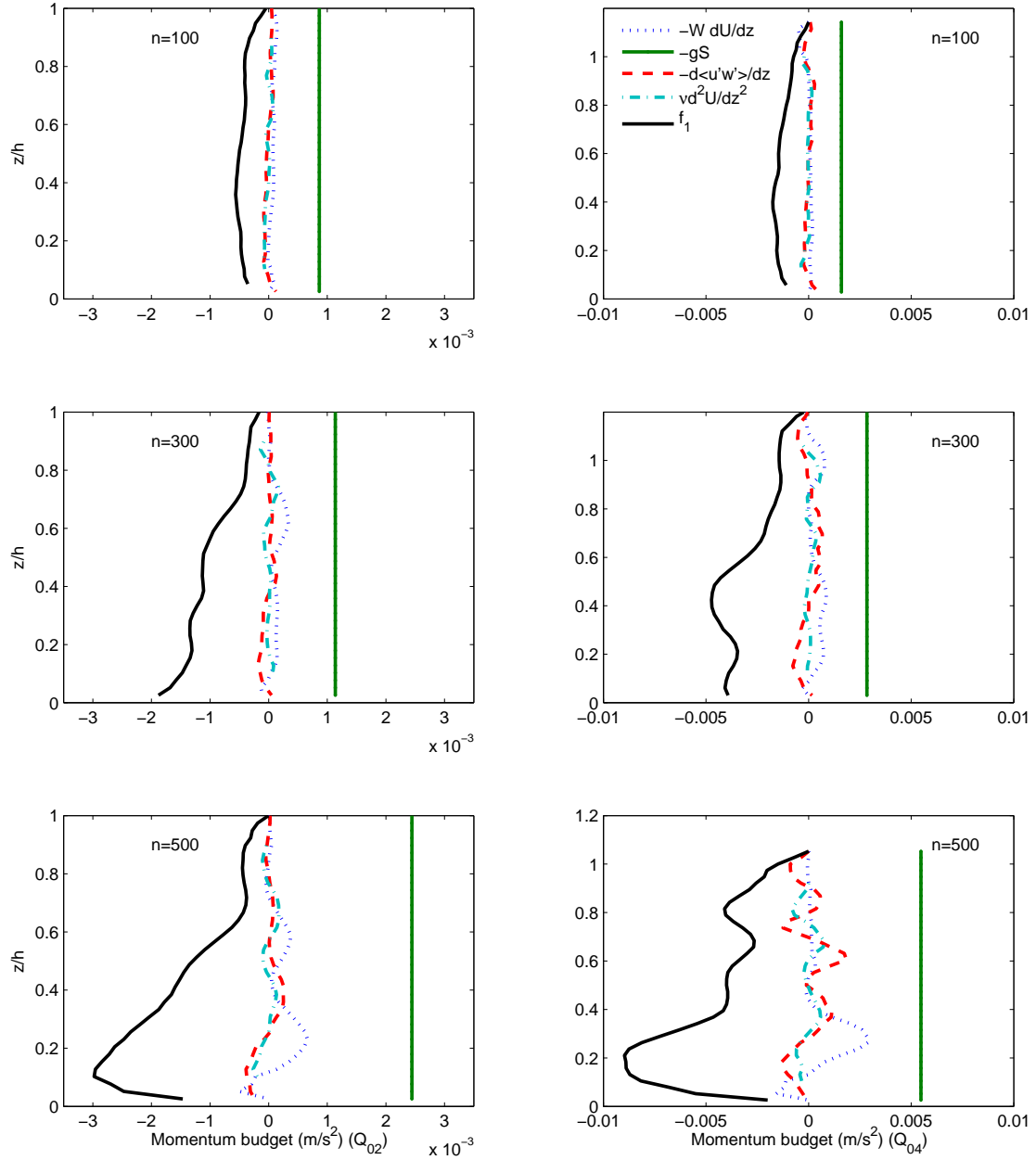


Figure 5.21: Momentum budget terms (Eq. 5.4) for all plant densities, $n = \{100, 300, 500\} \text{ stems/m}^2$, for fully emergent flow, Q_{02} , $Re_{d_e} = \{130, 100, 107\}$ (left column), and nearly emergent, Q_{04} , $Re_{d_e} = \{220, 200, 200\}$. $H = 0.20\text{m}$.

Analysis of the tke budget is conducted in an analogous manner to the rigid case. We use the second-order structure function, D_{LL} to estimate dissipation, ϵ_{DLL} , and compare it against the estimates for wake and shear dissipation, ϵ_w and ϵ_s . To calculate ϵ_w , we propose the use of the z -dependent effective diameter, defined as $d_e(z) = a(z)/n$, such that the vertical profile of dissipation is given as $\epsilon_w(z) = k(z)^{3/2}/d_e(z)$.

While we still see large variations in the calculated values, the results are consistent with the findings from rigid cylinders, with ϵ_w performing better far from the influence of shear, and following closely the shape of ϵ_{DLL} for the emergent case, while ϵ_s gives better estimates near the canopy top for the submersed case.

Using the same definitions from rigid arrays, each horizontally-averaged term of the tke budget is calculated as:

$$0 = T(z) + P_s(z) + P_w(z) - \epsilon(z) \quad (5.6)$$

$$P_s = -\langle \overline{u'w'} \rangle \frac{\partial U}{\partial z} \quad (5.7)$$

$$P_w = \frac{1}{2} a C_d U^2 |U| \quad (5.8)$$

$$T = \frac{\partial}{\partial z} \left[\nu_t \frac{\partial k}{\partial z} \right] \quad (5.9)$$

For the submersed experiments the balance between ϵ and P_w is still maintained in the wake zone, with contributions from turbulent transport and shear production around the top of the canopy.

For the emergent case, since we noticed very low values of dissipation ϵ_{DLL} for the $n = 100$ series (Figure 5.23), we include both ϵ_{DLL} and the estimated ϵ_w values in Figure 5.25. It appears that shear production and turbulent transport are damped, leading to a balance between wake production and dissipation. As

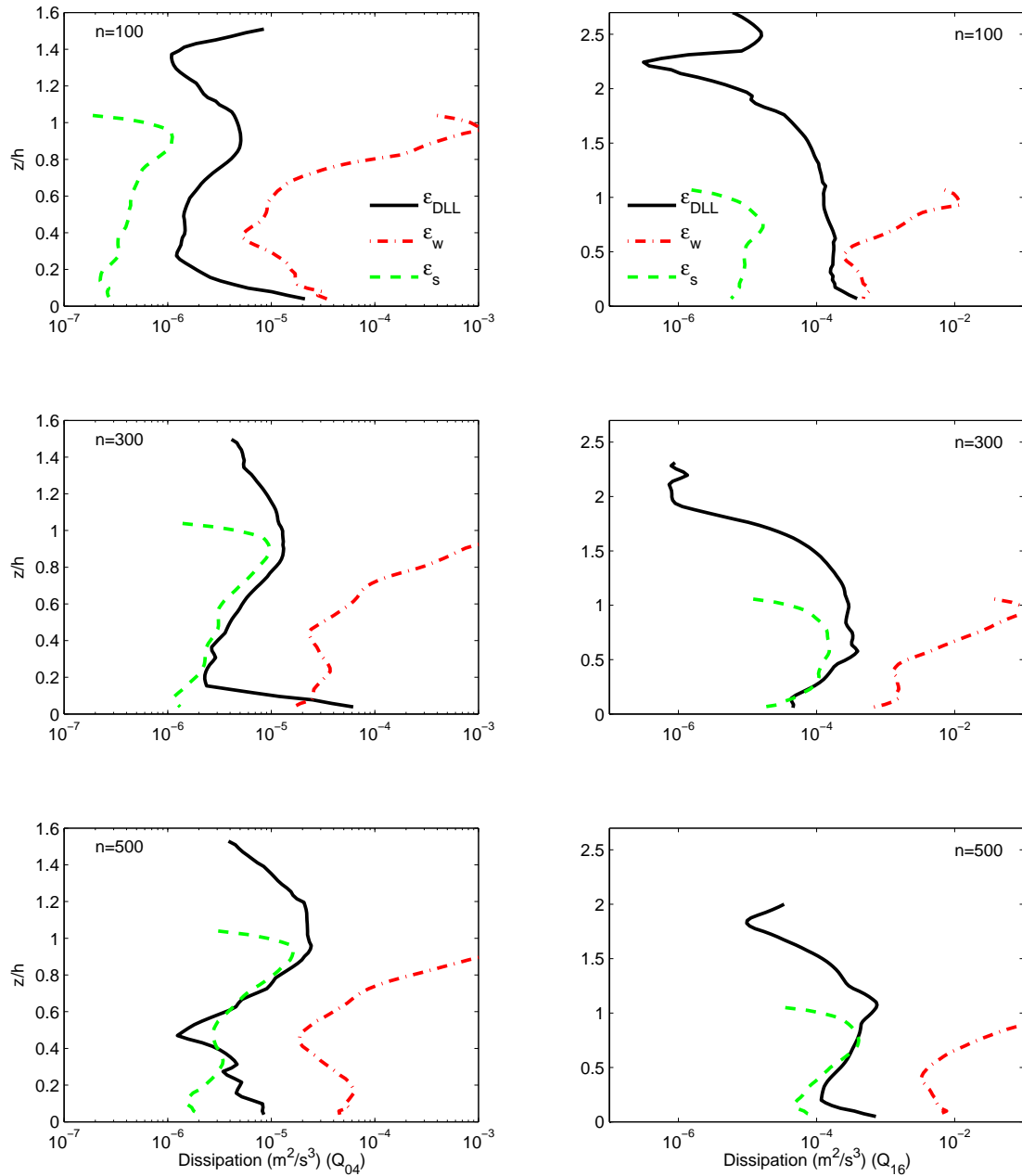


Figure 5.22: Dissipation values from the second order structure function, ϵ_{DLL} (solid line), compared against the estimates ϵ_s (dashed line) and ϵ_w (dot-dashed line), assumed to be only valid in the shear and wake regions respectively, for all plant densities, $n = \{100, 300, 500\}$ stems/m², for test Q_{04} , $Re_{de} = \{95, 100, 65\}$ (left column) and Q_{16} , $Re_{de} = \{300, 315, 195\}$, for the $H = 0.37m$ case.

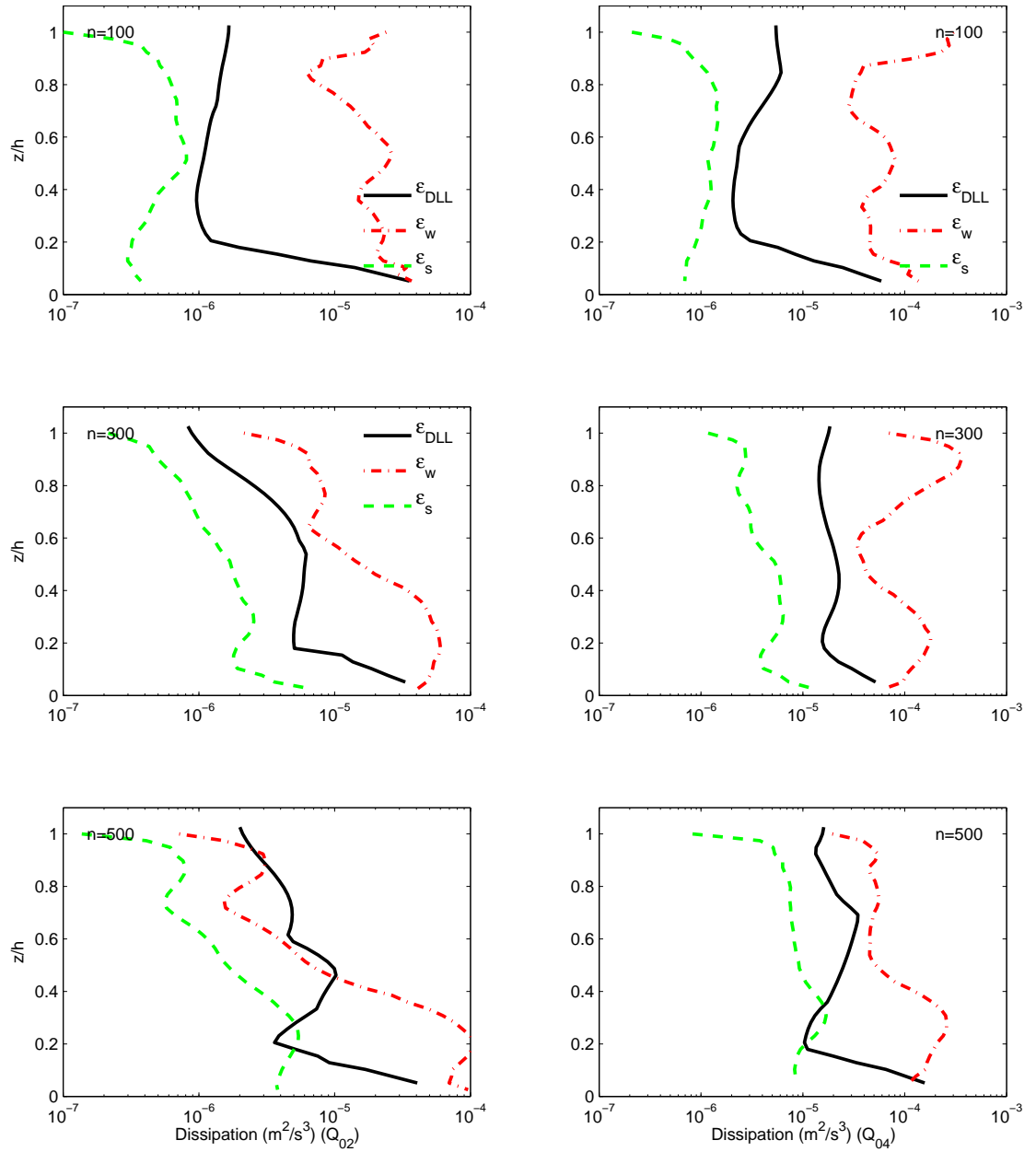


Figure 5.23: Dissipation values from the second order structure function, ϵ_{DLL} (positive x-axis), compared against the estimates ϵ_s and ϵ_w (negative x-axis), assumed to be valid in the shear and wake regions respectively, for all plant densities, $n = \{100, 300, 500\} stems/m^2$, for the fully emergent flow, Q_{02} , $Re_{de} = \{130, 100, 107\}$ (left column), and nearly emergent, test Q_{04} , $Re_{de} = \{220, 200, 200\}$. $H = 0.20m$.

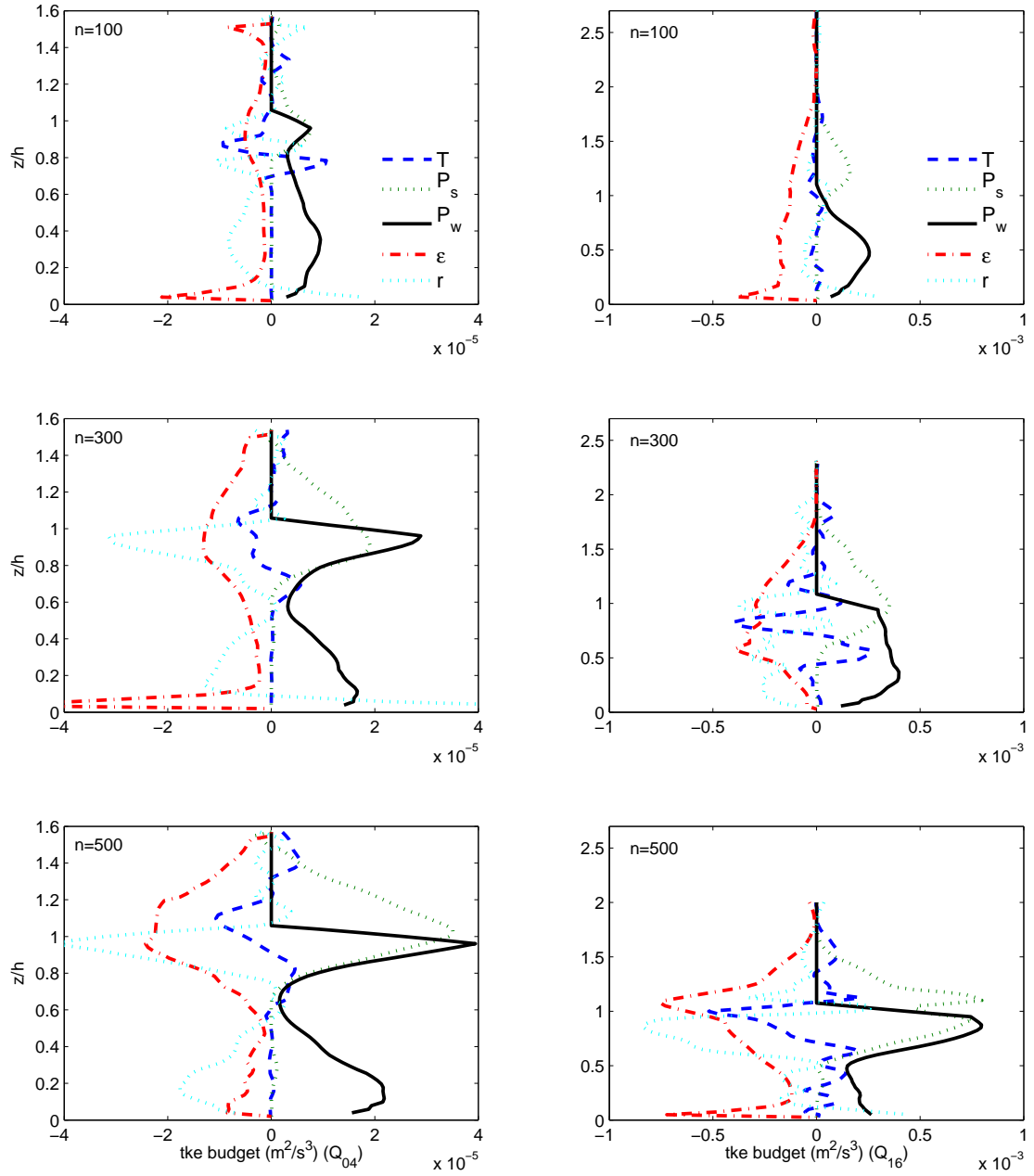


Figure 5.24: tke budget terms (Eq. 5.6) for all plant densities, $n = \{100, 300, 500\}$ stems/m² (top to bottom), for the $H = 0.37m$ case, for test Q_{04} , $Re_{de} = \{95, 100, 65\}$ (left column), and test Q_{16} , $Re_{de} = \{300, 315, 195\}$.

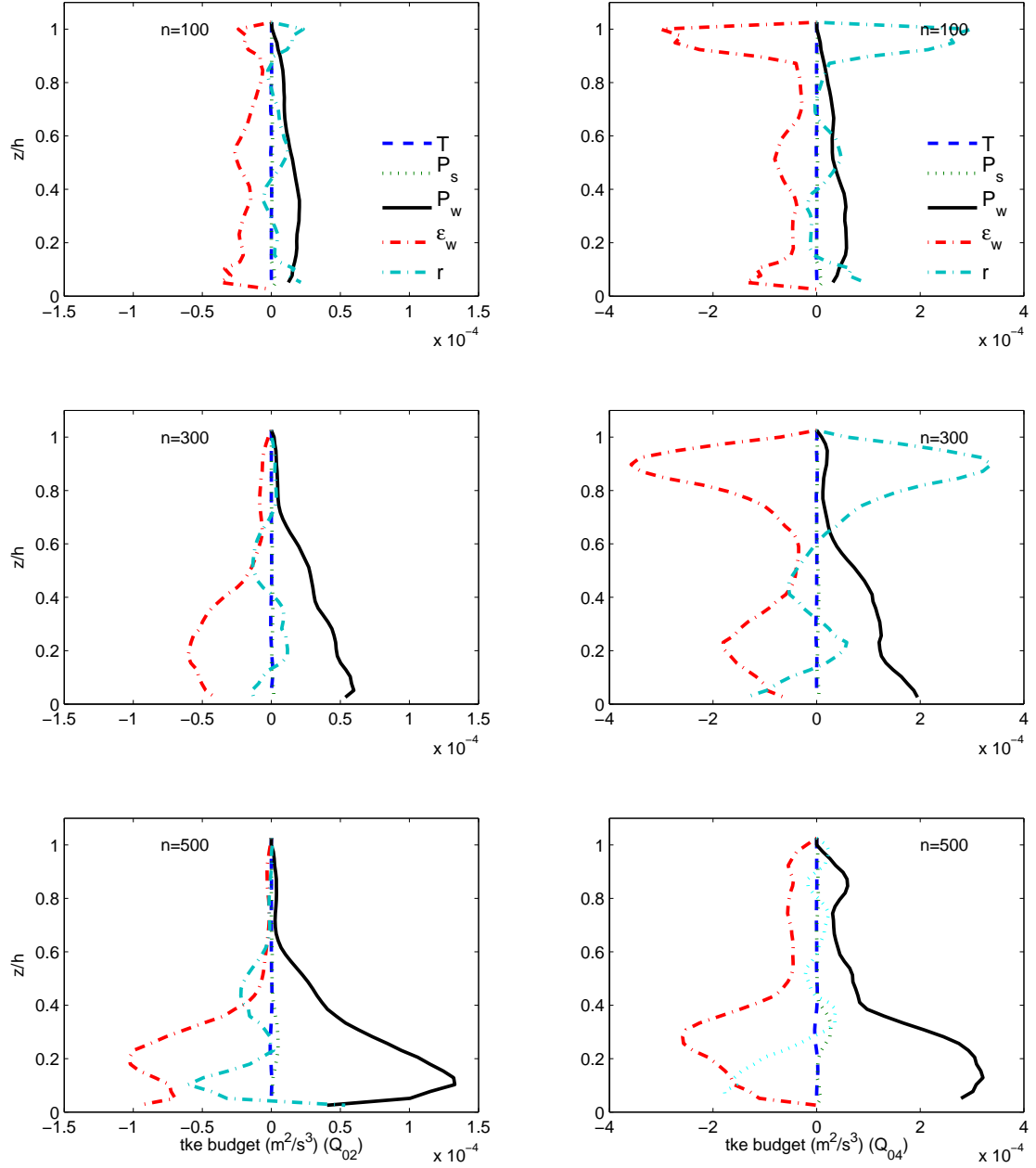


Figure 5.25: tke budget terms (Eq. 5.6) for all plant densities, $n = \{100, 300, 500\}$ stems/m², for fully emergent flow, Q_{02} , $Re_{de} = \{130, 100, 107\}$ (left column), and nearly emergent, Q_{04} , $Re_{de} = \{220, 200, 200\}$. $H = 0.20m$.

it appears in Figure 5.25, as we increase the number of plants, we start over predicting wake production P_w . One must recall that the way we defined P_w (Eq. 5.8), assumes that all energy extracted from the mean flow by canopy drag is turned into tke, which does not hold when the wakes are not fully turbulent (for $Re_d < 200$ in rigid cylinders (Nepf and Vivoni, 2000)), in which case our defined P_w becomes an upper limit.

5.4 Conclusions

We used a quantitative imaging methodology to successfully measure time series of vertical profiles of obstructed frontal area as a function of velocity, capturing in detail the height reduction and periodic oscillations of the stems. The recorded periodic motions match the frequency of the shear scale eddies, generated by the drag discontinuity at the top of the canopy.

Analysis of the velocity fields showed significant spatial variations due to both the local heterogeneity of the canopy and swaying of the plants. However, the robust spatial (horizontal) averaging scheme conducted, allowed us to obtain representative mean values of each parameter of interest.

As expected from previous results, the drag plate yields accurate measurements even for the sparsest arrays, at which other indirect methods, based on free surface measurements, begin to fail as the magnitude of the slope approaches uncertainty limits. The ability of the drag plate to measure vegetated drag is demonstrated, and the coupling of drag, measured frontal areas, and a detailed characterization of the velocity field gives us certainty in the measured drag coefficients.

Using the analysis conducted on results from rigid cylinders and introducing a length scale analogous to the rigid cylinders, an effective diameter $d_e = a/n$, we predict C_d values as a function of ϕ and Re_{d_e} . The predicted values are used to calculate the actual forces on the canopy, yielding a good match to the measured values, and outperforming the assumption of a constant, order one drag coefficient.

The success of the predicted C_d values leads us to propose a series of steps to predict drag coefficients for the field based on empirical curves relating frontal area, volume, and biomass of specific plant species.

Chapter 6

Conclusions

1. We have presented the development of a laboratory device, a drag plate, that outperforms similar attempts at directly measuring drag on aquatic vegetation, thanks to a) its ability to capture both mean values and instantaneous, high frequency drag variations, b) its sensitivity to small force variations, as demonstrated by the measurements in pure bottom stress, and the capture of periodic oscillations by wake generated waves, c) its dimensions, large enough to allow for averaging drag over multiple elements, d) its non-intrusive design, removing added stresses from submerged mounting frames, which at the same time facilitates an easy set up of any single or multiple structure study, regardless of shape or flexibility, e) the accessibility to all of its components, allowing easy adjustment or replacement of the load cell without dismounting the drag plate or perturbing the elements mounted above it, and f) its specific design to match existing test sections available in the open channel flumes and a wave tank in the DeFrees Hydraulics Laboratory at Cornell University.

2. We used the successfully tested drag plate, coupled in state of the art quantitative imaging techniques, to produce an extensive and unique data set, for four flow scenarios: flow through rigid, emergent cylinders; flow over submerged, rigid

cylinders; flow through flexible, live stems; and flow above live, flexible stems. Our data set provides a) representative spatially averaged values of the velocity field, b) velocity dependent profiles of obstructed area, c) detailed laterally averaged measurements of the free surface slope, d) bulk flow rates, and e) the measured total drag force for each test, a parameter rarely measured directly for vegetated flows. By using the same facilities and methodologies for all of the flow scenarios studied, we obtain a more robust, consistent data set, optimal for calibration of numerical models, such as the one by King and Cowen (2011).

3. Starting from a similar approach from previous laboratory (Tanino and Nepf, 2008a) and numerical works (Koch and Ladd, 1997), we investigate the dependence of drag coefficients on solid volume fraction and diameter based Reynolds number for arrays of rigid cylinders. We found a family of curves to predict C_d as a function of ϕ and Re_d . Our data suggests that such relationships are better represented by a parameter C_{dad} , instead of C_d alone, and in fact, plotting the C_{dad} curves as a function of Re_d for all the investigated values of ϕ yields a simpler, linear relationship to estimate drag coefficients at $Re_d > 1000$.

4. We used the C_{dad} curves, found from experiments on rigid cylinders, to predict vertical profiles of drag coefficients for the flows on live, flexible stems. To account for the plant morphology in the estimation of C_d , we introduced an additional length scale, analogous to the cylinder diameter, an effective stem diameter, defined as $d_e(z) = a(z)/n$, thus calculating C_d as a function of Re_{d_e} . We used the predicted drag coefficients to estimate the drag experienced by the canopy. The estimated values closely match the actual measurements except at the lowest Reynolds numbers, where the drag is largely underestimated. Those discrepancies are attributed to the sensitivity of the fitting parameters α_1 and α_0 , as well as the lack of data from lower densities $\phi < 0.005$.

6. The main objective to predict drag in complex canopy arrays is achieved,

and we propose an extended methodology presented here as a way to estimate vegetated drag in the field, using macrophyte surveys as a starting point. For such a method to perform satisfactorily, several representative species, according to their morphology, will have to be investigated to produce the required empirical relationships between biomass, frontal area, and plant volume.

BIBLIOGRAPHY

- Ackerman, J. (1997). Submarine pollination in the marine angiosperm *Zostera marina* (Zosteraceae). i. the influence of floral morphology on fluid flow. *American Journal of Botany*, 84(8):1099–110911.
- Ackerman, J. and Okubo, A. (1993). Reduced mixing in a marine macrophyte canopy. *Functional Ecology*, 7:305–309.
- Ackerman, J.D. and Hoover, T.M. (2001). Measurement of local bed shear stress in streams using a Preston-static tube. *Limnol. Oceanogr.*, 46(8):2080–2087.
- Aiken, S., Newroth, P. and Wile, I. (1979). The biology of Canadian weeds. 34. *Myriophyllum spicatum* L. *Can. J. Plant Sci.*, 59:201–215.
- Augustin, L., Irish, J. and Lynett, P. (2009). Laboratory and numerical studies of wave damping by emergent and near-emergent wetland vegetation. *Coast. Eng.*, 56:332–340.
- Baptist, M., Babovic, V., Rodriguez, J., Keijzer, M., Uittenbogaard, R., Mynett, A. and Verwey, A. (2007). On inducing equations for vegetation resistance. *Journal of Hydraulic Research*, 45(4):435–450.
- Barnes, M.P., O'Donoghue, T., Alsina, J. and Baldock, T.E. (2009). Direct bed shear stress measurements in bore-driven swash. *Coastal Engineering*, 56:853–867.
- Callaghan, F., Cooper, G., Nikora, V., Lamouroux, N., Statzner, B., Sagnes, P., Radford, J., Malet, E. and Biggs, B. (2007). A submersible device for measuring drag forces on aquatic plants and other organisms. *New Zealand Journal of Marine and Freshwater Research*, 41:119–127.

- Cowen, E. and Monismith, S. (1997). A hybrid digital particle tracking velocimetry technique. *Experiments in fluids*, 22:199–211.
- DeJong, J., Cao, L., Woodward, S., Salazar, J., Collins, L. and Meng, H. (2009). Dissipation rate estimation from piv in zero-mean isotropic turbulence. *Exp. Fluids*, 46:499–515.
- Doron, P., Bertuccioli, L., Katz, J. and Osborn, T. (2001). Turbulence characteristics and dissipation estimates in the coastal ocean bottom boundary layer from piv data. *Journal of Physical Oceanography*, 31:2108–2134.
- Dunn, C., Lopez, F. and Garcia, M. (1996). Mean flow and turbulence in a laboratory channel with simulated vegetation. Technical report, Hydraulic Engineering Series No. 51, UILU-ENG-96-2009.
- Efron, B. and Tibshirani, R. (1993). *An introduction to the bootstrap*. Chapman and Hall, London.
- Ergun, S. (1952). Fluid flow through packed columns. *Chem. Eng. Prog.*, 48(2):89–94.
- Fathi-Maghadam, M. and Kouwen, N. (1997). Nonrigid, nonsubmerged, vegetative roughness on floodplains. *Journal of Hydraulic Engineering*, 123:51–57.
- Fernholz, H., Janke, G., Schober, M., Wagner, P.M. and Warnack, D. (1996). New developments and applications of skin friction measuring techniques. *Measurement Science and Technology*, 7:1396–1409.
- Finnigan, J. (2000). Turbulence in plant canopies. *Annu. Rev. Fluid Mech.*, 32:519–571.

- Freeman, G.E., Rahmeyer, W.J. and Copeland, R.R. (2000). Determination of resistance due to shrubs and woody vegetation. Technical report, US Army Corps of Engineers.
- Ghisalberti, M. (2010). The three-dimensionality of obstructed shear flows. *Environ Fluid Mech*, 10:329–343.
- Ghisalberti, M. and Nepf, H. (2006). The structure of the shear layer in flows over rigid and flexible canopies. *Environmental Fluid Mechanics*, 6:277–301.
- Ghisalberti, M. and Nepf, H.M. (2004). The limited growth of vegetated shear layers. *Water Resources Research*, 40:1–12.
- Ghisalberti, M. and Nepf, H. (2002). Mixing layers and coherent structures in vegetated aquatic flows. *Journal of Geophysical Research*, 107.
- Ghomeshi, M., Mortazavi-Dorcheh, S. and Falconer, R. (2007). Amplitude of wave formation by vortex shedding in open channels. *J. of App. Sci.*, 7(24):3927–3934.
- Green, J. (2005b). Further comment on drag and reconfiguration of macrophytes. *Freshwater Biology*, 50:2162–2166.
- Gross, E., Johnson, R. and Hairston, N. (2001). Experimental evidence for changes in submersed macrophyte species composition caused by the herbivore acentria ephemera (lepidoptera). *Oecologia*, 127(1):105–114.
- Ikeda, S. and Kanazawa, M. (1996). Three-dimensional organized vortices above flexible water plants. *J. Hydraul. Eng.*, 122(11):634–640.
- Jadhav, R. and Buchberger, S. (1995). Effects of vegetation on flow through free water surface wetlands. *Ecological Engineering*, 5:481–496.

- Janauer, G. and Dokulil, M. (2006). *Macrophytes and algae in running waters*. John Wiley & Sons, Ltd.
- Jarvela, J. (2002). Flow resistance of flexible and stiff vegetation: a flume study with natural plants. *Journal of Hydrology*, 269:44–54.
- Johnson, R.L. (2008). *A field guide of aquatic plant species found in Chautauqua Lake along with potential exotic invaders*. Chautauqua Lake Association.
- Johnson, R.L., Gross, E.M. and Hairston, N.G. (1998). Decline of the invasive submersed macrophyte *Myriophyllum spicatum* (haloragaceae) associated with herbivory by larvae of *Acentria ephemerella* (lepidoptera). *Aquatic Ecology*, 31:273–282.
- Kathiresan, K. and Rajendran, N. (2005). Coastal mangrove forests mitigated tsunami. *Estuar. Coast. Shelf. Sci.*, 65:601–606.
- Kerr, A., Baird, A. and Campbell, S. (2006). Comments on "coastal mangrove forests mitigated tsunami". *Estuar. Coast. Shelf. Sci.*, 67:539–541.
- Khalak, A. and Williamson, C. (1996). Dynamics of a hydroelastic cylinder with very low mass and damping. *J. Fluids. Struct.*, 10:455–472.
- King, A. (2011). *Measuring and modeling mean flow, turbulence, and hydraulic residence time in shallow surface water systems occupied by submerged and emergent aquatic vegetation*. Ph.D. thesis, Cornell University.
- King, A. and Cowen, E. (2011). A $k-\epsilon$ turbulence model based on the scales of vertical shear and stem wakes valid for emergent and submerged vegetated flows. *J. Fluid Mech.*
- Kline, S. and McClintock, F. (1953). Describing uncertainties in single-sample experiments. *Mechanical Engineering*, 75:3–8.

- Koch, D. and Ladd, A. (1997). Moderate reynolds number flows through periodic and random arrays of aligned cylinders. *J. Fluid. Mech.*, 349:31–66.
- Koegel, R., Sy, S., Bruhn, H. and Livermore, D. (1973). Increasing the efficiency of aquatic plant management through processing. *Hyacinth Control J.*, 11:24–30.
- Kundu, P. and Cohen, I. (2004). *Fluid Mechanics*. Elsevier Academic Press.
- Lam, K., Li, J., Chan, K. and So, R. (2003). Flow pattern and velocity field distribution of cross-flow around four cylinders in a square configuration at a low reynolds number. *J. Fluid Struct.*, 17:665–679.
- Lightbody, A. and Nepf, H. (2006). Prediction of velocity profiles and longitudinal dispersion in emergent salt marsh vegetation. *Limnology and Oceanography*, 51(1):218–228.
- Lopez, F. and Garcia, M. (1997). Open-channel flow through simulated vegetation: Turbulence modeling and sediment transport. Technical report, Wetlands Research Program Technical Report WRP-CP-10.
- Lopez, F. and Garcia, M. (1998). Open-channel flow through simulated vegetation: Suspended sediment transport modeling. *Water Resources Research*, 34(9):2341–2352.
- Lopez, F. and Garcia, M. (2001). Mean flow and turbulence structure of open channel flow through non-emergent vegetation. *Journal of Hydraulic Engineering*, 127:392–402.
- Luhar, M., Rominger, J. and Nepf, H. (2008). Interaction between flow, transport and vegetation structure. *Environ Fluid Mech*, 8:423–439.

- Madsen, J., Sutherland, J.W., Bloomfield, J.A., Eichler, L.W. and Boylen, C.W. (1991). The decline of native vegetation under dense eurasian watermilfoil canopies. *Journal of Aquatic Plant Manage*, 29:94–99.
- Murphy, E. (2006). *Longitudinal dispersion in vegetated flow*. Master's thesis, MIT.
- Nepf, H. and Ghisalberti, M. (2008). Flow and transport in channels with submerged vegetation. *Acta Geophysica*, 56(3):753–777.
- Nepf, H.M. (1999). Drag, turbulence and diffusion in flow through emergent vegetation. *Water Resources Research*, 35(2):479–489.
- Nepf, H.M., Mugnier, C.G. and Zavistoski, R.A. (1997a). The effects of vegetation on longitudinal dispersion. *Estuarine, Coastal and Shelf Science*, 44:675–684.
- Nepf, H.M., Sullivan, J.A. and Zavistoski, R.A. (1997b). A model for diffusion within emergent vegetation. *Limnology and Oceanography*, 42(8):1735–1745.
- Nepf, H.M. and Vivoni, E.R. (2000). Flow structure in depth-limited, vegetated flow. *Journal of Geophysical Research*, 105:28547–28557.
- Nepf, H. and Koch, E. (1999). Vertical secondary flows in submersed plant-like arrays. *Limnol. Oceanogr.*, 44(4):1072–1080.
- Nikora, V. (2009). Hydrodynamics of aquatic ecosystems: An interface between ecology, biomechanics and environmental fluid mechanics. *River Research and Applications*, In press.
- Poggi, D., Katul, G. and Albertson, J. (2004a). A note on the contribution of dispersive fluxes to momentum transfer within canopies. *Boundary Layer Meteorology*, 111:615–621.

- Poggi, D., Porporato, A., Ridolfi, L., Albertson, J. and Katul, G. (2004c). The effect of vegetation density on canopy sub-layer turbulence. *Boundary Layer Meteorol*, 111:565–587.
- Pope, S. (2000). *Turbulent Flows*. Cambridge University Press.
- Raupach, M.R. and Thom, A.S. (1981). Turbulence in and above plant canopies. *Ann. Rev. Fluid Mech.*, 13:97–129.
- Rosman, J., Monismith, S., Denny, M. and Koseff, J. (2010). Currents and turbulence within a kelp forest (*macrocystis pyrifera*): Insights from a dynamically scaled laboratory model. *Limnol. Oceanogr.*, 55(3):1145–1158.
- Rueda, F. and Cowen, E. (2005). Residence time of a freshwater embayment connected to a large lake. *Limnology and Oceanography*, 50(5):1638–1653.
- Sand-Jensen, K. (2003). Drag and reconfiguration of freshwater macrophytes. *Freshwater Biology*, 48:271–283.
- Sand-Jensen, K. (2005). Aquatic plants are open flexible structures -a reply to sukhodolov. *Freshwater Biology*, 50:196–198.
- Schlichting, H. (1979). *Boundary layer theory*. McGraw-Hill.
- Schlichting, H. and Gersten, K. (2000). *Boundary Layer Theory*. Springer, 8th edition.
- Spalart, P. (1986). Direct simulation of a turbulent boundary layer up to $re=1410$. *NASA Technical memorandum 89407*.
- Statzner, B., Lamouroux, N., Nikora, V. and Sagnes, P. (2006). The debate about drag and reconfiguration of freshwater macrophytes: comparing results obtained by three recently discussed approaches. *Freshwater Biology*, 51:2173–2183.

- Stone, B. and Shen, H. (2002). Hydraulic resistance of flow in channels with cylindrical roughness. *J. Hydraul. Eng.*, 128(5):500–506.
- Su, H., Paw, K. and Shaw, R. (1996). Development of a coupled leaf and canopy model for the simulation of plant-atmosphere interaction. *Journal of Applied Meteorology*, 35:733–748.
- Sucker, D. and Brauer, H. (1975). Investigation of the flow around transverse cylinders. *Heat and Mass Transfer*, 8:149–158.
- Sukhodolov, A. (2005). Comment on drag and reconfiguration of macrophytes. *Freshwater Biology*, 50:194–195.
- Sumner, D., Wong, S., Price, S. and Paidoussis, M. (1999). Fluid behaviour of side-by-side circular cylinders in steady cross-flow. *J. Fluid Struct.*, 13:309–338.
- Tanino, Y. and Nepf, H. (2008a). Laboratory investigation of mean drag in a random array of rigid, emergent cylinders. *Journal of Hydraulic Engineering*, 134:34–41.
- Tanino, Y. and Nepf, H. (2008b). Lateral dispersion in random cylinder arrays at high Reynolds number. *J. Fluid Mech.*, 600:339–371.
- Tennekes, H. and Lumley, J.L. (1972). *A first course in Turbulence*. MIT Press.
- Tinoco, R. (2008). *An experimental investigation of the turbulent flow structure in one-dimensional emergent macrophyte patches*. Master’s thesis, Cornell University.
- Variano, E. and Cowen, E. (2008). A random-jet-stirred turbulence tank. *J. Fluid Mech.*, 604:1–32.

- Vermaat, J. and Thampanya, U. (2006). Mangroves mitigate tsunami damage: A further response. *Estuar. Coast. Shelf. Sci.*, 69:1–3.
- Wereley, S. and Meinhart, C. (2001). Second-order accurate particle image velocimetry. *Exp. Fluids*, 31:258–268.
- Wienke, J. and Oumeraci, H. (2005). Breaking wave impact force on a vertical and inclined slender pile: theoretical and large-scale model investigations. *Coastal Engineering*, 52:435–462.
- Wieselsberger, C. (1922a). New data on the laws of fluid resistance. Technical report, National Advisory Committee for Aeronautics.
- Williamson, C. (1985). Evolution of a single wake behind a pair of bluff bodies. *J. Fluid Mech*, 159:1–18.
- Williamson, C. (1996). Vortex dynamics in the cylinder wake. *Annu. Rev. Fluid Mech.*, 28:477–539.
- Zima, L. and Ackerman, N. (2002). Wave generation in open channels by vortex shedding from channel obstructions. *J. of Hydraulic Eng.*, 128(6):596–603.